Advanced Moderator Material Handbook

FY25 Version

C.A. Kohnert (LANL), W.D. Neilson (LANL), M. Nedim Cinbiz (ORNL), A.P. Shivprasad (LANL), J.R. Torres (LANL), T.E. Cutler (LANL), D.W. Wootan (PNNL), J.K. Jewel (INL), V.K. Mehta (LANL), S. Widgeon Paisner (LANL), C.N. Taylor (INL), E.P. Luther (LANL), H.R. Trellue (LANL)

LA-UR-25-30471
September 30, 2025

Los Alamos
NATIONAL LABORATORY

Prepared for: U.S. Department of Energy
Office of Nuclear Energy
John H. Jackson| National Technical Director
DOE Microreactor Program

Prepared by: Caitlin Kohnert| Scientist
Los Alamos National Laboratory

Foreword to FY25 Revision

The first version of the Advanced Moderator Material Handbook was published in United States Fiscal Year 2020 to consolidate knowledge on yttrium dihydride for nuclear reactor moderator applications [1]. The purpose of the handbook was to exist a living document to reflect updates to new findings, results, and publications of experimental data related to nuclear applications of yttrium dihydride as they become available.

The FY22 revision [2] included data from the Transformational Challenge Reactor program originally conducted at Oak Ridge National Laboratory. These results were primarily in the form of material properties. Additionally, Handbook sections were split and reorganized to improve clarity and overall readability.

The FY23 revision [3] added pre- and post-irradiation examination of neutron-irradiated yttrium dihydride through the U.S. Department of Energy Office of Nuclear Energy (DOE NE) Microreactor Program and the inclusion of the results from the Hypatia experiment, also performed through the DOE NE Microreactor Program.

The principal addition to the FY25 revision is a summary of literature data on thermophysical and mechanical properties of zirconium hydride.

Acknowledgements

This document was developed collaboratively with a team of subject matter experts who contributed content and recommendations.

How to cite this document: C.A. Kohnert et al. “Advanced Moderator Material Handbook: FY25 Version,” Los Alamos National Laboratory, Los Alamos, NM, LA-UR-xx-xxxx, 2025.

Summary

High hydrogen density moderators such as metal hydrides are an important research topic within the DOE NE Microreactor Program due to their ability to retain hydrogen to much higher temperatures than other hydrogenous media. This class of moderators, which includes yttrium dihydride (δ-YH_2) and zirconium hydride (δ-$ZrH_{1.6}$ or ϵ-$ZrH_{1.8}$), thermalizes neutrons in the system such that the overall fuel mass or the required uranium enrichment in the system can be significantly reduced. Knowledge of material properties, both in the as-fabricated and irradiated state, are important to understanding moderator performance during steady-state and transient reactor operation.

Provided in this document is the Advanced Moderator Material Handbook, which gives a detailed summary of the YH and ZrH thermomechanical and other property data available in the literature. This handbook also provides microstructural and thermophysical property data for YH that has been irradiated in the Advanced Test Reactor at Idaho National Laboratory, as well as nuclear data from an integral critical experiment at the National Criticality Experiments Research Center at Los Alamos National Laboratory. This report focuses on measured quantities but also includes some modeling results for comparison where applicable.

From the evaluation of the available literature data, further work is necessary for thoughtful deployment of YH and ZrH moderators in microreactors. Although property data is relatively extensive, details on material degradation are lacking. In particular, the knowledge base for hydrogen redistribution under temperature gradients, as well as moderator reactivity during accident scenarios such as a reactor breach, warrant further study. In addition, literature information on hydrogen concentrations at given pressures and temperatures exhibits significant variation. A better understanding of the effect of radiation damage on hydrogen release and degradation is needed. Development of cladding capable of retaining hydrogen at elevated temperatures, under irradiation, for many years is needed for the deployment of high temperature microreactors and is a current area of R&D focus for many programs. In this edition of the Handbook we primarily added literature on zirconium hydride. In the next Handbook edition, we plan to compile data from in-progress irradiation and cladding development campaigns.

Contents

Contents

Figures

Contents

Contents

Tables

1 Introduction

1.1 Moderators for microreactor applications

Advanced nuclear reactors such as small modular (SMR) and microreactors are emerging as a viable power generation technology around the world. With their small size, high power output, and relatively low cost, microreactors are envisioned to meet localized power generation needs; these needs may include integration into microgrids to provide power to remote locations and disaster-prone regions, space applications such as nuclear propulsion or fission surface power, and military forward bases. The United States government as well as several private companies have expressed commitment to developing novel, compact nuclear power generation. The Kilopower Reactor Using Stirling TechnologY (KRUSTY) was a recent demonstration performed at the National Criticality Experiments Research Center (NCERC) in March 2018 [4]. Its ambitious, self-regulating features made it highly attractive for terrestrial and space power and propulsion applications. However, the KRUSTY design required highly enriched or weapons-grade uranium to achieve criticality, much like many existing compact designs from the past [Systems Nuclear Auxiliary POWER (SNAP), Aircraft Nuclear Propulsion program (ANP)]. Reduction of the enrichment level from weapons-grade to civilian-grade fuel is highly sought after, but results in higher core masses; this can be ameliorated by using a moderator to slow down neutrons. Moderator materials selected for these concepts must be usable at high temperatures to improve power conversion efficiencies, which makes metal hydrides, graphite, and beryllium-containing compounds attractive candidate materials.

Nuclear moderators are used to thermalize, or slow down, high-energy neutrons so that they may more efficiently participate in fission reactions in isotopes such as uranium-235, which has a high capture cross section in the thermal-neutron energy range [5]. The nearly equal mass of hydrogen to that of a neutron enables significant energy transfer through inelastic collisions. Water is therefore a commonly used moderator due to its high hydrogen density, wide availability, and low cost. However, high-temperature water and steam pose significant risk of corrosion, and the total hydrogen density in steam and supercritical water is much lower than in liquid water. Among the promising alternatives are metal hydrides, owing to their greater thermal stability and hydrogen mass density at high temperatures. The SMR and microreactor concepts are designed around compact nuclear cores that operate at temperatures above what is practical with water moderators. In this respect, metal hydrides are a leading candidate class of materials for a moderator.

Metal hydrides exhibit greater moderating efficiencies due to their high hydrogen densities. Moreover, zirconium, cerium, and yttrium hydrides retain their high hydrogen densities at temperatures in excess of 773 K, the most stable of which is yttrium dihydride (YH_2), up to 1623 K [6]. Due to the historical use of graphite, beryllium, and zirconium hydride as nuclear reactor moderators, there exists a wealth of property and neutronic data for these materials. Zirconium hydrides ($ZrH_{1.6}$ or $ZrH_{1.8}$) have been used for decades in reactor systems as either a separate moderator or as part of the fuel system. Examples include the Russian Topaz-II reactor [7], the SNAP-8 and -10 series reactors [8, 9], and the TRIGA reactor series [10]. However, at temperatures above 923 K, hydrogen will eventually desorb from zirconium hydrides with a corresponding decrease in moderating power. Figure 1-1 plots the equilibrium hydrogen atom density of water compared to various metal hydrides that are in equilibrium with 101.325 kPa (1 atm) of hydrogen gas as a function of temperature. Here, zirconium hydride shows a quadratic decrease in H density between 923 and 1123 K followed by a steep drop around 1123 K. Moreover, we note that the 101.325 kPa of hydrogen cover gas is an optimistic scenario; therefore, it is more realistic that hydrogen dissociation will

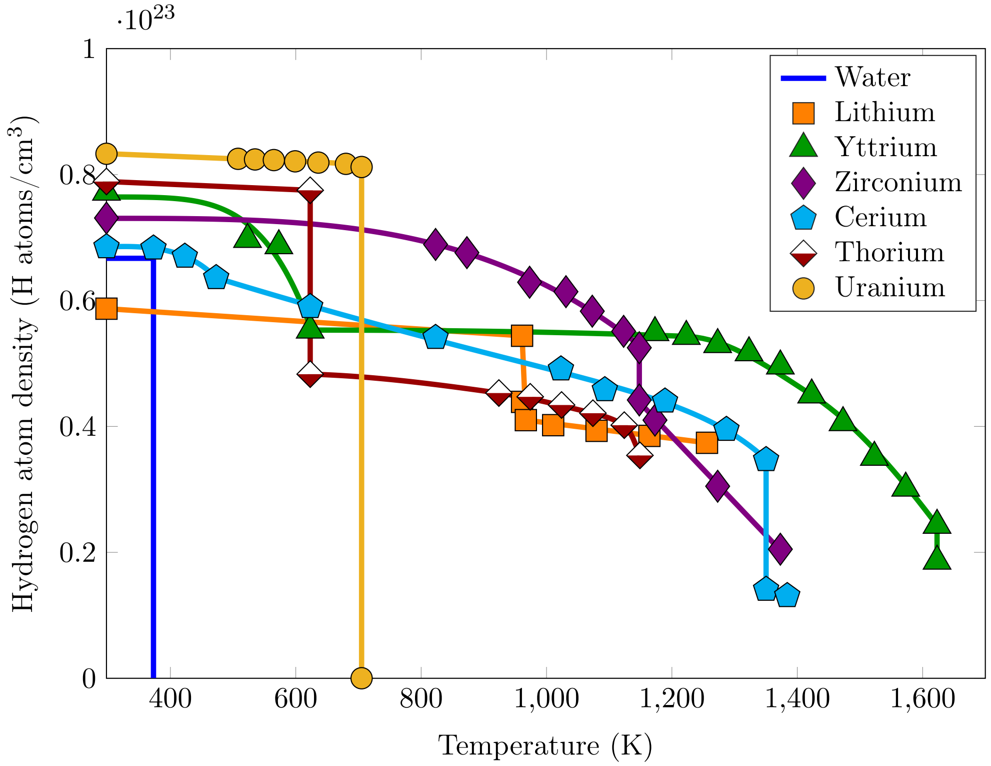

Figure 1-1: Hydrogen atom density as a function of temperature for water and various metal hydrides in equilibrium with $101.325\,\mathrm{kPa}$ of hydrogen gas for temperatures between 25 and $1600\,\mathrm{K}$. Decreases in hydrogen density are associated with hydrogen content changes with temperature and with thermal expansion. Figure and caption modified from [6].

occur at lower temperatures.

In Figure 1-1, YH_2 displays superior hydrogen retention at the highest temperatures compared to zirconium hydrides. Between 673 and 1273 K, the hydrogen density of YH_2 is roughly constant with significant hydrogen desorption occurring around 1623 K, and historical data notes that YH_2 has shown the ability to melt without significant decomposition [11]. Hydrides welded inside a hydrogen-impermeable cladding can operate at elevated temperature without hydrogen loss. In this scenerio, the hydrides will lose hydrogen until the pressure inside the can reaches equilibrium with the metal hydride. The back pressure at which hydrogen gas stops desorbing and equilibrates with the metal hydride is dictated by the pressure-composition-temperature curves. Equilibrium back pressures are significantly higher for zirconium hydride than yttrium hydride, making cladding fabrication generally easier for the latter.

This Handbook serves as a culmination of the phase stability, thermodynamic, thermophysical, mechanical, hydrogen-diffusion, and post-irradiation performance properties of YH and ZrH from across published literature in the context of microreactor technology development. We note that a significant portion of these collected works originate from the U.S. Department of Energy Office of Nuclear Energy's Micro Reactor Program and Transformational Challenge Reactor (TCR) program [12, 13].

This Handbook is organized as follows. Section 2 covers manufacturing and research needs for metal hydrides. Sections 3-5 cover literature data on yttrium hydride thermodynamics, fabrication and properties. Section 6 covers new additions on the properties of unirradiated zirconium hydride.

Section 7 contains neutronic considerations to metal hydride moderators. Finally, Sections 8-10 present the results of various nuclear tests of YH_2, including in-reactor irradiations at various test reactors including the Advanced Test Reactor (ATR), as well as an integral critical experiment at the NCERC.

1.2 Summary of techniques

This section details the various techniques used to measure the experimental data presented in the rest of this document.

Bulk yttrium dihydride production An overview of fabrication of metal hydrides for historic nuclear applications is given by Van Houten and is briefly summarized here [11]. Historically, the fabrication of large metal hydride components for nuclear reactors was achieved using systems that were designed to hydride components to a specific hydrogen content by hydrogen aliquoting or matching hydrogen pressures and reaction vessel temperatures, as per the pressure-composition-temperature (PCT) diagrams of the metal-hydrogen system of interest. Hydriding furnaces on the order of meters in diameter and up to tens of meters in height were used during the Aircraft Nuclear Propulsion Program to produce large components of titanium, zirconium, and yttrium hydrides.

In more recent efforts, metal hydrides have been produced using a Sieverts-type apparatus, which is a gas manifold attached to a calibrated-volume reaction vessel maintained at a temperature of interest. A metal sample is placed in the reaction vessel and hydrogen is titrated into the vessel in well-defined aliquots. The analysis of the subsequent gas-solid reaction is termed "Sievert's gas absorption" from which one can determine the hydrogen content of the resultant metal hydride, the PCT relationships, and, thus, the thermodynamics of the gas-solid reaction. One alternative to the hydride retort and Sieverts gas absorption methods is to expose high-purity metal to hydrogen pressure defined by an isochore for the particular metal-hydrogen system and a defined hydrogen content; this method was first described by Van Houten [14] and was later used by Hu, et al. to produce yttrium dihydride [13]. Another alternative fabrication method is the powder metallurgy process invented by Shivprasad et al. [6].

Measurement of hydrogen concentration There are several methods used to measure hydrogen concentration with varying levels of accessibility, applicability, and accuracy. Sieverts gas absorption, as discussed above, allows for the measurement of the number of moles of hydrogen absorbed in a sample as determined by the corresponding pressure drop in the reaction vessel. Note that this assumes a correct hydrogen gas equation of state is used; systematic errors in the pressure, reaction gas manifold volume, and temperature can lead to significant uncertainty. More commonly used is the gravimetric method in which the difference between the mass before and after the absorption reaction is assumed equivalent to the mass of absorbed hydrogen; here accuracy depends on that of the balance and requires high gas purities such that that all mass change is due to hydrogen absorption. There are also destructive methods such as inert gas fusion and vacuum hot extraction where a sample is heated to release the absorbed hydrogen, which is then quantified using various analytical techniques [15]. Among the more advanced nondestructive methods, there is neutron radiography, which measures the attenuation of a neutron beam by the hydrogenated sample and has been shown to be quantitative provided that appropriate calibrations/standards are used [16, 17]. Similarly, cold-neutron prompt gamma activation provides a unique prompt-gamma decay signature upon absorption of a neutron; the intensity of this prompt gamma line is correlated to the overall hydrogen content of the material [18, 19]. These neutron techniques, however, are inherently expensive and can be difficult to access.

Phase formation Yttrium and zirconium form various hydride phases with hydrogen solubility limits that depend on temperature and pressure. Measurements of the phase-formation thermodynamics include calorimetry where heat evolution/absorption is measured as a function of temperature relative to a reference temperature. The phase formation thermodynamics, determined using Sievert's gas absorption or calorimetric methods, are used to calculate phase diagrams. One well-established technique to do this is the Calculation of Phase Diagrams (CALPHAD) method, where thermodynamic parameters for the relevant phases are summarized in a database and a computer program is used to calculate the respective Gibb's Free Energies [20]. The computer programs perform Gibb's energy minimization calculations to determine the equilibrium phase diagrams given the input thermodynamic parameters. Thus, the resultant phase diagrams depend heavily on the reliability of the input thermodynamic data.

Material structure provides supplementary information for phase diagram evaluation. Structural parameters are typically determined using X-ray diffraction (XRD) or neutron diffraction (ND) [21, 22]. In these techniques, the incident particles (X-rays or neutrons) scatter off the probed material, following Bragg's Law, which then allows the crystal unit cell parameters to be determined through structure refinement. Moreover, neutrons are highly penetrating and hydrogen nuclei in metal hydrides exhibit very high neutron-scattering cross sections compared to X-rays, thus enabling bulk phase fraction measurements and occupancy factor determination.

Thermophysical properties Thermal expansion properties, including the coefficient of thermal expansion (CTE), have been measured using dilatometric methods as well as XRD and ND [23–27]. In our opinion, ND data are preferred due to the ability to probe bulk properties as well as gather simultaneous structural and thermal expansion information. Like phase formation thermodynamics, heat capacity is also measured using calorimetric methods [23, 25, 26, 28]. Thermal diffusivity may be measured using laser flash analysis, where the sample is exposed to a laser and the measured heat rise across the sample is an indication of the material thermal diffusivity [25, 26, 28]. Finally, thermal conductivity may be measured either using a thermal conductivity probe [23] or from the product of the density calculated from the CTE, the heat capacity, and the thermal diffusivity, all as a function of temperature.

Hydrogen diffusion The magnetic properties and hydrogen self-diffusion properties of metal hydrides have been measured using nuclear magnetic resonance (NMR) [29–32]. NMR involves application of a magnetic field to a sample to probe the local magnetic fields about the nucleus of interest. Radio-frequency pulses are used to excite the nuclei, which relax from the excited state. Relaxation times are dependent on experimental parameters and material properties. Thus, if the experimental parameters are kept constant, the material properties, such as mobility and structure, may be determined. This technique can probe the electronic structure of various nuclei and is a bulk measurement technique because the signal is representative of the ensemble of nuclei in the system.

There are several neutron-scattering methods used to measure hydrogen diffusion rates. Quasi-elastic neutron scattering (QENS) and neutron spin-echo spectroscopy are inelastic scattering techniques that measure very small energy exchanges between incident neutrons and a sample's hydrogen nuclei on dynamic time scales that span hydrogen self-diffusion processes (on the order of picosecond to microsecond timescales). QENS studies have been performed for various metal hydrides to uncover ion diffusion rates and pathways [33–36]. Recently, in-situ and ex-situ neutron radiography has been used to quantify hydrogen concentrations and diffusion rates (using the Fick equation) in zirconium alloys [37–40], the principles of which could be extended to studies on yttrium hydrides [41].

Mechanical properties The mechanical properties of metal hydrides may be determined using traditional methods like uniaxial tensile testing and creep testing [23]. However, preparation of dogbone samples, for example, is very difficult due to cracking and anisotropic volume expansion of large test pieces. Acoustical measurements like resonant ultrasound spectroscopy (RUS) provide a measure of elastic properties of various metal hydrides [6, 27, 42]. In the RUS technique, the sample is subject to mechanical vibrations swept through ultrasound frequencies, which then generate a series of resonances that are solutions to the equation of motion. Elastic properties are then determined by modeling the experimental spectra through either finite-element analysis or energy minimization methods.

Radiation effects Post-irradiation examination of ATR-irradiated YH_2 samples is presented in this Handbook and highlights radiation-induced changes to microstructure and physical properties. Some ion irradiation studies on the fundamental radiation effects in YH and ZrH were recently published and will be included in the next Handbook iteration, along with more recent neutron irradiation data.

Nuclear properties In addition to characterization of material properties, nuclear cross section data to predict performance of a material is important to understand. Density functional theory (DFT) codes can be used to model fundamental, atomistic properties, such as interatomic forces and crystal lattice parameters [6, 25, 43–48]. Validation of results from DFT codes has occurred using neutron time-of-flight powder diffraction and elastic constant measurements [6, 46, 48]. Of particular interest for hydride material performance in a nuclear system is the generation of thermal scattering laws that contribute to inelastic scatter cross sections such as incoherent inelastic neutron scattering ($S(\alpha,\beta)$) in Monte Carlo transport codes such as the Monte Carlo N-Particle Transport Code (MCNP) [47]. Once the thermal scatter laws are generated, they can be processed by codes such as NJOY to generate data for MCNP [49]. The cross sections developed in this way can then be validated against nuclear reactivity data generated during a critical test, such as was done for YH_2 at NCERC [50].

2 Summary of manufacturing and research needs

Although the benefits of using a yttrium dihydride (YH) and zirconium hydride (ZrH) moderators are many, there are several gaps in knowledge and several logistical considerations for implementation of this material in nuclear reactors.

2.1 Manufacturing specifications

For the U.S. nuclear industry, one concern is that there is no domestic supply of yttrium, which has already been identified as a high supply chain risk to the U.S. economy [51]. As a result, *yttrium sourcing is a key need for research and end use in advanced nuclear reactors.*

A key drawback to the use of YH in nuclear reactors is the difficulty in producing the starting material at purity levels sufficient for nuclear applications. Currently, high-purity yttrium stock is only provided by a few commercial vendors and the material that is produced typically contains impurities that hinder the quantity of hydrogen absorbed, such as oxygen and fluorine [52], or impurities that are associated with neutronic penalties, such as tantalum [6]. The process by which high-purity yttrium metal is produced, which is described in greater detail in Section 3, requires high-purity yttrium oxide (Y_2O_3) as a starting material, with typical purities of 99.999% and less than 10 wt. ppm of lanthanides. *Innovative methods of purifying yttrium metal from high-purity starting materials are necessary to produce nuclear grades of YH.* Zirconium metal usually contains Hf, a neutron poison which must be removed before fabricating ZrH moderators. The most available nuclear grade (low Hf content) zirconium alloy is Zircaloy-4, an alloy developed for nuclear fuel cladding.

2.2 Research needs and considerations

Currently, the process to manufacture YH and ZrH across a variety of synthesis techniques is well established and is deemed to be mature [6, 13]. Although these methods are informed by pressure-composition-temperature (PCT) relations, the absolute values of the PCT curves are not well established at high hydrogen-to-metal (H/M) ratios for both YH and ZrH. These values are necessary for predicting hydride phase stability under reactor conditions. As will be described in section 3, the equilibrium hydrogen pressures to achieve hydrogen contents within the two-phase Y-YH_2 phase regime are consistent across much of the literature. However, the equilibrium hydrogen pressures in the single-phase regimes are not consistent in the yttrium-hydrogen system. PCT curves are difficult to measure at high H/M in the zirconium-hydrogen system due to exponential pressure increase above 1 atm [53]. *Well-characterized PCT curves are needed to accurately predict performance of these materials in nuclear reactor systems.*

Similarly, most studies of the formation of the hydride have focused on equilibrium measurements. However, dynamic properties of the hydride are also necessary to predict material performance during reactor startup, normal operation, transients, reactor accidents, reactor shutdown, and under irradiation. *Of particular importance are phase formation kinetics, hydrogen absorption/desorption kinetics, hydrogen surface reaction rates, yttrium trihydride phase formation kinetics, and hydrogen diffusion kinetics.* All of these must be characterized as a function of hydrogen content (H/Y), hydrogen partial pressure, and temperature; in the case of diffusion kinetics, this must be determined additionally as a function of thermal gradients to determine their effect on diffusion above pure concentration-driven, Fick diffusion of hydrogen. Much of the dynamic hydrogen behavior in YH_2 can be predicted using modeling tools [54]. However, the lack of a consensus for much of the equilibrium and dynamic hydrogen data make modeling efforts challenging.

Hydrogen-impermeable cladding development is the **most significant remaining challenge** for implementing metal hydride moderators into microreactors. Metal hydrides must be contained in cladding to operate for long periods at elevated temperatures. As the temperature increases, the hydrides will off-gas hydrogen into the plenum, which stabilizes the majority of hydrogen inside the metal hydrides at elevated temperature. If hydrogen can readily diffuse through the cladding, this stabilization process will never occur because the moderator element will experience continuous pressure loss. If the cladding is made from a material impermeable to hydrogen, the hydrogen won't diffuse through the cladding, and the moderator element will stabilize at elevated temperature. Hydrogen impermeable materials are typically refractory metals and ceramics, which are more difficult to machine and hermetically seal. As a bonus, cladding offers containment for the brittle metal hydride pieces which might crack due to thermal cycling during operation. There are some ongoing cladding campaigns through various programs. This work will be added to the next edition of the Handbook.

3 Yttrium dihydride phases and thermodynamics

The yttrium-hydrogen (Y-H) system is, like many rare earth-hydrogen systems, relatively complex. The cubic dihydride phase forms from the hexagonal metal phase, which exhibits a significant amount of hydrogen solubility. The dihydride phase has been reported to have extreme thermal stability, even retaining its hydrogen to melting temperatures [11]. The presence of the trihydride phase, YH_3, complicates many fabrication efforts due to the large volume expansion upon formation, which often results in material pulverization. This section describes current knowledge of the Y-H phase system and the recorded fabrication methods to produce yttrium dihydride(YH_2).

3.1 Stable phases and phase transitions

Reviews of the Y-H system have been performed in the past, such as by Blackledge and Khatamian et al. [55, 56]. In this section, we combine the data given in these reviews with other recently reported results to provide a complete picture of the current understanding of the Y-H system.

For nuclear reactor moderator applications, the relevant phases within the Y-H system can be down-selected to those stable at ambient pressure and temperatures between 298 and 1273 K. There are three principal phases of interest: hcp yttrium metal (α-Y), fcc YH_2 (δ-YH_2), and trigonal/hexagonal YH_3 (ε-YH_3) [55–57]. There also exists a high-pressure, fcc yttrium trihydride, which maintains the same crystal structure as the ambient pressure dihydride [58].

Yttrium metal in the α-phase is stable at ambient pressure up to approximately 1753 K, at which point it transforms to the bcc β-yttrium. The melting point of yttrium metal is approximately 1803 K. The hydrides of yttrium are formed upon exposure of α-yttrium to hydrogen gas at pressures up to 101.325 kPa and temperatures up to approximately 1623 K [21, 59, 60]. Hydride formation may be possible at higher temperatures. However, investigations of hydriding have not been reported to temperatures above 1623 K.

The formation of the di- and trihydride phases is governed by pressure-composition-temperature (PCT) relations. Under sub-ambient pressures of hydrogen, both phases are possible to form. The dihydride phase is stable up to approximately 1623 K, while the trihydride phase is stable below approximately 623 and 673 K based on extrapolation of the PCT data [60, 61]. At temperatures above approximately 623 K, the trihydride phase decomposes to form the dihydride phase and hydrogen gas, and at temperatures above approximately 1623 K, YH_2 decomposes to form α-yttrium metal and hydrogen gas for hydrogen pressures below 101.325 kPa.

Other phases High-pressure compression (≥ 17 GPa) of YH_3 or Y-metal exposed to H_2 at low temperature yields hydrides with much higher hydrogen content, e.g., bct-YH_4, bcc-YH_6, and hcp-YH_9 [62, 63]. However, these "super-hydride" phases have not been shown to be stable at ambient pressures or temperatures and, thus, are not considered relevant for nuclear reactor use.

3.1.1 Reporting hydrogen composition

The hydrogen content of metal hydrides for moderator applications has been denoted by four principal units: (1) the hydrogen-to-metal atom ratio, or H/M; (2) the hydrogen atom fraction or percent; (3) the hydrogen weight fraction or percent; and (4) the hydrogen atom density in atom/cm^3. For neutronics calculations, the hydrogen atom density is the preferred unit, as it can readily be used to calculate macroscopic cross sections.

Yttrium dihydride phases and thermodynamics

The hydrogen-to-metal atom ratio is calculated as the moles of hydrogen absorbed by the hydride to the moles of yttrium metal (H/Y) in the original specimen. This is typically calculated through mass-balance measurements, but the moles of hydrogen absorbed can also be measured by hydrogen pressure drops during Sieverts gas absorption. The focus of this Handbook is YH_2, so H/M and H/Y are used interchangeably.

The hydrogen atom fraction or percent is calculated quite simply from the H/M ratio, X. In one molecule of YH_X, the hydrogen atom fraction, c_H, is given as:

$$c_H = \frac{\mathrm{X}}{1+\mathrm{X}} \tag{1}$$

Hydrogen weight fraction, or percent, is similarly determined. The hydrogen weight fraction, w_H, is related to X as follows:

$$w_H = \frac{M_H\,\mathrm{X}}{M_Y + M_H\,\mathrm{X}} \tag{2}$$

where M_H is the molar mass of monatomic hydrogen (approximately 1.01 g/mol) and M_Y is the molar mass of yttrium (approximately 88.91 g/mol).

The hydrogen atom density, N_H, is calculated from the mass density of the material (either the metal with hydrogen in solid-solution or the metal hydride), ρ, and X, as follows:

$$N_H\left(\frac{\text{atoms H}}{\text{cm}^3}\right) = \frac{\rho\left(\frac{\text{g}}{\text{cm}^3}\right)\ N_A\,\mathrm{X}}{M_Y + M_H\,\mathrm{X}} \tag{3}$$

where N_A is Avogadro's number $\left(6.022\times10^{23}\,\frac{\text{atoms}}{\text{mol}}\right)$. Table 3-1 shows a comparison between several different values for these parameters for yttrium, YH_2, and YH_3 at room temperature.

Table 3-1: Summary of hydrogen contents for yttrium and its hydrides that are relevant to nuclear reactor moderator applications at room temperature and ambient pressure.

X (H/M)	c_H (atom %)	w_H (weight %)	N_H (10^{22} atoms H/cm^3)	Phase(s) (-)
0.00	0.00	0.00	0.00	α-Y
0.10	9.09	0.11	0.30	α-Y
0.20	16.67	0.23	0.61	α-Y
0.30	23.08	0.34	0.91	α-Y + δ-YH_2
0.50	33.33	0.56	1.51	α-Y + δ-YH_2
1.00	50.00	1.12	3.00	α-Y + δ-YH_2
1.50	60.00	1.68	4.48	α-Y + δ-YH_2
1.70	62.96	1.89	5.06	α-Y + δ-YH_2
1.80	64.29	2.00	5.35	α-Y + δ-YH_2
1.90	65.52	2.11	5.64	α-Y + δ-YH_2
2.00	66.67	2.22	5.93	δ-YH_2
2.50	71.43	2.76	7.38	δ-YH_2 + ε-YH_3
3.00	75.00	3.30	8.80	ε-YH_3

3.1.2 Stable phase structural data

Key structural parameters for the relevant stable phases of yttrium hydrides are given in Table 3-2 along with the hydrogen-to-yttrium atom ratio, measured lattice parameters, and the techniques used to determine the lattice parameters. The data summarized in Table 3-2 show that the lattice parameters of each phase are very consistent across all studies, with discrepancies only principally arising on the order of approximately one-hundredth or one-thousandth of an angstrom. However, these differences could also mainly be due to differences in hydrogen content. While a more detailed study may be of interest, the data in the literature are thought to be sufficient due to the consistency across multiple studies and techniques.

Table 3-2: Lattice parameters for Y, YH_2, and YH_3 measured experimentally at ambient temperature and pressure using X-ray (XRD) and neutron diffraction (ND). *Setoyama et al. measured the lattice parameter (a) of δ-YH_2 as a function of hydrogen content that follows the empirical relation $\mathrm{a(nm)} = 0.5215 - 4.127 \times 10^{-4} c_H \mathrm{(H/Y)}$.

Phase (-)	Hydrogen content (H/Y)	a (Å)	c (Å)	Technique (-)	Ref. (-)
α-Y	0	3.6474 ± 0.0007	5.7306 ± 0.0008	XRD	[64]
	0	3.654	5.7501	XRD	[21]
	0.23	3.6636 ± 0.0009	5.7900 ± 0.0013	XRD	[65]
δ-YH_2	2.00	5.201	-	XRD	[21]
	1.96	5.205 ± 0.002	-	ND	[22]
	1.7 - 2.0	*	-	XRD	[24]
ε-YH_3	3.00	3.674	6.599	XRD	[21]
	2.90 - 3.00	3.672	6.659	XRD	[66]
	N/A	3.67 ± 0.02	6.62 ± 0.02	XRD	[67]

3.2 Thermodynamics and phase equilibrium

3.2.1 *Calculation of thermodynamic quantities*

An analysis of the PCT curves allows for calculation of the phase formation thermodynamics for yttrium or yttrium hydrides at a particular stoichiometry. The following is a summary of the analysis by Dantzer and extended to additional datasets that were not available at the time of that publication [68]. The PCT curves in Figure 3-1 can be broken down into three distinct regions that span H/M ratios of 0 to 2.0: hydrogen dissolved in yttrium metal, two-phase mixture of yttrium metal and YH_2 (α-Y + δ-YH_{2-x}), and single-phase δ-YH_{2-x}.

Hydrogen in yttrium metal For low values of H/Y, hydrogen absorbs into the yttrium metal by the process of adsorption, dissociation, and dissolution (solvation of hydrogen) [69]. The chemical equation for this reaction is given as:

$$\mathrm{H_2(g)} \rightleftharpoons 2\,\mathrm{H_M} \tag{4}$$

where $\mathrm{H_M}$ is hydrogen adsorbed onto the yttrium metal surface. At equilibrium, the chemical potential of the gas is equal to the chemical potential of the hydrogen in the metal. The equilibrium constant, called the Sieverts constant, is given as follows:

$$K_S = c_H \sqrt{p_{\mathrm{H_2}}} \tag{5}$$

where K_s is the Sievert's Law constant, c_H is the concentration of hydrogen in solution, and $p_{\mathrm{H_2}}$ is the equilibrium partial pressure of hydrogen. K_s is related to thermodynamic properties through

Yttrium dihydride phases and thermodynamics

Gibb's Free Energy as follows:

$$K_S = K_S^0 \exp\left(-\frac{\Delta H}{RT} + \frac{\Delta S}{R}\right) \tag{6}$$

where K_s^0 is the pre-exponential factor for the Sieverts constant and ΔH_s and ΔS_s are the enthalpy and non-configurational entropy of solution, respectively. Combining Equations (5) and (6) enables calculation of the standard enthalpy and entropy of formation for a given H/M value given knowledge of K_s^0 [70]. The result is that Gibb's Free Energy, and thus the enthalpy and non-configurational entropy of solution, is a linear function of the hydrogen concentration.

Two-phase yttrium/yttrium dihydride regime At intermediate values of H/Y, the hydrogen reacts with saturated yttrium metal to form the dihydride. This is represented in the PCT curves as the plateau region and consists of two-phase saturated α-yttrium and δ-YH_2 at the equilibrium stoichiometry given by the composition at the phase boundary. For example, at 873 K, at an overall stoichiometry of 1.0 H/Y units, the material will consist of α-yttrium with an approximate composition of 0.45 H/Y units and δ-YH_2 with a composition of 1.5 H/Y units. In this two-phase region, the hydrogen absorption reaction can be written as:

$$\frac{2}{2-y-z}\mathrm{YH}_y + \mathrm{H_2(g)} \rightleftharpoons \frac{2}{2-y-z}\mathrm{YH}_{2-z} \tag{7}$$

where y is the maximum solubility of hydrogen in yttrium metal and z is the sub-stoichiometry in hydrogen sublattice of YH_2 [68]. The enthalpy and entropy of the reaction do not vary with hydrogen concentration, as required by chemical equilibrium [71].

Single-phase yttrium dihydride The general reaction between yttrium metal and hydrogen gas to form the single-phase dihydride is given as follows:

$$\mathrm{Y\,(s)} + \frac{2-x}{2}\mathrm{H_2\,(g)} \rightleftharpoons \mathrm{YH}_{2-x} \tag{8}$$

where x is the degree of sub-stoichiometry in the hydrogen sublattice. For a reversible reaction, the equilibrium constant for this equation is given as follows:

$$K_{\mathrm{eq}} = \frac{a\,(\mathrm{YH}_{2-x})}{a(\mathrm{Y})\,a(\mathrm{H_2})^{\frac{2-x}{2}}} \tag{9}$$

where $a(i)$ is the activity of species i. Assuming that the activities of the solid, pure phases are unity, and that the concentrations of gases are equal to their equilibrium partial pressures ($p_g = p_{\mathrm{eq}}/p_0$), then

$$K_{\mathrm{eq}} = p_{\mathrm{H_2}}^{-\left(\frac{2-x}{2}\right)} \tag{10}$$

Combining the definitions of Gibb's Free Energy yields:

$$\ln\left(K_{\mathrm{eq}}\right) = -\frac{\Delta H^\circ}{RT} + \frac{\Delta S^\circ}{R} \tag{11}$$

$$\frac{2-x}{2}\ln\left(p_{\mathrm{H_2}}\right) = \frac{\Delta H^\circ}{RT} - \frac{\Delta S^\circ}{R} \tag{12}$$

where ΔH° is the standard reaction enthalpy and ΔS° is the standard reaction entropy.

From this analysis, the natural log of the equilibrium constant (K_{eq}) and the natural log of the hydrogen partial pressure are both linear functions of 1/T. The enthalpy of formation is obtained from the slope of the curve, while the entropy of formation is obtained from its intercept. For exothermic reactions, the enthalpy of formation is negative, which yields a negative slope for plots of $\ln(p_{\mathrm{H_2}})$ vs. 1/T and a positive slope for plots of $\ln(K_{\mathrm{eq}})$ vs. 1/T.

3.2.2 Pressure-composition-temperature curves

PCT curves plot equilibrium partial pressure as a function of composition/stoichiometry for gas-solid reactions and are used extensively for hydrogen-solid interactions. As described in section 3.2.1, the equilibrium partial pressure of hydrogen and hydrogen content of the hydride phase are directly related to the enthalpies and entropies of the hydriding reaction.

The PCT diagrams are typically developed using a Sieverts apparatus or a modification thereof. In a typical experiment, a sample is placed in a reaction vessel with a well-defined volume that is attached to a gas manifold also with a well-defined volume. The reaction vessel is evacuated to a suitable vacuum level and then heated to a desired temperature. Hydrogen is then aliquoted at precisely controlled pressures, followed by absorption of the hydrogen gas by the sample, and the corresponding pressure drop over time is measured. The moles of hydrogen absorbed by the sample are calculated from the measured pressure drop, the system volume, and the known temperature using an equation of state (such as the Ideal Gas Law) with assumptions therein. The moles of hydrogen absorbed are related to the initial moles of sample to produce a hydrogen composition. In this way, the equilibrium pressure of hydrogen is plotted as a function of hydrogen composition for each isothermal gas absorption experiment.

It is important to note that chemical compatibility between the sample and the reaction vessel must be considered, and potential hydrogen permeation through the reaction vessel must be addressed at high temperatures. Additionally, the condition of the sample surface, such as surface-adsorbed species, chemical treatment of the surface, ball-milling, and the presence of a surface oxide, have been shown to impact hydriding [72].

A compilation of the PCT curves in the literature for the Y-H system is plotted in Figure 3-1 as equilibrium pressure of hydrogen (on a logarithmic scale) as a function of hydrogen-to-yttrium atom ratio. Each curve represents data collected at a particular temperature. It is observed that, for low hydrogen contents, up to H/Y = 0.3 - 0.4, the PCT data follow an approximate Sieverts law dependence, which is characteristic of hydrogen solubility in the base yttrium metal, as will be discussed in section 5. For hydrogen contents between approximately 0.3 – 0.6 and 1.0 – 1.6 H/Y units, depending on the temperature, the hydrogen partial pressure remains constant as a function of hydrogen content, which is due to the formation of the dihydride from hydrogen-saturated yttrium metal and hydrogen gas. This regime is called the "plateau region" and represents two-phase equilibrium between the hydrogen-saturated metal and the dihydride, following the phase rule. Finally, at higher hydrogen contents, the hydrogen partial pressure rapidly increases as a function of hydrogen content. At this point, the system is single-phase dihydride that is nearly stoichiometric, and the accommodation of further hydrogen becomes increasingly difficult, i.e., more thermodynamically unfavorable.

Across the literature, it is observed that the plateau regions are very consistent and as such the reproducibility is high. However, the single-phase regions (hydrogen dissolved in yttrium metal or the single-phase dihydride) are quite inconsistent. For example, in the studies by Lundin et al. [21]

and Begun et al. [73], the terminal hydrogen content is H/Y = 2.0, while for Yannopoulos et al. [59] and Tanase et al. [74], their terminal values were closer to H/Y = 1.90 and 1.70, respectively. In the single-phase region with low hydrogen contents, the relationships between the hydrogen partial pressure and hydrogen-to-yttrium atom ratio are also not consistent across the various studies, though they are consistent within each single study. The origin of the inconsistencies is not currently known. We speculate that the starting metal's purity is a likely cause. Lundin et al. noted that the principal impurities in their yttrium metal were 0.57% zirconium and 0.32% oxygen. Yannopoulos et al., on the other hand, noted low-Z impurities of 0.179% oxygen and 0.0033% nitrogen, by mass. The yttrium metal used by Begun et al. showed approximately 0.1% dysprosium, cerium, and zirconium, as well as 0.45% oxygen and 0.05% nitrogen, hydrogen, and other rare earths, by mass, with impurities totaling approximately 0.85% by mass. Tanase et al. measured oxygen and nitrogen impurities to be 0.083% and 0.12%, by mass, respectively. Fu et al. [60] noted that the metal used in their work was vacuum distilled and provided a maximum purity (lowest impurity content of the group) of 0.0155% oxygen and 0.0030% nitrogen, by mass. The presence of alloying elements that do not form a hydride or hydride at higher partial pressures will likely skew the partial pressures to higher values. Substitutional impurity elements, such as oxygen, nitrogen, carbon, and fluorine, will bind with the yttrium atoms, resulting in a smaller population of yttrium atoms available for reaction with the hydrogen. Small differences in gas purities could also affect these impurity content values. Lundin et al. obtained hydrogen source gas by thermal decomposition of uranium hydride, whereas the studies by Yannopoulos et al. and Begun et al. used high-purity hydrogen gas cylinders with impurities of approximately 60 and 10 ppm, respectively. Yannopoulos et al. further purified their gas by using a liquid-nitrogen trap and by passing the gas over zirconium turnings. Tanase et al. used gas with a purity of 99.9999%, while Fu et al. did not mention the purity of the hydrogen gas used to develop the PCT curves. As with substitutional impurities, gas phase impurities can react with the yttrium, thus skewing the overall measured hydrogen content by gravimetric or Sieverts gas absorption methods.

Another possible source of the discrepancies could arise from the differences in the Sieverts apparatuses used in the various studies. Lundin et al., Yannopoulos et al., Begun et al., and Tanase et al. all used ceramic reaction vessels, such as mullite and quartz, due to the low permeability of hydrogen through these materials [75]. However, Fu et al. used a stainless steel reaction vessel, which is known to permeate hydrogen at elevated temperatures [76], raising the question as to how pressure equilibrium at high temperature was established in their study. As a result of the inconsistencies across datasets and the potential impact of gas and metal starting purities, it is believed that more work is necessary to further characterize the PCT relationships in the single-phase regions with careful consideration of sample preparation, vessel calibration, source-gas purity, and pressure/temperature control and sensitivity.

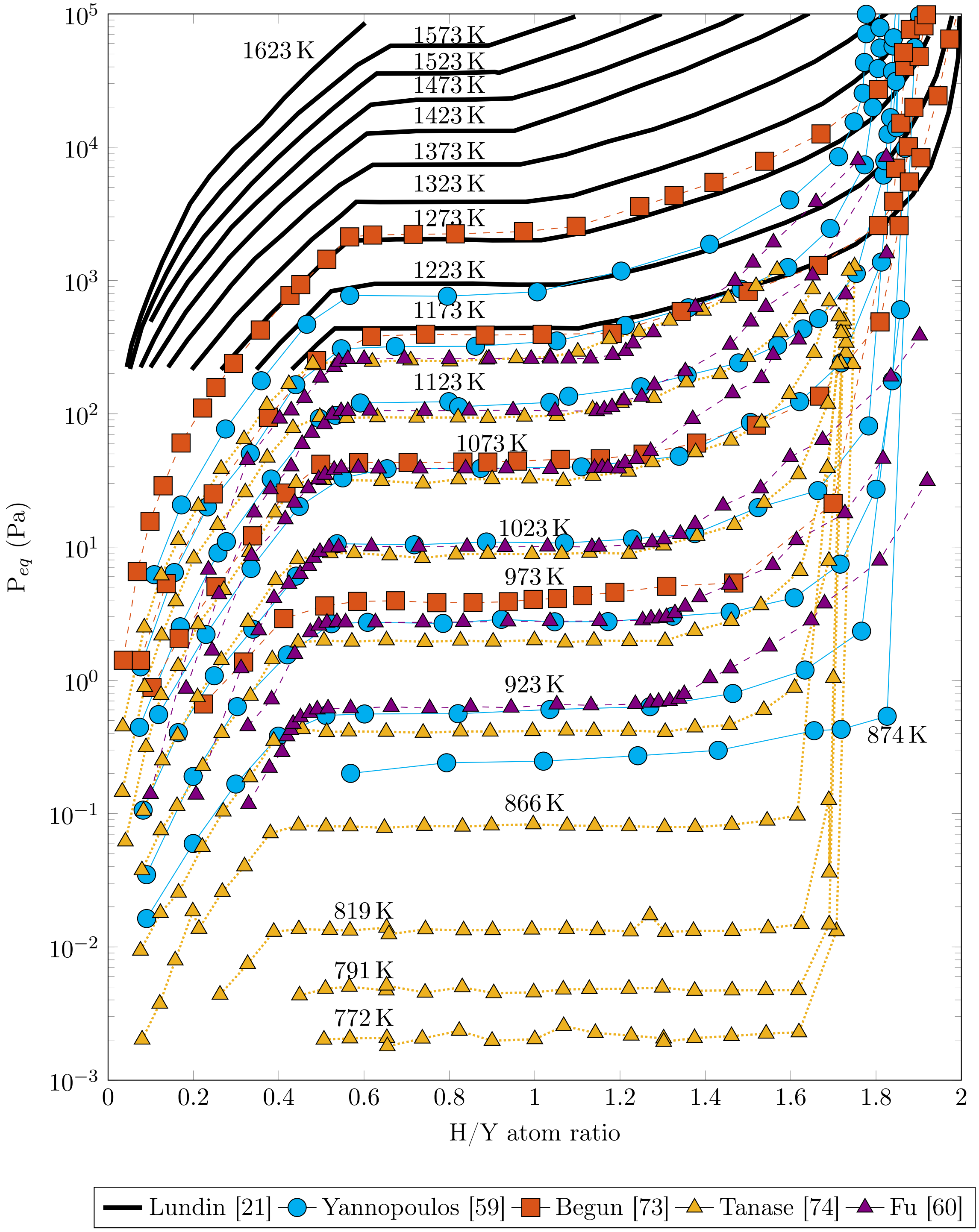

Figure 3-1: Compilation of PCT curves for the Y-H system up to a hydrogen-to-yttrium ratio of 2.0. Data replotted from [21, 59, 60, 73, 74].

3.2.3 Some hydrogen partial pressures of yttrium dihydride

As mentioned in section 3.2.2, the PCT data for the Y-H system exhibit consistency in the two-phase region (metal and dihydride in equilibrium) but show significant differences in the single-phase regions. A summary of the equilibrium partial pressures, along with the associated data spread from averaging over the various literature sources is shown in Table 3-3. Data are presented as equilibrium hydrogen pressure (in Pa) as a function of hydrogen-to-yttrium atom ratio and temperature (in K).

Table 3-3: Summary of equilibrium hydrogen pressures from literature PCT data [21, 59, 60, 73, 74]. Underlined values were extrapolated from low-temperature data. No data exists for H/Y = 2.0, exactly, due to the difficulty in achieving complete hydriding at these temperatures.

	P_{H_2} (Pa)			
X (H/Y)	T = 873 K	T = 1073 K	T = 1273 K	T = 1473 K
0.2	1.80×10^{-2}	2.43 ± 1.44	8.91×10^{1}	1.12×10^{3}
0.4	7.43×10^{-2}	$1.80 \times 10^{1} \pm 7.89$	$6.48 \times 10^{2} \pm 1.97 \times 10^{1}$	5.54×10^{3}
0.6	$1.43 \times 10^{-1} \pm 1.73 \times 10^{-1}$	$3.74 \times 10^{1} \pm 9.59$	$2.09 \times 10^{3} \pm 2.24 \times 10^{2}$	1.93×10^{4}
0.8	$1.61 \times 10^{-1} \pm 2.23 \times 10^{-1}$	$3.82 \times 10^{1} \pm 9.45$	$2.14 \times 10^{3} \pm 2.76 \times 10^{2}$	2.27×10^{4}
1.0	$1.65 \times 10^{-1} \pm 2.27 \times 10^{-1}$	$3.89 \times 10^{1} \pm 9.78$	$2.19 \times 10^{3} \pm 5.12 \times 10^{2}$	2.62×10^{4}
1.2	$1.74 \times 10^{-1} \pm 2.59 \times 10^{-1}$	$4.17 \times 10^{1} \pm 9.64$	$2.98 \times 10^{3} \pm 7.83 \times 10^{2}$	4.31×10^{4}
1.4	$1.87 \times 10^{-1} \pm 2.97 \times 10^{-1}$	$7.19 \times 10^{1} \pm 4.72 \times 10^{1}$	$4.73 \times 10^{3} \pm 1.37 \times 10^{3}$	7.61×10^{4}
1.6	$2.42 \times 10^{-1} \pm 4.08 \times 10^{-1}$	$1.78 \times 10^{2} \pm 2.07 \times 10^{2}$	$8.70 \times 10^{3} \pm 3.71 \times 10^{3}$	$\underline{1.40 \times 10^{5}}$
1.8	5.11×10^{-1}	$1.02 \times 10^{3} \pm 9.63 \times 10^{2}$	$2.23 \times 10^{4} \pm 1.18 \times 10^{4}$	$\underline{2.44 \times 10^{5}}$
2.0	N/A			

3.2.4 Enthalpies and entropies of formation

The enthalpies and entropies of formation for YH_2 are important to understand, as they provide information on how tightly bound the hydrogen is within the hydride moderator and, thus, help describe the propensity of the moderator to release hydrogen at a given set of conditions. The partial molar enthalpies of formation in the literature are plotted in Figure 3-2, while the partial molar entropies of formation are plotted in Figure 3-3. It should be noted that all results except those from Dantzer et al. were calculated using the above methods from the PCT curves, while Dantzer et al. measured the partial molar enthalpies of formation using calorimetric methods. Another available dataset by Fadeyev et al. was not included, due to a lack of access, as it is a foreign publication not available in English [77].

From Figure 3-2, it is observed that many of the data sets exhibit a significant degree of consistency. The only dataset that appears to disagree is the one by Lundin et al., for which the data appear to be consistently lower, as compared with the other literature. The temperature range examined in the study by Lundin et al. was higher than for all other studies, which could have impacted the analysis. In all studies, the enthalpies of formation are essentially constant in the two-phase equilibrium region of yttrium with YH_2 for hydrogen contents between approximately 0.5 and 1.0 H/Y units. In the dihydride single-phase region, the enthalpy of formation consistently increases with hydrogen content, though Dantzer et al. measured a significantly lower value at 2.0 H/Y units. However, in the metal single-phase region, the relationship between enthalpy of formation and hydrogen content is not as clear. The data by Dantzer et al. show a nearly constant enthalpy of formation in this region, while the values determined from other studies, calculated

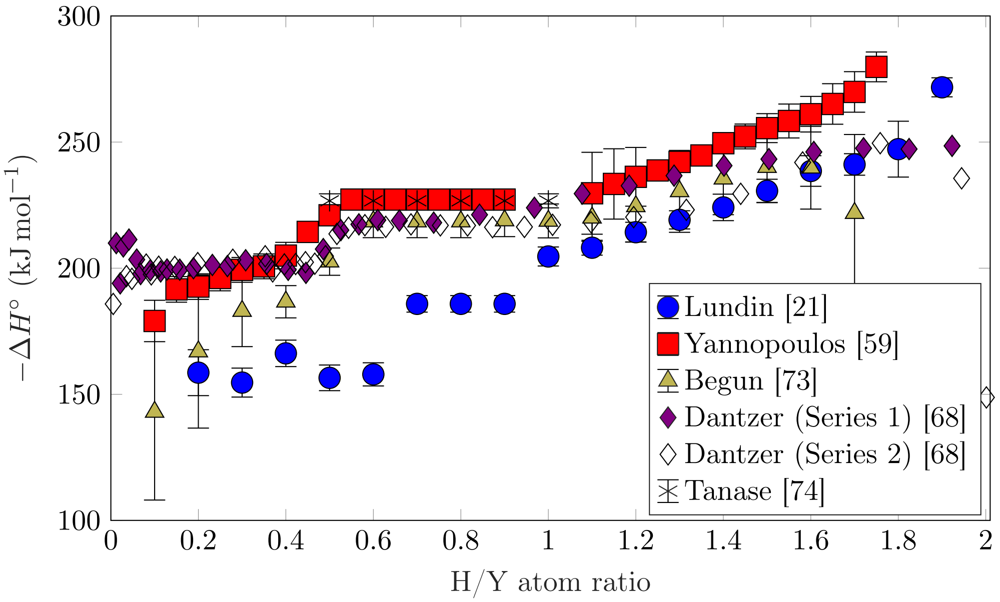

Figure 3-2: Partial molar enthalpy of formation for yttrium dihydride as a function of hydrogen content in H/Y units. Data taken from [21, 59, 68, 73, 74].

using the PCT curves, show increasing formation enthalpy with hydrogen content. It should be noted from Section 3.2.2 that there exists a significant degree of scatter in the PCT data for the pure metal and dihydride single-phase region across all datasets.

Similarly, in Figure 3-3, it is observed that the datasets exhibit a significant degree of overlap, with only the data from Lundin et al. deviating from the others. Again, this is believed to be due to the higher temperature at which hydrogen absorption experiments were performed. However, this is only the case for the yttrium metal single-phase and two-phase regions. In the dihydride single-phase region, all datasets exhibit consistency. The non-configurational entropy of formation is observed to increase with hydrogen content up to approximately 0.5 H/Y units, which demarcates the single-phase metal and two-phase metal and dihydride regions. In the two-phase region, the entropy of formation is constant. Finally, in the single-phase dihydride region, the non-configurational entropy increases with hydrogen content.

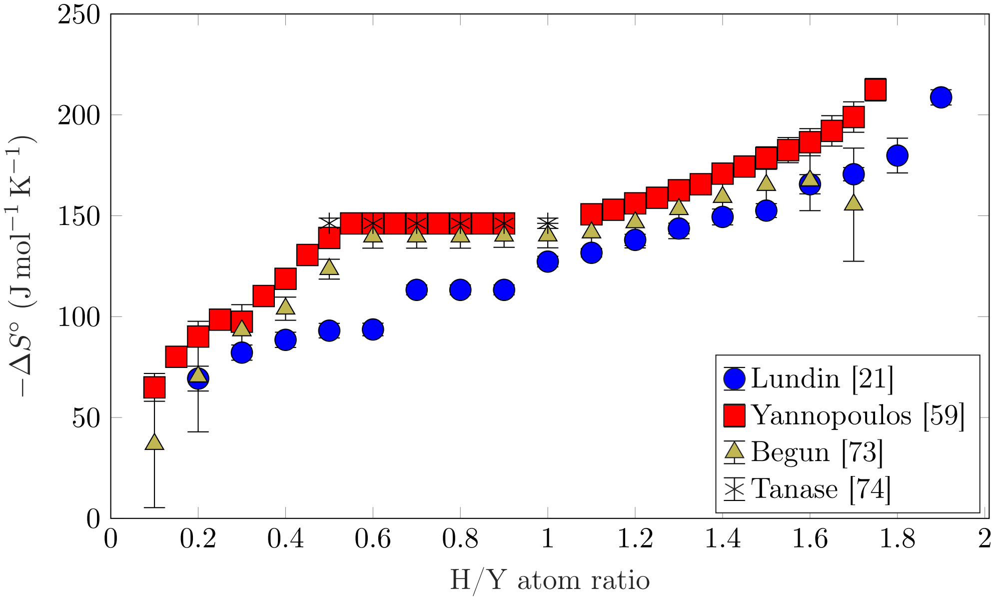

Figure 3-3: Partial molar non-configurational entropy of yttrium dihydride as a function of hydrogen content in H/Y units. Data taken from [21, 59, 73, 74].

3.2.5 Yttrium-hydrogen phase diagram

The phase diagrams for gas-solid systems are generated by projecting PCT curves onto the T-x axis and outlining phase-stability regions. As such, the phase diagrams omit the pressures required, but represent useful information. Phase diagram analysis of the Y-H system was first presented by Yannopoulos, et al. [59] and then summarized by Blackledge [55] by compiling data from Lundin, et al. and Yannopoulos, et al. More recently, CALPHAD analysis of the Y-H system thermodynamics was carried out by Fu, et al. and Peng, et al. [60, 61]. A redrawing of the Y-H phase diagram based on the analyses by Fu, et al. and Peng, et al. is presented in Figure 3-4. The phase diagram from this study was used because it is consistent with the previous analyses of the Y-H phase system by Blackledge. It should be noted that very little data exists for YH_2 at temperatures below approximately 773 K, especially at/near the phase boundary between the two-phase (metal and dihydride) and single-phase (dihydride) regions. As a result, it is believed that this region represents an area of research that requires further study.

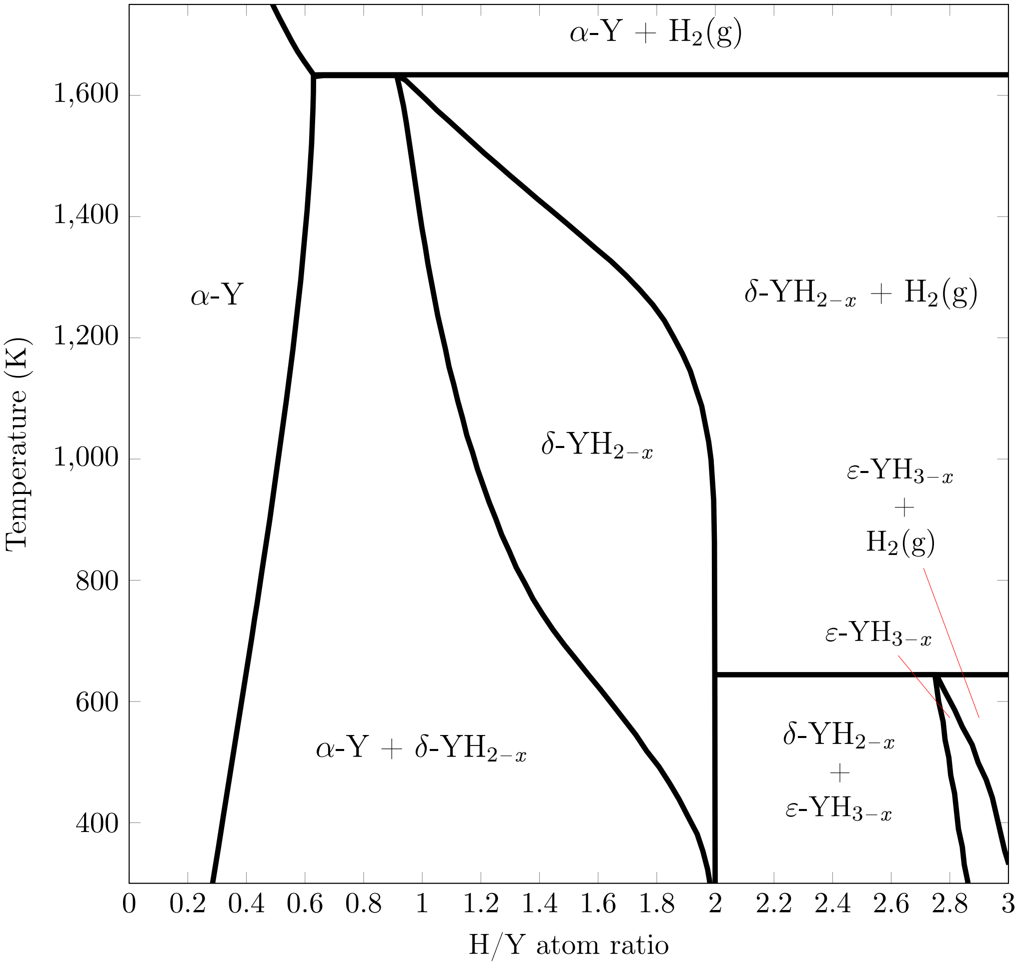

Figure 3-4: Redrawing of the Y-H phase diagram based on CALPHAD analyses by Fu, et al. and Peng, et al. [60, 61] Phase regions are labeled and phase regions have been modified from the original source to temperature in Kelvin as a function of H/Y atom ratio.

3.3 Phase formation kinetics

While hydriding kinetics have been measured for many materials such as titanium, zirconium, and intermetallic compounds for hydrogen storage applications, the formation kinetics of YH_2 have not been explicitly measured [72, 78]. One study in the literature examined the emissivity of a sample of yttrium metal as a function of time when exposed to 0.49 MPa of hydrogen at 528 K, though the result was unclear due to the formation of YH_3 before complete reaction of yttrium metal to form the dihydride [79]. The application of methods described in literature may be used to characterize the formation of YH_2 from yttrium metal at various temperatures and pressures.

In general, the pure metals that form hydrides are highly electropositive and readily form surface oxide layers. These surface oxides act as barriers for hydrogen diffusion from the gaseous phase to the metal. As hydrogen diffuses to the metal, it reacts with the metal to form the metal hydride, which is accompanied by the characteristic volume expansion associated with metal hydride formation as the hydride ingresses into the metal in a film-like manner [72].

At low temperatures, the solubility of hydrogen in the metal is low, which results in a large hydrogen concentration gradient across the surface [72]. Under these conditions, hydrogen accumulates below the surface oxide layer and, thus, the hydrides nucleate just below the surface oxide layer and grow into the metal. The solubility of hydrogen in the metal increases exponentially with temperature. Therefore, at high temperatures, the hydrogen concentration gradient is shallower and, thus, allows for hydrogen to diffuse further within the metal due to a slower approach to supersaturation at the surface. As a result, other nucleation sites besides the oxide/metal interface become possible such as pathways for fast diffusion like grain boundaries. This results in bulk nucleation of hydrides.

The observed effect of temperature and diffusion pathways on hydriding kinetics makes it clear that surface condition, the presence of impurity phases, heat treatment, and physical form (powder versus monolith) may affect hydriding kinetics significantly. Thus, future investigations into the hydriding kinetics of yttrium to form YH_2 must account for these kinds of effects.

4 Fabrication of yttrium and yttrium dihydride

4.1 Preparation of high-purity yttrium

The first preparation of yttrium metal was by the reduction of yttrium chloride by potassium metal in 1828 by Wohler [80]. Since then, all subsequent methods of preparing yttrium metal have been variations of the metallothermic reduction of yttrium halides.

Yttrium halide synthesis from high-purity oxide The Ames Laboratory led the production of yttrium metal based on demand from the U.S. Atomic Energy Commission as part of the Air Force Nuclear Propulsion Program. Researchers at Ames Lab developed several methods of preparing yttrium metal from yttrium halides. Detailed descriptions of these methods may be found elsewhere [81], but some of these methods are briefly summarized here. The starting material for yttrium metal production is yttrium(III) oxide (Y_2O_3). High-purity rare-earth oxides (including yttrium) are prepared using ion-exchange methods. The oxide is then converted to yttrium fluoride (YF_3) or yttrium chloride (YCl_3). High-purity YF_3 is prepared by Ames Laboratory by direct reaction of the oxide with high-purity anhydrous hydrogen fluoride (HF) gas. Commercially, YF_3 may be prepared by the reaction of yttrium(III) oxide with ammonium bifluoride ($NH_4F \cdot HF$). Yttrium metal resulting from YF_3 produced using ammonium bifluoride has been shown to have a higher oxygen content, as compared with material produced using the gaseous hydrogen fluoride route [81]. YCl_3 may be prepared by the reaction between yttrium(III) oxide and either chlorine gas (Cl_2) or carbon tetrachloride (CCl_4).

The high-purity yttrium halides are further purified. YF_3 may be purified using a molten-salt method, where the fluoride is mixed with a fluxing salt and then exposed to anhydrous hydrogen fluoride gas. YCl_3, on the other hand, may be vacuum distilled or may be melted and then filtered under an argon atmosphere.

Reduction of yttrium halides with calcium The primary method of producing high-purity yttrium metal is reduction of YF_3 or YCl_3 using calcium or lithium metal [81]. In this method, a charge of compacted YF_3 and calcium is placed in a tantalum crucible and heated to approximately 1873 K. All processing is done in an inert environment, due to the ability of calcium to oxidize rapidly. At the Ames Lab, calcium metal is distilled under helium and stored in a glovebox for further processing. Tantalum crucibles generally adhere to ASTM B708 – 12. After the charge is cooled, the slag may be removed, and the yttrium remelted under vacuum and cast as an ingot.

Yttrium-magnesium intermediate alloy process Another method of producing high-purity yttrium metal is through the formation of an yttrium-magnesium alloy [81]. In this process, a charge of high-purity YF_3, calcium chloride ($CaCl_2$), calcium metal, and magnesium metal, is heated in a zirconium crucible at 1273 K. At this temperature, an yttrium-magnesium alloy forms and separates from the slag. Heating to 1473 K enables further separation of magnesium and unreacted calcium. Heating cycles are employed to further separate the magnesium and calcium. The use of a calcium-lithium alloy as a co-reductant has also shown promising results due to the formation of a low-melt-point mixture of calcium fluoride and lithium fluoride. The resultant yttrium metal may be cast or extruded into desired shapes.

Fabrication of yttrium and yttrium dihydride

4.2 Direct hydriding of yttrium metal

Previous documents by Van Houten describe the process of directly hydriding metals to produce crack-free hydrides [11]. They are briefly summarized here.

Historically, the fabrication of crack-free metal hydrides has been complicated by a variety of issues. Firstly, hydriding at high temperatures generally causes initial hydride nucleation at the surface, which is then followed by undesirable directional hydride grain growth towards the center of a work piece. Additionally, the procedure to make a crack-free metal hydride requires well characterized PCT curves and, thus, phase diagrams for the metal-hydrogen system of interest.

- Metal/hydride phase boundaries are typically not vertical with temperature except at low temperatures.
- The hydriding reaction is exothermic, which causes localized thermal, hydrogen, and strain gradients.
- The PCT relationships enable large changes in hydrogen concentration with small changes in temperature such that cooling is accompanied by rapid hydrogen absorption.

The coupling of these issues necessitates controlled temperature steps to ensure adequate hydrogen absorption while also balancing hydrogen, thermal, and stress gradients to mitigate localized volume changes that can result in distortion.

Another issue that has been seen in historical hydride fabrication is anisotropic expansion during hydriding. For example, complete hydriding of zirconium is accompanied by a volumetric expansion of approximately 17%, but hydriding of a zirconium cube could result in 8% expansion in both the x- and y-directions, but only a 1% expansion in the z-direction. This is because prior metal grains in cast microstructures are typically large and hydride grains typically grow into the metal with a columnar grain morphology. To mitigate this, the prior metal microstructure should be comprised of small, randomly oriented metal grains. In the past, this was achieved using ceramic grain refiners, such as carbides and borides. Hydrided bodies fabricated using these additives exhibited much finer dimensional control that are crack free, and the as-hydrided bodies are much easier to machine than the pure hydride.

In more recent work, Setoyama, et al. demonstrated the ability to produce crack-free yttrium dihydride (YH_2) using a Sieverts apparatus [24, 28]. These samples were measured for elastic and thermo-physical properties. In methods detailed by Hu et al., crack-free YH_2 was fabricated by exposing high-purity yttrium to ultra-high purity hydrogen gas at low flow rates and tuning the hydrogen partial pressure to the temperature. This maintains the PCT relations by cooling on an isochore (constant composition) by varying the hydrogen pressure to match the desired composition. In principle, this is identical to the methods detailed by Van Houten. The full details of the hydriding procedure may be found in [13].

4.3 Powder metallurgy of yttrium dihydride

Historical approaches to powder metallurgy were limited due to the sheer number of hydriding furnaces available for these projects and the ease with which directly-hydrided components could be produced [82]. For producing YH_2 by powder metallurgy, Van Houten has described a method by which yttrium trihydride is consolidated and then converted to YH_2 by sintering or hot pressing [11].

Fabrication of yttrium and yttrium dihydride

Shivprasad et al. have shown that powder metallurgy processes to produce YH_2 are possible [6]. Mechanical and thermophysical property measurements of the sintered monoliths showed results consistent with those obtained from directly-hydrided yttrium, indicating the feasibility of the powder metallurgy process to produce high-quality YH_2. Further details of these methods may be found in [6]. Briefly, the metal hydride, which does not have to be crack free, is size-reduced in an inert, argon glovebox, compacted into a green body (typical green densities on the order of 70% theoretical density), and then sintered under a hydrogen-containing atmosphere at high temperatures. Powder metallurgical methods for the production of YH_2 have several advantages:

1. Large yttrium castings are not readily, commercially available for producing reactor-scale components.

2. Yttrium castings tend to have large, directionally solidified grains. Direct hydriding leads to a phase change accompanied by a large, anisotropic volume expansion unless grain refinement is done prior to hydriding. This may result in cracks and large residual stresses in the final component.

3. The anisotropic volume expansion results in final parts with unpredictable sizes, which necessitates post-hydriding machining that has the potential for safety incidents due the pyrophoricity of YH_2 powders.

4. Processing of castings is required to refine the grain size and improve homogeneity.

5. Powder processing of YH_2 results in final products that are independent of preexisting yttrium metal microstructure and physical form. Therefore, YH_2 of irregular sizes and geometries may be used in lieu of large castings.

6. The sintered microstructure exhibits significant grain refinement to inhibit directional hydride grain growth at elevated temperatures.

7. Fabrication of composite microstructures, such as fuel-moderator composites, is relatively straightforward.

The principal disadvantage to the process is that it requires inert, argon glovebox handling and processing of YH_2 powder, due to the air-sensitive nature of the size-reduced material. Additionally, the sintered microstructure is relatively complicated, as compared with that of directly hydrided yttrium.

5 Properties of unirradiated yttrium dihydride

This section primarily focuses on physical property characterization of yttrium dihydride (YH_2) in the unirradiated state. These include properties such as heat capacity, thermal expansion coefficient, thermal conductivity, and elastic moduli; all of these properties might be measured during post-irradiation examination, so this section serves as a reference for characterizing as-fabricated YH_2 and comparing with results obtained post-irradiation.

5.1 Heat capacity

Heat capacity has been measured experimentally and density functional theory (DFT)-based methods allow for simulation of this property. Flotow et al. measured the heat capacity at low temperatures (5 – 350 K) using an adiabatic calorimeter and cryostat [83]. Parker also reported heat capacity, as measured using an ice calorimeter, in the temperature range of 273 to 1081 K [23]. More recently, Ito et al.; Shivprasad et al.; and Trofimov et al. measured the heat capacity of YH_2 using differential scanning calorimetry (DSC) [6, 26, 28]. Ito et al. and Trofimov et al. measured heat capacity for various stoichiometries of YH_2, while Shivprasad et al. measured the heat capacity of near-stoichiometric sintered samples and compared experimental results with those calculated using DFT. A summary of these measurements and calculations is shown in Figure 5-1. The heat capacities of samples with lower- and upper-limit hydrogen concentrations from Trofimov et al. are plotted to show trends with hydrogen content. Figure 5-1 shows that there exists a significant degree of consistency between experimental data across various studies. Particularly, the data from Flotow et al., Parker, Shivprasad et al., and Trofimov et al. appear to overlap with one another for hydrogen contents near 2.0 H/Y units. The experimental data from Ito et al. show higher molar heat capacities, even exceeding the Dulong-Petit limit for the heat capacity. It is believed that the data presented by Flotow et al., Parker, Shivprasad et al., and Trofimov et al. represent the more correct values. It is also observed that the results of DFT modeling by Shivprasad et al., which only includes contributions from harmonic lattice vibrations, are also consistent with the experimental data up to a temperature of approximately 700 K. Above this temperature, the modeling results and experimental data appear to diverge. This could be due to changes in hydrogen content experimentally from passing from the two-phase to the single-phase region or, as was hypothesized by Shivprasad et al., to the initial formation of Frenkel pair defects [25]. Trofimov et al. similarly hypothesized that the divergence, shown as a peak in the heat capacity data, was due to an order-disorder transition [26]. However, more studies are required to understand the dependence of the molar heat capacity with temperature in this higher-temperature regime.

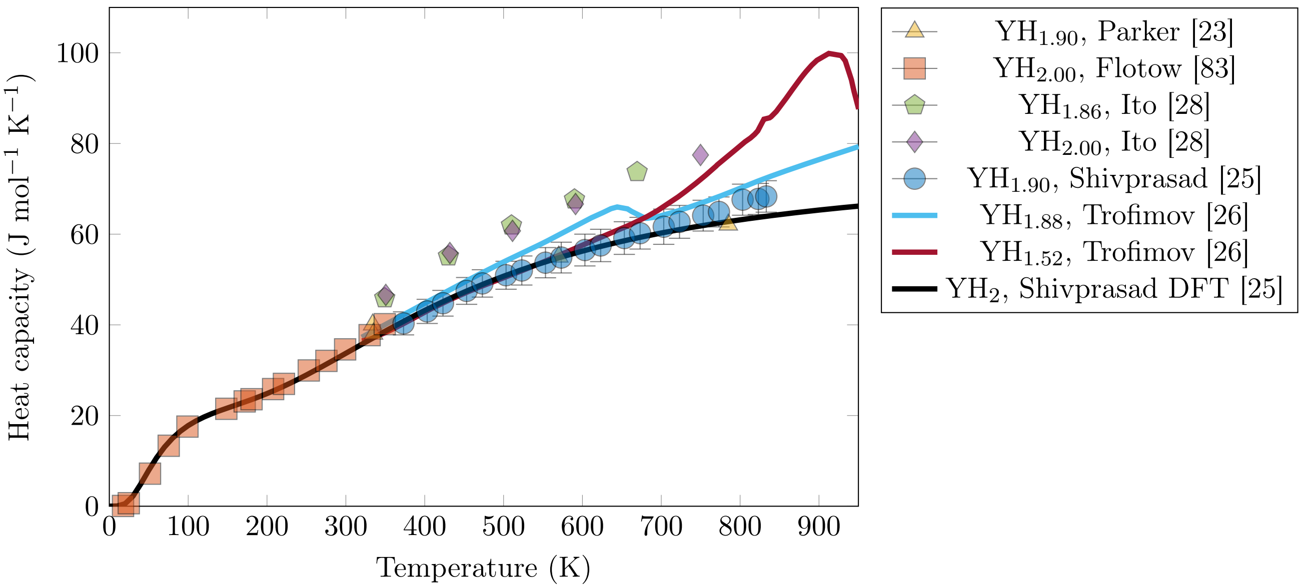

Figure 5-1: Molar heat capacity of yttrium dihydride as a function of temperature. Complete data sets are not shown here for ease of viewing. Data points are made translucent to view overlapping data sets.

5.2 Thermal expansion

5.2.1 Definitions of thermal expansion coefficient

Thermal strain The thermal strain as a function of temperature, ϵ_T, is defined as the normalized thermal expansion with reference to a temperature, T_0. The thermal strain, by definition, is a function of temperature. Here, the thermal strain at the reference temperature is typically defined as zero.

$$\epsilon_T(T) = \frac{\ell(T) - \ell_0}{\ell_0} \tag{13}$$

where $\ell(T)$ is the length at temperature, T, and ℓ_0 is the length at temperature, T_0.

Across the various studies that have examined the thermal expansion of YH_2, two different methods for reporting the coefficient of thermal expansion (CTE) are used. This has caused some confusion as to which values of CTE as a function of temperature are correct. Here we seek to clarify the two different, but related, definitions of CTE.

Secant coefficient of thermal expansion A common way to describe thermal expansion is using a linear, or secant, model that averages the thermal strain over a particular temperature range. Thus, the secant CTE, α_S, is a function of temperature and is defined using the following relationship:

$$\epsilon_T(T) = \alpha_\mathrm{S}\,(T - T_0)$$

or

$$\alpha_\mathrm{S}(T) = \frac{\epsilon_T}{T - T_0} \tag{14}$$

Instantaneous coefficient of thermal expansion Another common way to describe thermal expansion is to relate it to the instantaneous expansion as a function of temperature.

$$\alpha_{\mathrm{I}}(T) = \frac{d\epsilon_T}{dT} = \frac{1}{\ell_0}\frac{d\ell}{dT} \tag{15}$$

Relating secant and instantaneous thermal expansion coefficients Because the literature thermal expansion data is reported as the two different types of coefficients, it is important to understand how to convert the data between these two. This can be accomplished by differentiating the definition of the secant CTE.

$$\epsilon_T = \alpha_{\mathrm{S}}(T - T_0),\ \frac{d\epsilon_T}{dT} = \alpha_{\mathrm{I}}$$

$$\alpha_{\mathrm{I}} = \frac{d\epsilon_T}{dT} = \frac{d}{dT}\left[\alpha_{\mathrm{S}}(T - T_0)\right]$$

This simplifies to the following expression:

$$\alpha_{\mathrm{I}} = \frac{d\alpha_{\mathrm{S}}}{dT}(T - T_0) + \alpha_{\mathrm{S}} \tag{16}$$

Evaluating the instantaneous CTE at a temperature, T_1, can thus be achieved as follows:

$$\alpha_{\mathrm{I}}\Big|_{T_1} = \frac{d\alpha_{\mathrm{S}}}{dT}\Big|_{T_1}(T_1 - T_0) + \alpha_{\mathrm{S}}\Big|_{T_1}$$

Conversely, through the definition of the instantaneous CTE, it is simple to convert this quantity to the secant CTE:

$$\epsilon_T(T) - \epsilon_T(T_0) = \int_{T_0}^{T} \alpha_{\mathrm{I}}(T')\, dT'$$

Because $\epsilon_T(T_0)$ is typically defined as zero, this expression can be combined with Equation (14) to give

$$\alpha_{\mathrm{S}} = \frac{1}{T - T_0}\int_{T_0}^{T} \alpha_{\mathrm{I}}(T')\, dT' \tag{17}$$

5.2.2 Thermal expansion data for yttrium dihydride

As with heat capacity measurements, thermal expansion data are similarly limited. Historical data for YH_2 thermal expansion are found in studies by Lundin et al. and Parker; both of these studies used dilatometric methods to measure the secant CTE of YH_2 [23, 84]. More recently, Setoyama et al., Ito, Shivprasad et al., and Trofimov et al. measured thermal expansion using XRD, neutron diffraction, and dilatometry, respectively [24–26, 85]. Setoyama, Ito, and Trofimov all reported secant CTEs, while Shivprasad reported instantaneous CTE. A compilation of all this data is shown in Figure 5-2, which compares (a) the thermal strain, (b) instantaneous CTE, and (c) secant CTE of YH_2 across all studies.

All CTEs show consistency in values and in functional behavior with temperature. The experiments by Lundin et al. and Shivprasad et al. measured data at high temperature, showing that at a temperature of 800 K, the dependence of the CTE with temperature appeared to change. Shivprasad et al. hypothesized that this change may be due to the formation of Frenkel pair defects,

Table 5-1: Empirical fitting parameters for the instantaneous thermal expansion coefficient as a function of temperature. Fitting parameters are given with 95% confidence intervals.

Temperature range (K)	Temperature unit (-)	A (10^{-5})	B (10^{-6})	C (10^{-7})	D (10^{-6})
298-1000	$\frac{T-698.0}{203.6}$	1.44 ± 0.05	2.10 ± 0.76	6.13 ± 3.82	1.30 ± 0.38

Table 5-2: Empirical fitting parameters for the secant thermal expansion coefficient as a function of temperature. Fitting parameters are given with 95% confidence intervals.

Temperature range (K)	Temperature unit (-)	A (10^{-5})	B (10^{-6})	C (10^{-7})	D (10^{-6})
298-1000	$\frac{T-699.2}{203.2}$	1.16 ± 0.02	2.18 ± 0.34	-0.07 ± 0.16	0.10 ± 0.15

as their formation is accompanied by a volume expansion, which would be reflected in the thermal expansion. This change appears to correlate with temperatures where the heat capacity increases in the data by Trofimov, et al., though there are differences in hydrogen content between the two studies and this discrepancy will cause shifts in these temperature regimes. Another possibility relating to the sharp increase in CTE is a softening of phonon modes, which has produced anomalous thermal expansion data in other materials [86, 87].

Shivprasad et al. provided empirical fits for the two temperature regimes considered for thermal expansion, as the CTE appeared to follow two different regimes. These were fit using equations with the following form: $\alpha_P = A+BT+CT^2$. Hu et al. fit the Transformational Challenge Reactor (TCR) CTE data to a function with the following form: $\alpha = A + BT + CT^2 + DT^3$ [88]. Here, we have taken a similar approach as Hu et al: we have fit the instantaneous and secant CTE data across many studies. Both data sets were fit using a third-order polynomial. For both fits, temperature units were centered and scaled to the full span. These fits are shown for near-stoichiometric YH_2 in Figure 5-2 and fitting parameters are summarized in Tables 5-1 and 5-2. The CTE of $YH_{1.61}$ from the TCR program is shown in Figure 5-2 for comparison, but was not used to produce fits. For the analysis of the secant CTE data, the values from Ito were discarded, as they were much higher than values of other studies, where the data were much more consistent across the other studies. The data was normalized to the central point of the data and fit using a bisquare weights method in MATLAB (Mathworks, Natick, MA, USA).

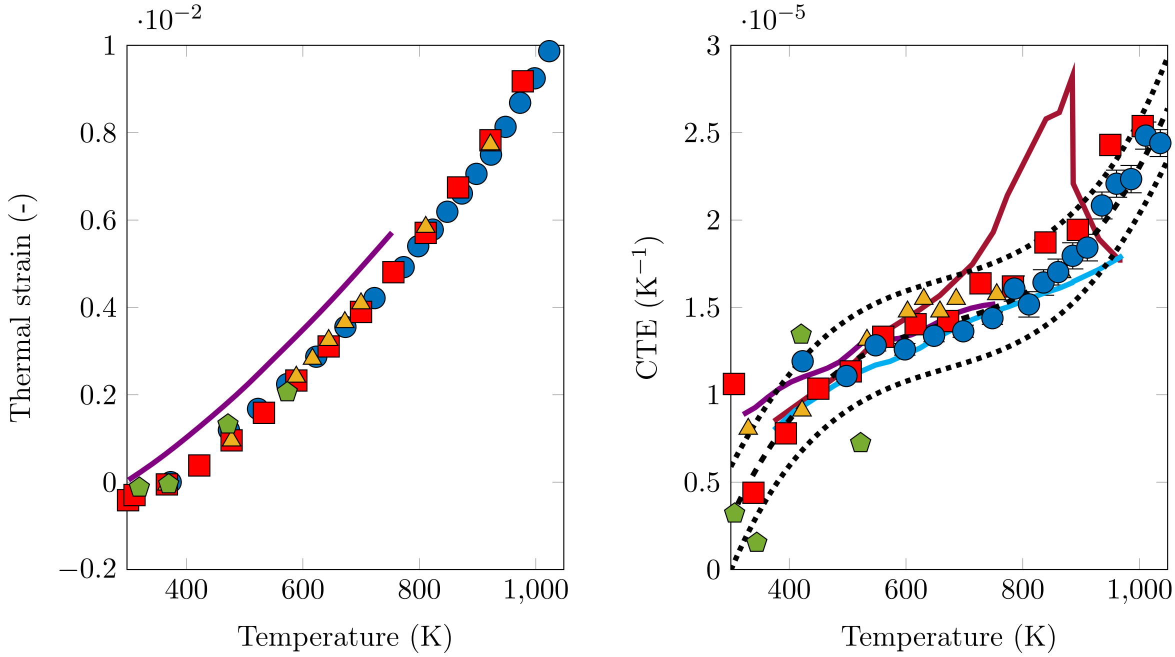

(a) Thermal strain

(b) Instantaneous CTE

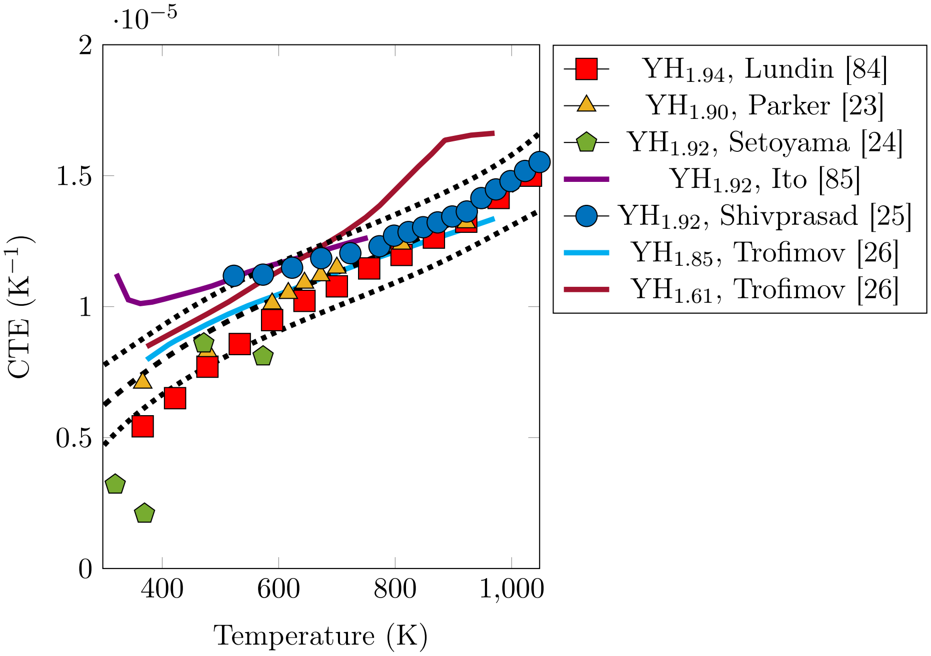

(c) Secant CTE

Figure 5-2: Thermal expansion data for yttrium dihydride. (a) Thermal strain, (b) instantaneous coefficient of thermal expansion, and (c) linear coefficient of thermal expansion. Thermal expansion coefficients were fit to functions of temperature. The fitting parameters for these are summarized in Tables 5-1 and 5-2.

5.3 Thermal conductivity

Four experimental measurements of the thermal conductivity of YH_2 exist. Parker measured this property as a function of temperature for $YH_{1.77}$ using a heat flow method and apparatus [23]. Ito et al., Shivprasad et al., and Trofimov et al. calculated thermal conductivity from experimentally-measured CTE, thermal diffusivity, and heat capacity [6, 26, 28]. Reported values from these studies are plotted in Figure 5-3, which plots thermal conductivity in Figure 5-3(a) along with the calculated thermal resistivities in Figure 5-3(b). The results from Ito et al., Shivprasad et al., and Trofimov et al. appear to be consistent, while the thermal conductivity values from Parker are much lower. Indeed, the values provided by Parker are closer to values expected for yttrium metal than YH_2. The thermal conductivity and resistivity provided by Trofimov, et al. used a heat capacity and CTE that spanned a hydrogen order-disorder transition [26, 88]. However, energy associated with that transition is primarily in hydrogen defects [25], which do not contribute to the thermal transport of the lattice. As a result, it is believed that the values by Ito et al. and Shivprasad et al. are more representative of the true thermal conductivity of the material.

By assuming phonon heat transport dominates, a linear fit of the thermal resistivity calculated by Ito and Shivprasad for near-stoichiometric YH_2 is provided in Equation (18) with 95% confidence intervals. Deviations from the trend by the experimental data could be due to other contributions to thermal conductivity, such as electronic or ionic heat transport. In the linear fit given in Equation (18), the y-intercept term represents the athermal scattering process, such as defect-phonon scattering, while the slope term represents phonon-phonon scattering processes.

$$R_\lambda(\mathrm{m\,K\,W^{-1}}) = (6.50\times10^{-3}\ \pm\ 1.70\times10^{-3}) + (2.61\times10^{-5}\ \pm\ 0.25\times10^{-5})\,T(\mathrm{K}) \tag{18}$$

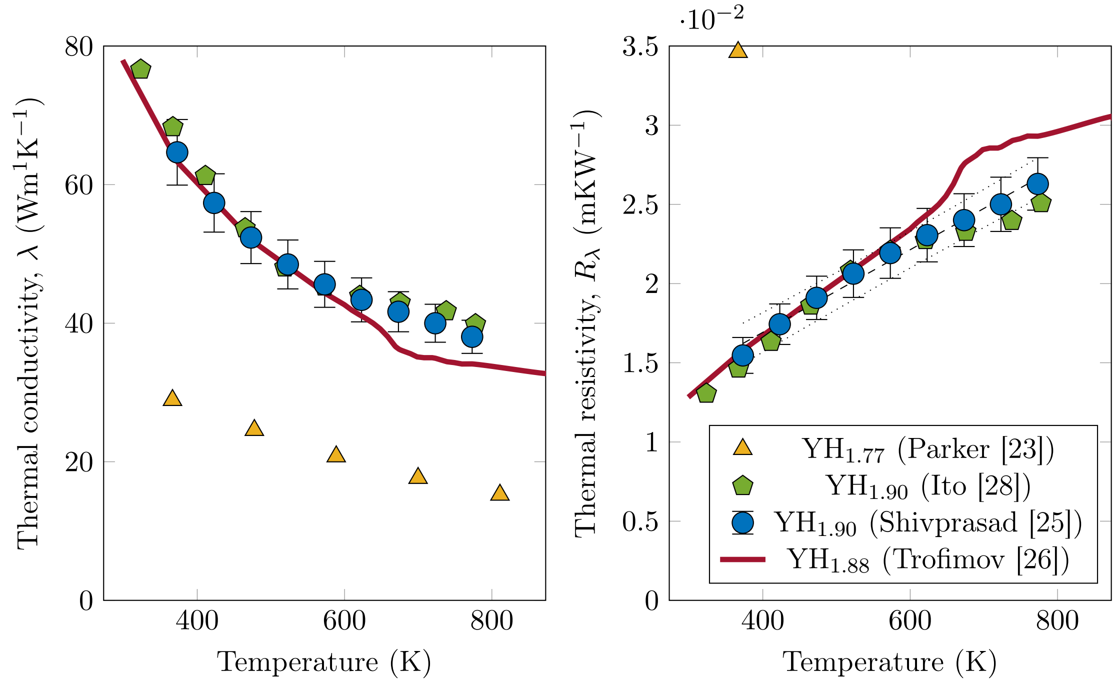

(a) Thermal conductivity

(b) Instantaneous CTE

Figure 5-3: (a) Thermal conductivity and (b) thermal resistivity. Thermal resistivity was fit to a function of temperature. The fitting parameters for these are summarized in Equation (18). Note that the thermal resistivity calculated by Parker is off the scale of the other studies.

5.4 Emissivity

The emissivities of yttrium hydrides have been measured qualitatively. The infrared emissivity of yttrium was measured as a function of exposure time when exposed to 490 kPa of pure hydrogen at 528 K [79]. Normalized emissivity values showed that emissivity increased with hydrogen content and exposure time and increased with phase transformations to the dihydride and the subsequent trihydride phases. It is difficult to extrapolate emissivities of YH_2 from these measurements, as the phase contents did not appear to follow a strict metal to dihydride to trihydride progression. Rather, by 10 minutes of exposure to hydrogen, the phase mixture consisted of yttrium metal and YH_2, after which point yttrium trihydride (YH_3) began to form, indicating that the system consisted of two to three phases at any point when YH_2 was present.

5.5 Electrical properties

Electrical property measurements have been performed for yttrium hydrides because of their use in switchable mirror applications, where changes in electrical properties are correlated with changes in optical properties. Because electrical properties do not significantly impact nuclear reactor performance, a cursory summary is presented here. Weaver et al. measured the dielectric constant of YH_2 as approximately 4.8 [89]. This value increases for higher concentrations, with the dielectric coefficient for YH_3 of 10 [90]. This is consistent with the understanding that the dihydride is well known as having metallic character, while the trihydride is a semiconductor [91]. The charge carrier concentration of $YH_2$was measured by Sakai et al. as between 1.1 and $1.4 \times 10^{27}\,\mathrm{m}^{-3}$ [92]. Sakai et al. also measured the electrical resistivity of YH_2 as approximately $8.4 \times 10^{-12}\,\Omega\,\mathrm{m}$. With higher hydrogen stoichiometries in the two-phase (dihydride + trihydride) region, Vajda et al. measured a significant increase in electrical resistivity. For $H/Y = 2.065$, the electrical resistivity was measured as $8.4 \times 10^{-7}\,\Omega\,\mathrm{m}$ at 283 K and for $H/Y = 2.07$, the electrical resistivity was measured as approximately $1.85 \times 10^{-6}\,\Omega\,\mathrm{m}$ at 256 K [93]. For hydrogen stoichiometries close to (but above) $H/Y = 2.00$, the hydride was found to be a metal at low temperatures, but still transitioned to a semiconductor at temperatures below room temperature [94, 95]. This transition temperature was found to decrease as a function of increased hydrogen content. These data have been evaluated for validity by other sources [96–99].

5.6 Magnetic properties

Magnetic property measurements of YH_2 have been summarized more thoroughly in other reviews [100]. Because they do not significantly impact nuclear reactor operation, a qualitative summary is presented here. Arons summarized that, in general, the rare earth dihydrides exhibit an antiferritic structure, but that this structure changes ordering with hydrogen stoichiometry [100]. Additionally, because measured hydrogen contents are relatively inaccurate, true dependence of the magnetic properties with hydrogen content are difficult. Magnetic properties, including proton spin relaxation times were found to depend on the impurity content with even 100 ppm of rare earth additions significantly impacting these values [30]. It was also observed that different additions affected the relaxation times to differing degrees, with the purest yttrium having the longest relaxation time and relaxation time decreased with additions in this order: cerium, dysprosium, erbium, neodymium, gadolinium. Because the proton spin relaxation time measurement is used to determine hydrogen self-diffusion coefficients, it is believed that diffusion measurements of hydrogen in YH_2 may have been significantly impacted by impurities. A more detailed description of the nuclear magnetic resonance (NMR) technique and the different relaxation times is given in section 5.8, as it relates to the determination of hydrogen self-diffusion parameters through YH_2.

5.7 Mechanical properties

Until recently, mechanical testing data of YH_2 have been relatively limited, primarily due to the difficulty in fabricating bulk, crack-free specimens. Nevertheless, the limited studies on elastic properties and hardness are presented below.

Short-term tensile testing of YH_2 was performed as part of the Aircraft Nuclear Propulsion program, though the program noted the difficulty in performing these tests, due to the brittle nature of the material and high temperature testing was performed in hydrogen-containing atmospheres to maintain stoichiometry [23]. Briefly summarized here, the results of short-term tensile testing showed nearly zero elongation at temperatures up to approximately 1273 K but were able to measure up to 5.5% elongation at nearly 1473 K and an 18% reduction in area at the same temperature. Parker noted that, for near-stoichiometric YH_2, the yield strength could not be measured and the variation in the ultimate tensile strength was nearly 100% of the measurement.

Equibiaxial flexural testing of YH_2 was performed under the TCR program for geometries representative of the moderator for the TCR design. No significant trend was observed as a function of hydrogen content in the range of 1.00 to 1.87 H/Y units, though the mean failure strength was calculated to range between 50 and 95 MPa for 5.8 mm diameter samples with a nominal thickness between 0.5 and 0.625 mm [88].

5.7.1 Elastic moduli

The elastic moduli of YH_2 are commonly determined through sound speed or resonant ultrasound spectroscopy (RUS) measurements. Beattie et al. measured the elastic moduli of $YH_{1.93}$ using sound speed measurements in the temperature range 80-300 K and observed an inflection around 230 K possibly due to proton ordering on tetrahedral sites [42]. Setoyama et al. measured the moduli of various YH specimens as a function of hydrogen content (H/Y between 1.6 to 2.3), finding that the moduli increase linearly with H/Y [24]. Similarly, Hu et al. observed a linear dependence of the elastic moduli with H/Y [101]. We also note there exists a significant body of work done to calculate the elastic moduli using DFT with modeled results in significant agreement with experimental values for fully-dense material [6, 43–46]. The results of various elastic modulus measurements are plotted in Figure 5-4 as a function of hydrogen stoichiometry. Results for shear modulus (G), the bulk modulus (K), and the Young's modulus (E) as a function of hydrogen content were fit to linear functions of hydrogen-to-yttrium atom ratio (X) and are summarized as follows with 95% confidence intervals for the fitting parameters:

$$G(\mathrm{GPa}) = (20.0 \pm 8.9) + (18.1 \pm 4.8)\,\mathrm{X} \tag{19}$$

$$K(\mathrm{GPa}) = (21.0 \pm 27.4) + (34.1 \pm 14.8)\,\mathrm{X} \tag{20}$$

$$E(\mathrm{GPa}) = (16.1 \pm 33.6) + (61.7 \pm 18.2)\,\mathrm{X} \tag{21}$$

It should be noted that the confidence intervals for the bulk and Young's moduli are significantly larger than for the shear modulus; as Shivprasad et al. showed, many of the resonances required to measure the elastic moduli have predominantly shear characteristics [6]. That is, material resonances from which the elastic moduli are calculated predominantly depend on shear modes. As a result,

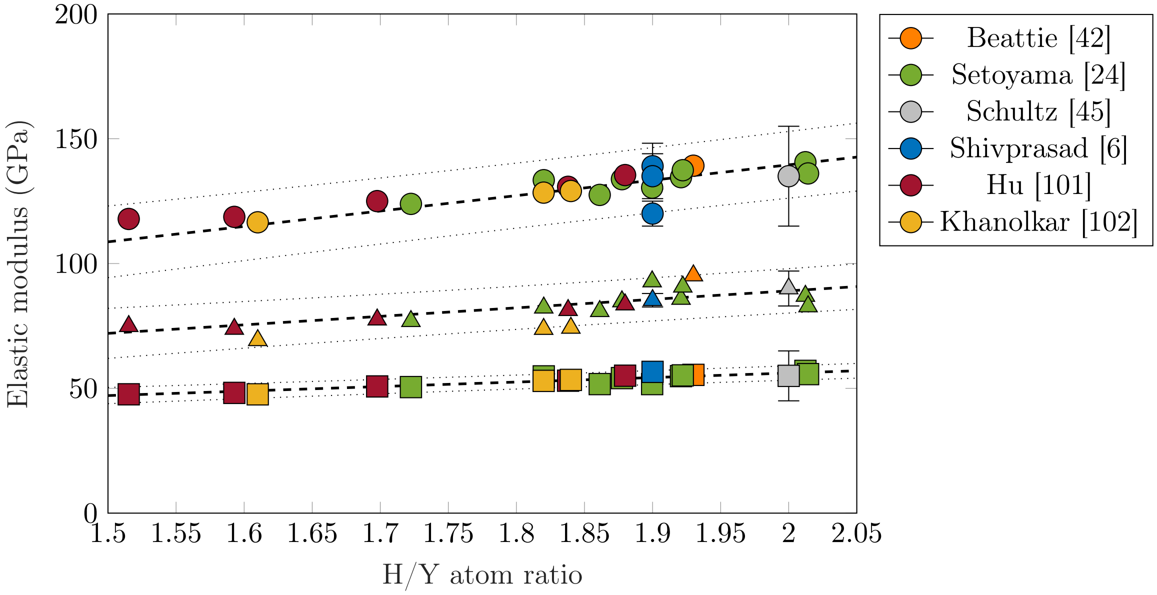

Figure 5-4: Shear (G), bulk (K), and Young's (E) moduli as a function of hydrogen content for yttrium dihydride. Young's modulus is plotted in circles, bulk modulus is plotted in triangles, and shear modulus is plotted in squares.

further characterization of the elastic moduli to stoichiometries lower than $H/Y = 1.90$ is required to better characterize the dependence of these moduli on hydrogen content. Shivprasad et al. demonstrated that the moduli of sintered-YH_2 monoliths decrease linearly as a function of monolith porosity (90-100%) [6]. These results are given in Figure 5-5, in which it is apparent that the elastic moduli of YH_2 decrease with increasing porosity. It is also observed that the dependence on porosity extrapolates to elastic moduli values very close to values obtained from fully dense YH_2. As a result, it is believed that these values and fits are valid. These results have been fit as functions of porosity and are given as follows with 95% confidence intervals for the fitting parameters:

$$G(\text{GPa}) = (56.60 \pm 3.64) - (180.34 \pm 70.81)\,p \tag{22}$$

$$K(\text{GPa}) = (85.34 \pm 2.68) - (307.12 \pm 52.03)\,p \tag{23}$$

$$E(\text{GPa}) = (139.02 \pm 9.23) - (449.88 \pm 179.44)\,p \tag{24}$$

As with the fits of elastic moduli as a function of hydrogen concentration, the confidence intervals for the bulk and Young's moduli are much larger than for the shear modulus due to many of the resonance modes correlating with shear characteristic.

Khanolkar, et al. performed a study using laser RUS to measure the elastic moduli of YH_2 as a function of temperature [102]. For this study, the samples used were the same as the ones produced by Oak Ridge National Laboratory for the TCR program and, thus, are of a similar pedigree to those studied by Hu, et al. and Trofimov, et al. Khanolkar found linear fits for the elastic moduli as a function of temperature. These fits have been redone here to convert the temperature to degrees Kelvin and to provide error bars for the fitting parameters. Khanolkar's data has been re-plotted with revised fits in Figure 5-6. Equations for the fits for shear, bulk, and Young's moduli as a function of temperature are given in Equations (25) to (27). The Poisson's ratios from these fits varied between 0.196 and 0.222 as a function of temperature. It should be noted that the vertical

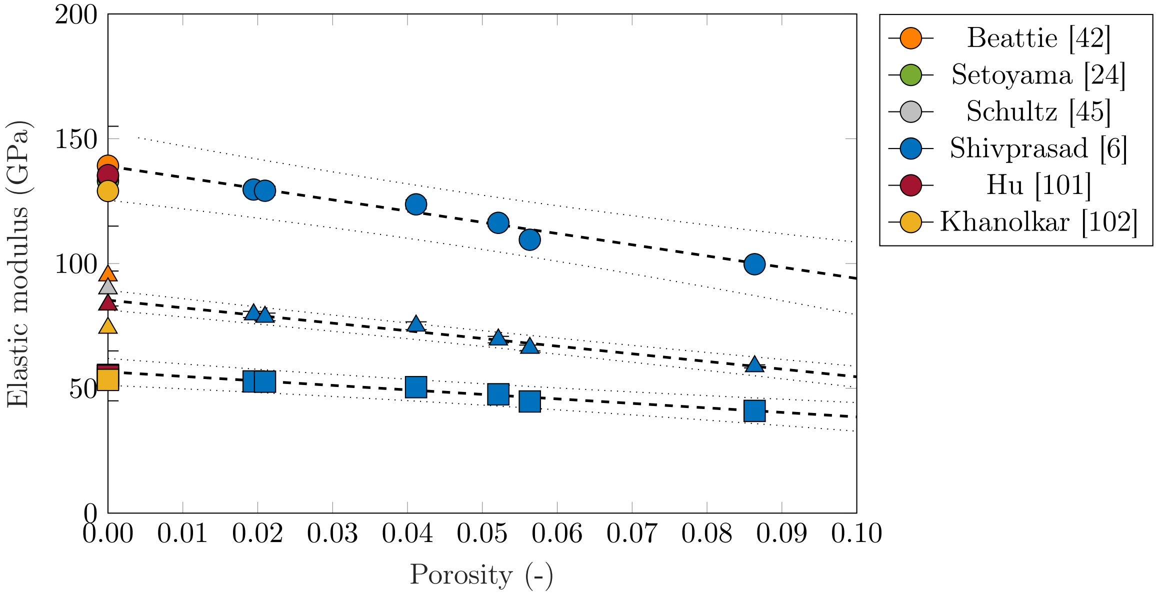

Figure 5-5: Shear (G), bulk (K), and Young's (E) moduli as a function of porosity for near-stoichiometric yttrium dihydride, YH_2. Young's modulus is plotted in circles, bulk modulus is plotted in triangles, and shear modulus is plotted in squares.

intercepts for the equations in Equations (25) to (27) are different from those provided by Khanolkar, as the equations presented here use temperature units of Kelvin and, thus, extrapolate values to absolute zero. The slopes, however, are consistent.

$$G(\text{GPa}) = (56.01 \pm 1.55) - (6.98 \times 10^{-3} \pm 1.9 \times 10^{-3})\,T \tag{25}$$

$$K(\text{GPa}) = (74.67 \pm 2.69) - (4.62 \times 10^{-3} \pm 3.2 \times 10^{-3})\,T \tag{26}$$

$$E(\text{GPa}) = (134.4 \pm 2.50) - (1.52 \times 10^{-2} \pm 3.0 \times 10^{-3})\,T \tag{27}$$

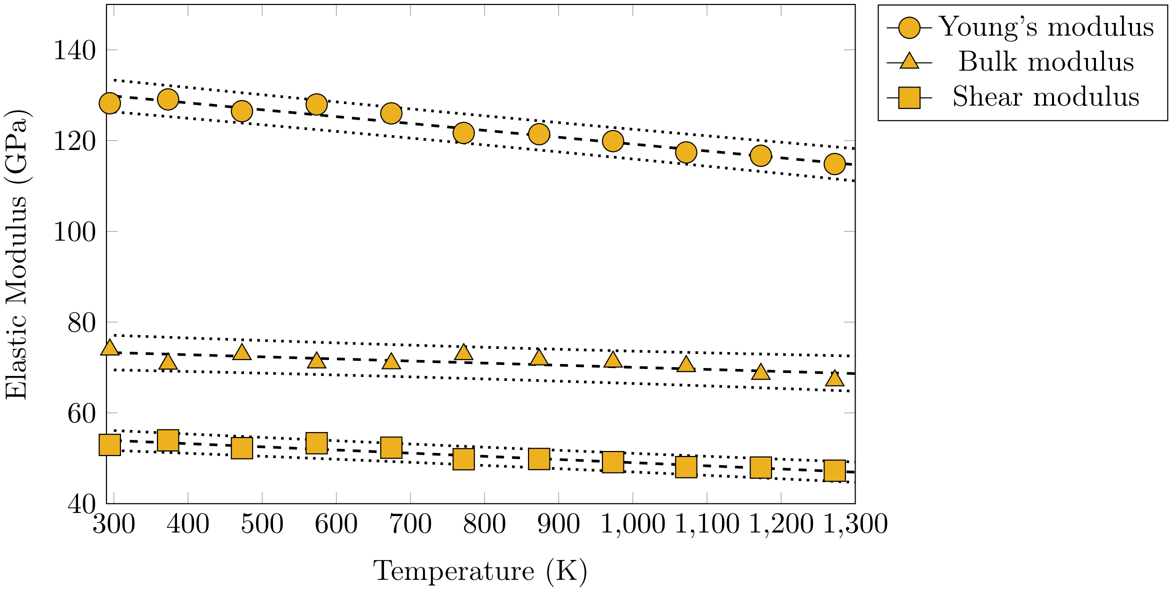

Figure 5-6: Shear (G), bulk (K), and Young's (E) moduli as a function of temperature for near-stoichiometric yttrium dihydride, YH_2. Young's modulus is plotted in circles, bulk modulus is plotted in triangles, and shear modulus is plotted in squares. Data from [102].

5.7.2 Hardness

Detailed studies on the hardness of YH_2 are limited. Funston, Parker, Setoyama et al., and Hu et al. measured hardness as a function of hydrogen content, while Shivprasad et al. measured hardness on YH_2 fabricated by direct-hydriding and powder metallurgical methods [6, 23, 24, 101, 103]. Vickers hardness results are summarized in Table 5-3. Funston, Parker, and Shivprasad et al. examined the hardness of only one stoichiometry of YH, while Setoyama, et al. and Hu, et al. looked at the dependence of the Vickers hardness on hydrogen content. While Setoyama et al. noted a dependence on hydrogen content, the values for H/Y between 1.7 and 1.9 exhibited no significant variation. Conversely, Hu et al. observed a linear trend for H/Y values between 1.5 and 1.9, but their reported values were lower than in other studies. As a result, we believe that further study of hardness as a function of hydrogen content is warranted.

Table 5-3: Summary of Vickers hardness values for yttrium dihydride.

Hydrogen content (H/Y)	Vickers hardness (GPa)	Synthesis route (-)	Ref. (-)
1.4	2.0	Direct hydride	[103]
2.12	2.9	Direct hydride	[23]
$1.7 \leq X \leq 2.0$	3.48 ± 0.86	Direct hydride	[24]
1.90	2.87 ± 0.69	Powder metallurgy	[6]
1.90	3.17 ± 0.07	Direct hydride	[6]
1.88	2.39 ± 0.08	Direct hydride	[88]

5.8 Hydrogen self-diffusion in yttrium hydrides

Although the data are sparse, hydrogen diffusion measurements in yttrium hydrides have been performed using NMR and quasi-elastic neutron scattering (QENS). A brief overview of both techniques is given below to familiarize the reader, which is followed by a summary of relevant diffusion parameters of YH_2.

5.8.1 *Description of measurement techniques*

Nuclear magnetic resonance (NMR) ^{1}H-NMR spectroscopy is a non-destructive, bulk measurement technique that measures the precession of hydrogen nuclei and provides insight into chemical composition, spin-spin coupling between adjacent atoms, molecular dynamics, and molecular structure of hydrogen-bearing media. The NMR signal is sensitive to the electronic structure because the number and proximity of nearby electrons affect the local magnetic field at the nucleus. Each nucleus precesses at a unique frequency ω, which is defined as

$$\omega = \gamma B_0 \tag{28}$$

where B_0 is the applied magnetic field and γ is the gyromagnetic ratio, which is characteristic of each nucleus and is representative of the sensitivity of a nucleus in an NMR experiment [104]. During a single measurement, only one nuclide can be observed, as the spectrometer can only detect signal at one frequency.

When a given sample is placed in a strong magnetic field, the nuclear spin aligns with the magnetic field along the z-axis, as is shown in Figure 5-7(a). A radiofrequency (RF) pulse is then applied, which perturbs the spin, aligning it either perpendicular to (x-y plane) or anti-parallel (-z-axis) to the magnetic field, as shown in Figure 5-7(b). Relaxation causes the nuclear spin to be aligned again with the magnetic field along the z-axis (Figure 5-7(c) – (e)) and causes a free induction decay, which is measured and Fourier transformed to give a spectrum. There are two mechanisms of relaxation: spin-lattice relaxation, which is also referred to as longitudinal or T_1 relaxation, and spin-spin relaxation, referred to as transverse or T_2 relaxation [105]. The T_1 relaxation is the recovery of the magnetization along the z-axis and is illustrated in Figure 5-7. This relaxation is typically caused by coupling to the electronic spin of free electrons within the material (i.e., dangling bonds, paramagnetic impurities, dopants, impurities). In pure, crystalline materials, the T_1 relaxation is very long and can take minutes or even hours for full recovery of the magnetization to the z-axis [105]. The T_2 relaxation, on the other hand, is more complex and may be affected by many factors. One such cause will be explained simply here for the sake of brevity. The first is related to the precession of the nuclear spin and is depicted in Figure 5-8: After the RF

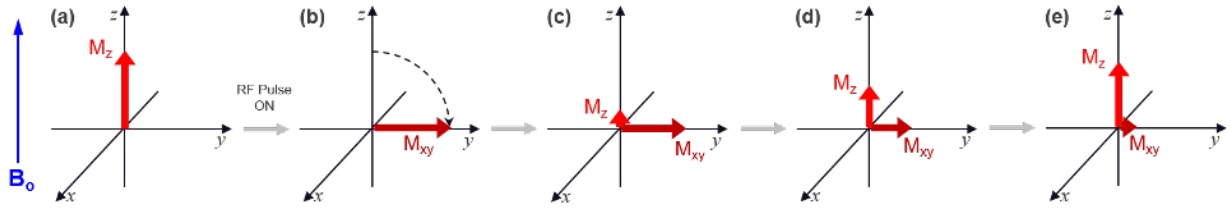

Figure 5-7: Magnetization evolution before and after a pulse of RF radiation is applied. The applied magnetic field is in the direction of the z-axis (up/down).

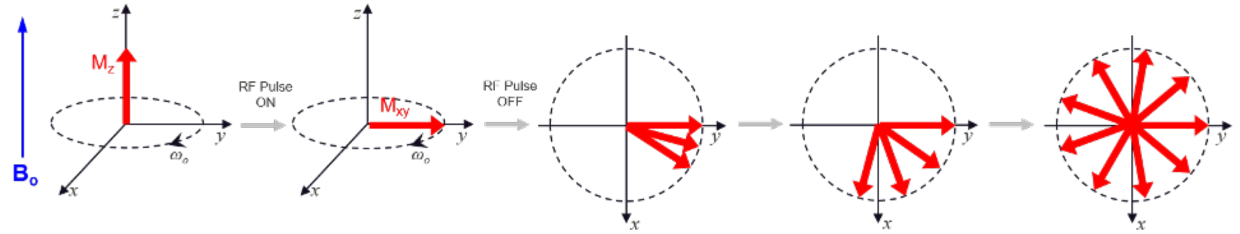

Figure 5-8: Loss of coherence of magnetization in the x-y plane after an RF pulse is applied.

pulse is turned off, the magnetization is aligned along the $+y$-axis, and the nuclear spins begin to precess about the z-axis. If we consider here ^{1}H nuclei in the tetrahedral site in YH_2, all ^{1}H nuclei should be precessing at the same frequency. However, some of the hydrogen atoms many be near a vacancy or an impurity atom, which disturbs the local magnetic field, B_{loc} [105]. The frequency then becomes:

$$\omega = \gamma \left(B_0 + B_{\text{loc}} \right) \tag{29}$$

There is then a loss in phase coherence between the unaffected spins and the affected spins. After some time, the ^{1}H nuclei are resonating at their own frequency, which is due to the differences in the local magnetic field [105]. An analogy for this phenomenon is that of runners in a marathon. Before the race, all runners are lined up, and initially after the start, all competitors are running at the same speed. After time t, some of the runners will be going at a faster pace. Towards the end of the race, the runners are randomly dispersed throughout the racetrack due to their various speeds. Another factor that leads to loss of phase coherence is mobility of the nuclei since hopping from one site to another will drastically change the local magnetic field, and this will lead to a change in the T_2 relative to the case of non-mobile species. The T_2 relaxation time can be approximated as the inverse of the width of the spectral peak. Therefore, if the nuclei in YH_2 become mobile, the T_2 will be affected, thus changing the peak width of the observed signal. This allows for the study of material dynamics because the mobility of a species can be related to the T_2. The dynamics can be studied by solid-state, variable temperature (VT) NMR, which has been applied broadly to determine the rotational dynamics in ionic liquids and glasses [106, 107], the glass transition temperature of glasses and hopping transport in ionic conductors and cathode materials [108, 109].

Quasi-elastic neutron scattering (QENS) QENS is an inelastic neutron scattering technique that measures the very small energy exchanges between incident neutrons and a sample's nuclei, which in turn leads to broadening of the spectrum's elastic line. The probability of a scattering event is gauged by the scattering cross sections of a sample's nuclei. In this context, the scattering cross section of hydrogen (82 barns) is much greater than that of zirconium (6 barns), and so the scattered neutron signal is dominated by the dynamics of hydrogen. The measured energy exchange occurs in the sub-meV range, which corresponds to dynamic processes such as hydrogen self-diffusion in the pico-to-microsecond range. The reader is referred to the book by Marc Bée for a detailed description of the QENS technique [110].

5.8.2 Hydrogen self-diffusion coefficients

Hydrogen diffusion in the hydrogen sublattice of the dihydride is believed to proceed through three potential mechanisms: (1) tetrahedral-tetrahedral (T-T) jumps, tetrahedral-octahedral (T-

O) jumps, and octahedral-octahedral (O-O) jumps. As mentioned above, the dihydride forms when the tetrahedral sites of the crystal fill with hydrogen, while the trihydride forms upon accommodation of further hydrogen into the octahedral sites. However, as also noted above, octahedral site occupation has been observed even at room temperature, though the occupancy factors are small [29, 34]. The mechanism for hydrogen diffusion in yttrium hydrides has been observed to depend on hydrogen content and temperature [29]. Majer, et al. hypothesized that at low hydrogen contents, the hydrogen diffuses predominantly through T-T jumps through a vacancy mechanism. As the hydrogen content increases, the tetrahedral sites become increasingly occupied, which Majer, et al. hypothesized allows for contributions from T-O and O-O jumps [111].

Fukai analyzed the hydrogen diffusion data from QENS and NMR for yttrium and zirconium hydrides (as well as other metal hydrides) and describes that the above hypothesis by Majer, et al. might be consistent for the hydrogen data in zirconium hydrides but is not consistent with the data for hydrogen in YH_2. In fact, Fukai's fit of the diffusion data to models considering T-T, T-O, O-T, and O-O jumps shows the best agreement when only considering O-O jumps with an activation energy of approximately $E_A = 0.39$ eV $\pm\ 0.05$ eV [69]. Fukai hypothesized that, for the rare earth dihydrides (such as YH_2), the hydrogen diffusion also exhibits some degree of coordinated motion that depends on the metal-to-ionic transition of the compound and atomic ordering. However, this coordinated motion manifests more clearly at high hydrogen concentrations. This behavior is consistent with what was observed by Mehta, et al. experimentally using neutron diffraction [46].

The diffusion of hydrogen in YH_2 is also complicated by the fact that, depending on the temperature, hydrogen diffusion in metals appears to proceed through different mechanisms [69]. While all of the statements below may not apply to YH_2, several of these phenomena are known to occur in YH_2 and the fact that several different mechanisms occur for hydrogen diffusion in metals means that a classical interpretation of hydrogen in YH_2 may not be correct. The various mechanisms by which hydrogen may diffuse in metals are briefly summarized here.

I. At low temperatures, where hydrogen is self-trapped, hydrogen atoms are believed to migrate by coherent tunneling in a zero-phonon process.

II. This is gradually damped with increasing temperature through interactions with conduction electrons and diphonon processes, which results in incoherent hopping of hydrogen.

III. As the temperature further increases, migration processes involving many phonons may occur. This can occur non-adiabatically if tunneling is less favorable and adiabatically if tunneling is more favorable.

IV. At still higher temperatures, hydrogen atoms diffuse by classical Fick diffusion. That is, the hydrogen behaves as a classical particle and diffuses through thermal excitation.

V. At very high temperatures, but before the hydride decomposes, the hydrogen atoms are no longer bound to their interstitial sites and undergo free motion.

The overall temperature dependence of hydrogen in metals is shown in Figure 5-9.

Given the different mechanisms described above, it is clear that a classical model, such as Fick's First Law of Diffusion, may not sufficiently describe hydrogen diffusion in metal hydrides. However, several studies assuming a classical model for diffusion have been carried out in the past. Table 5-4 summarizes key hydrogen diffusion data, including activation energy (E_A) and pre-exponential

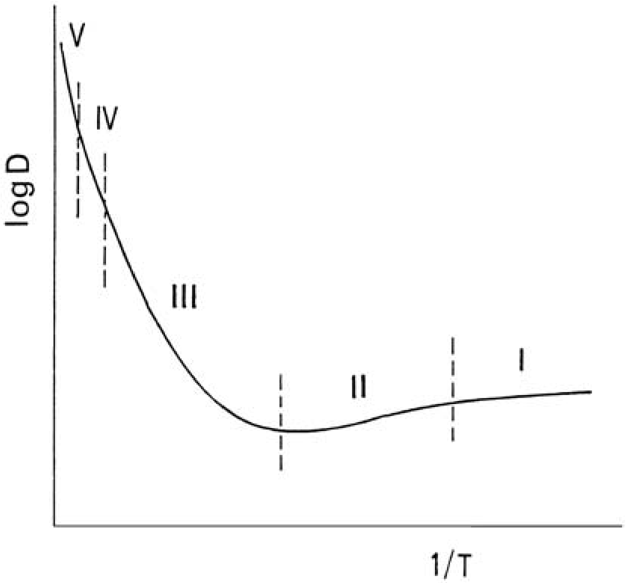

Figure 5-9: Schematic of the expected temperature dependence of the diffusion coefficient of hydrogen in metals. Temperature regions (I) - (V) are classified according to the dominant diffusion mechanism (see section 5.8.2). Note that not all of these temperature regimes may be realized in real systems. Figure and caption from [69].

factor (D_0), for yttrium hydrides as a function of hydrogen content. For stoichiometries where pre-exponential factors were not available in the literature, they were approximated using the Einstein equation for diffusion:

$$D = \frac{1}{6} z f \nu_0 \lambda^2 \exp\left(-\frac{E_A}{k_B T}\right) \tag{30}$$

where z is the number of nearest-neighbor diffusion sites (six for T-T jumps), ν_0 is the hydrogen atom jump attempt frequency, λ is the distance to the nearest neighbor site (half the lattice parameter for T-T jumps), and f is a correction factor of approximately 0.74 [112]. Note that this analysis does not account for hydrogen concentration factors, which would change the diffusion coefficient. This analysis also does not account for hydrogen jumps other than T-T jumps. As noted above, some studies have hypothesized that T-T jumps are the dominant migration mechanism, while others suggest it is not the dominant migration mechanism.

Because the studies cited here have these shortcomings, more diffusion studies of hydrogen in YH_2 are required to understand the mechanisms of hydrogen diffusion and the temperature regimes where mechanisms may change. This also includes studies of YH_3 to understand the impact of site occupancies, as the octahedral and tetrahedral sites are occupied in the trihydride, which may enable further distinction of the diffusion mechanism and jump sites involved in the diffusion processes.

Table 5-4: Available diffusion parameters for the Y-H system. D_0 values were calculated as described in Equation (30) when not provided in the reference.

Hydrogen content (H/Y)	E_A (eV)	D_0 ($\mathrm{cm^2\,s^{-1}}$)	Ref. (-)
1.63	1.1	5.3×10^{-1}	[29]
1.80	0.3	N/A	[34]
1.87	1.73	45.7	[35]
1.91	0.53	4.8×10^{-4}	[111]
1.92	0.438	7.9×10^{-5}	[29]
1.95	0.4	9.0×10^{-5}	[111]
1.98	0.417	7.9×10^{-5}	[29]
2.03	0.38	1.0×10^{-4}	[111]

5.9 Out-of-pile degradation of yttrium dihydride

This section represents a significant gap in our current knowledge regarding YH_2 performance as a moderator. It is currently hypothesized that the material will degrade under the thermal cycling that will occur during startup/shutdown cycles for a nuclear reactor. Phase stability will be affected by significant temperature changes under hydrogen partial pressures such that YH_3 may be stable at low temperature, which could result in the degradation of thermophysical and mechanical properties, as well as pulverization of the moderator. Fast temperature changes could result in thermal shock of the moderator. Additionally, operation of the moderator at high temperatures (e.g., above 750 K) could allow for hydrogen loss through a moderator cladding, reactor monolith, or pressure vessel. However, the relevant testing parameters have not been critically evaluated. As such, thermo-mechanical testing for this type of behavior has yet to occur.

In general, it was established early on that metal hydride moderators would undergo hydrogen losses due to temperature and hydrogen redistribution under temperature gradients, as observed in the ANP and SNAP programs [9, 11, 113, 114]. To mitigate hydrogen losses, a permeation-resistant cladding is necessary. Historic concepts focused on FeCrAl alloys with native aluminum oxide layers [113] and ceramic coatings to the cladding inner diameter of Hastelloy-N [9] in the ANP and SNAP programs, respectively.

In the event of a reactor breach, a potential ingress of air will enable degradation of the moderator through reactions with nitrogen and oxygen. The ability of yttrium compounds to readily react with oxygen is well-documented in the literature, as yttrium is found at the bottom of the Ellingham diagrams for oxide formation [115]. However, YH_2 has also been observed to react at room temperature with nitrogen to form surface layers of yttrium nitride. Nitrogen rot of YH_2 has also been observed in the past, though no details of this phenomenon have been provided in the literature other than the fact that it may be impeded by grinding off the surface oxide/nitride and re-oxidizing the surface [11].

A recent examination of YH_2 oxidation in synthetic air by Kane et al. showed that YH_2 oxidized more slowly than yttrium metal [52]. The authors attributed the difference to proton migration from the hydride into the oxide scale, thus inhibiting oxygen diffusion from the oxide/air interface to the oxide/hydride interface. It was noted that the presence of yttrium fluoride (YF_3) and yttrium oxy-fluoride (YOF) impurities in the base metal carried over to the hydride phase and increased the oxidation rate, but this effect was reduced in the hydride as compared to yttrium metal.

Properties of unirradiated yttrium dihydride

Hu et al. performed thermal desorption experiments of YH_2[101]. The authors found that the hydrogen desorption process occurred in four distinct regimes characterized by (1) minimal hydrogen loss followed by (2) linear hydrogen loss with temperature and (3) constant hydrogen loss with temperature. In the final regime, (4) hydrogen loss increased rapidly with temperature.

6 Properties of unirradiated zirconium hydride

6.1 Zr-H system

The Zr-H system consists of four stable phases and has been reviewed several times in the literature [53, 116–118]. Wang et al. [53] provided thermodynamic expressions defining the phase boundaries and a compilation of experimental data used to confirm those expressions. The α-Zr phase, space group $P6_3/mmc$, consists of H in the hexagonal close packed (hcp) Zr metal lattice. Hydrogen dissolved in the α-Zr lattice occupies interstitial sites, and has been shown to prefer the tetrahedral versus octahedral interstitial site [119–121]. Lattice parameter increases linearly with hydrogen concentration in the α-phase [122]. The β-Zr phase, space group $Im\bar{3}m$, is a body-centered cubic (bcc) high temperature structure. Hydrogen dissolved in β-Zr occupies interstitial sites, but the interstitial location has not been precisely determined. The δ phase, space group $Fm\bar{3}m$, is a face-centered cubic (fcc) fluorite crystal structure with H atoms located at the tetrahedral interstitial sites [123, 124]. The ε phase, space group $\mathrm{I}4/mmm$, is a distorted fluorite face-centered tetragonal (fct) structure with the H located at the tetrahedral interstitial sites [123–125]. The tetragonality of the cell increases with increasing H concentration [126]. Two metastable phases have been identified, γ phase [123] and ζ phase [119, 127]. The γ phase, space group $P4_2/n$, has been identified as fct crystal structure, with H located at tetrahedral interstitial sites on alternate (110) planes, leading to an occupancy of $\sim$ 50 at.% H.

Diagrams showing the crystal structures and interstitial sites in the α- and δ-phases of these systems are provided in Figure 6-1. Hydrogen mostly occupies tetrahedral interstices in the α-phase and mostly tetrahedral interstices in the δ-phase in the Zr-H system. Octahedral site occupation is possible especially at elevated temperature and high hydrogen concentration. The number of interstitial sites occupied will increase with H/M. Atomic percent can be converted to H/M ratio using Equation (31) and H/M or x can be converted to concentration in atomic percent using Equation (32)

$$\frac{\mathrm{H}}{\mathrm{M}} = x = \frac{C\ [\text{at.\%}]}{100\left(1 - \dfrac{C\ [\text{at.\%}]}{100}\right)}. \tag{31}$$

$$C\ [\text{at.\%}] = \frac{x}{1+x} \times 100. \tag{32}$$

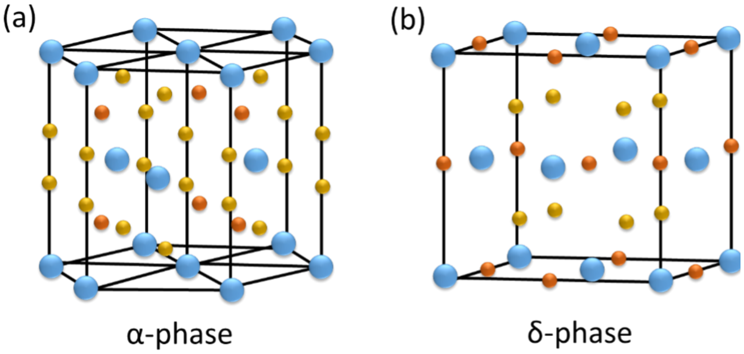

Figure 6-1: Diagrams showing the available interstitial sites in the (a) α-phase (hcp) and (b) δ-phase (fcc) hydride structures. Metal atom locations are shown as large blue spheres, tetrahedral interstitial sites are shown as small yellow spheres, and octahedral interstitial sites are shown as small orange spheres.

6.2 Thermodynamics and phase equilibrium

Phase diagrams provide equilibrium crystallographic information as a function of temperature and atomic composition. Phase boundaries are theorized using thermodynamic calculations and validated with experimental measurements, and thus provide the best summary of known thermodynamic information for the particular metal-hydride system. In two-phase regions, where the microstructure is a composite of two primary phases, the lever rule can be used to determine the primary phase fraction expected at a particular temperature and stoichiometry. Because phase diagrams describe equilibrium conditions, rapid temperature changes can result in additional metastable phases in the microstructure. Phase diagrams are provided for the Zr-H system in Figure 6-2. Two phase diagrams are reproduced, the first produced using the composition-temperature relationships of the phase boundaries reported by Wang and Olander [53]; a second is constructed using Thermochimica calculations [128]. In general the agreement between the diagrams is good, the most clear exception being the overestimation of the extent of the δ+ε mixed-phase region by Thermochimica.

Phase diagrams display the equilibrium crystallographic phase for a specified temperature and composition where the pressure is normally assumed atmospheric. In hydrogen systems the composition is also a function of pressure; therefore, Pressure-Composition-Temperature (PCT) diagrams, or isotherms, are used to relate the temperature with equilibrium H_2 partial pressure to the stoichiometry. In general, as the temperature increases, the pressure required to contain hydrogen inside the system also increases. Higher temperatures induce lattice disorder and therefore make retaining hydrogen more difficult [117]. PCT diagrams can be directly correlated with phase diagrams. For a given temperature, the low pressure portion of the isotherm describes interstitial hydrogen entering the metal lattice [117]. As the pressure increases, the H/M, or hydrogen to metal ratio, increases. If a second hydride phase begins to form, the pressure remains constant at a given temperature, creating a plateau in the isotherm plot. In the two-phase regions, the equilibrium hydrogen pressure is a function of temperature only. Wang and Olander [53] provided an expression for this in the Zr-H system:

$$\ln\, P_{2\Phi}^{(i/j)} = a + \frac{\Delta \bar{H}^{(i/j)}}{RT} \tag{33}$$

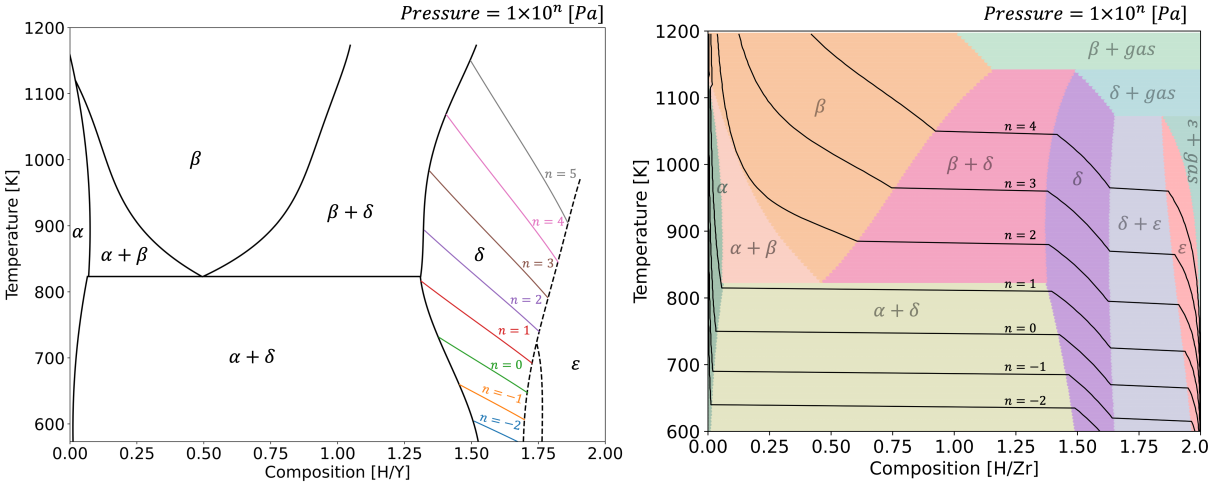

Figure 6-2: Zr–H phase diagrams. Left: phase boundaries from the composition–temperature relations of Wang and Olander [53]. Right: Thermochimica calculation [128]. Isobars of the equilibrium H_2 pressure are superimposed: in the left plot, δ-phase pressures are evaluated via eq. (37); in the right plot, pressures are calculated by Thermochimica.

In this expression, i and j are the coexisting phases and $\Delta\bar{H}^{(i/j)}$ is the corresponding relative partial molar enthalpy of hydrogen. In the two phase regions, a range of H/M values are possible in the same sample for a given temperature and pressure, as is also represented in a phase diagram for a given temperature. Depending on the stoichiometry, the equilibrium phase fraction can be calculated by applying the lever rule to the phase diagram at the temperature of interest. As the H/M ratio increases above the equilibrium two-phase region, the pressure again begins to increase. Additional two-phase regions existing at a specific temperature will be represented by additional plateau regions at higher H/M ratios

Raymond [129] fit a series of ZrH_x isochore hydrogen dissociation data collected in the δ and ε-phase regions with a curve that can be utilized to predict equilibrium pressures at higher temperatures. The curve is given in Equation (34),

$$\log(p_{\mathrm{eq}})\ [\mathrm{Pa}] = K_1 + \frac{K_2 \times 10^3}{T} \tag{34}$$

where,

$$K_1 = 1.164217 + 38.6433x - 34.2639x^2 + 9.2821x^3, \tag{35}$$

$$K_2 = -31.2982 + 23.5741x - 6.0280x^2, \tag{36}$$

T is the temperature in Kelvin, and x is the hydrogen-to-zirconium atom ratio.

Additionally, Wang and Olander [53] developed an expression for pressure as a function of composition and temperature in the Zr-H system. The expression is provided in Equation (37).

$$\ln(p_{\mathrm{eq}})\ [\mathrm{Pa}] = 2\ln\left(\frac{x}{2-x}\right) + 19.535 + 5.21x - \frac{2.07 \times 10^4}{T}. \tag{37}$$

Using these two expressions, we can predict that the equilibrium pressures required to maintain $\mathrm{ZrH}_{1.6}$ will reach the values presented in Table 6-1. The table demonstrates that maintaining $x = 1.6$ stoichiometry in ZrH_x requires equilibrium hydrogen pressures substantially greater than 1 atm once the moderator temperature surpasses 850 °C.

Table 6-1: Predicted equilibrium pressures required to maintain x = 1.6 stoichiometry in ZrH_x in excursion temperature regimes, comparing eq. (34) and eq. (37).

Temperature (°C)	Equilibrium H_2 Pressure (kPa)	
	eq. (34)	eq. (37)
800	79.5	85.4
850	188.0	201.4
900	413.1	441.9
950	851.3	909.0
1000	1657.4	1766.84

Figure 6-3 summarizes the available literature data on PCT relationships for the Zr-H system between 973-1273 K (700-1000 °C). No data is available for δ-phase ZrH_x above 1123 K, so Figure 6-3 uses Equation (37) to predict the δ-phase PCT curve at each temperature. There are discrepancies in the literature data in the δ-phase region, which makes predicting precise equilibrium pressures difficult. At 1073 K and $x = 1.6$, for example, hydrogen pressures vary from approximately 61 − 84 kPa. Equilibrium partial pressures at $x = 1.6$ range from 71 kPa at 1073 K to much greater than 100 kPa at 1173 K, where data is only available in the β-phase.

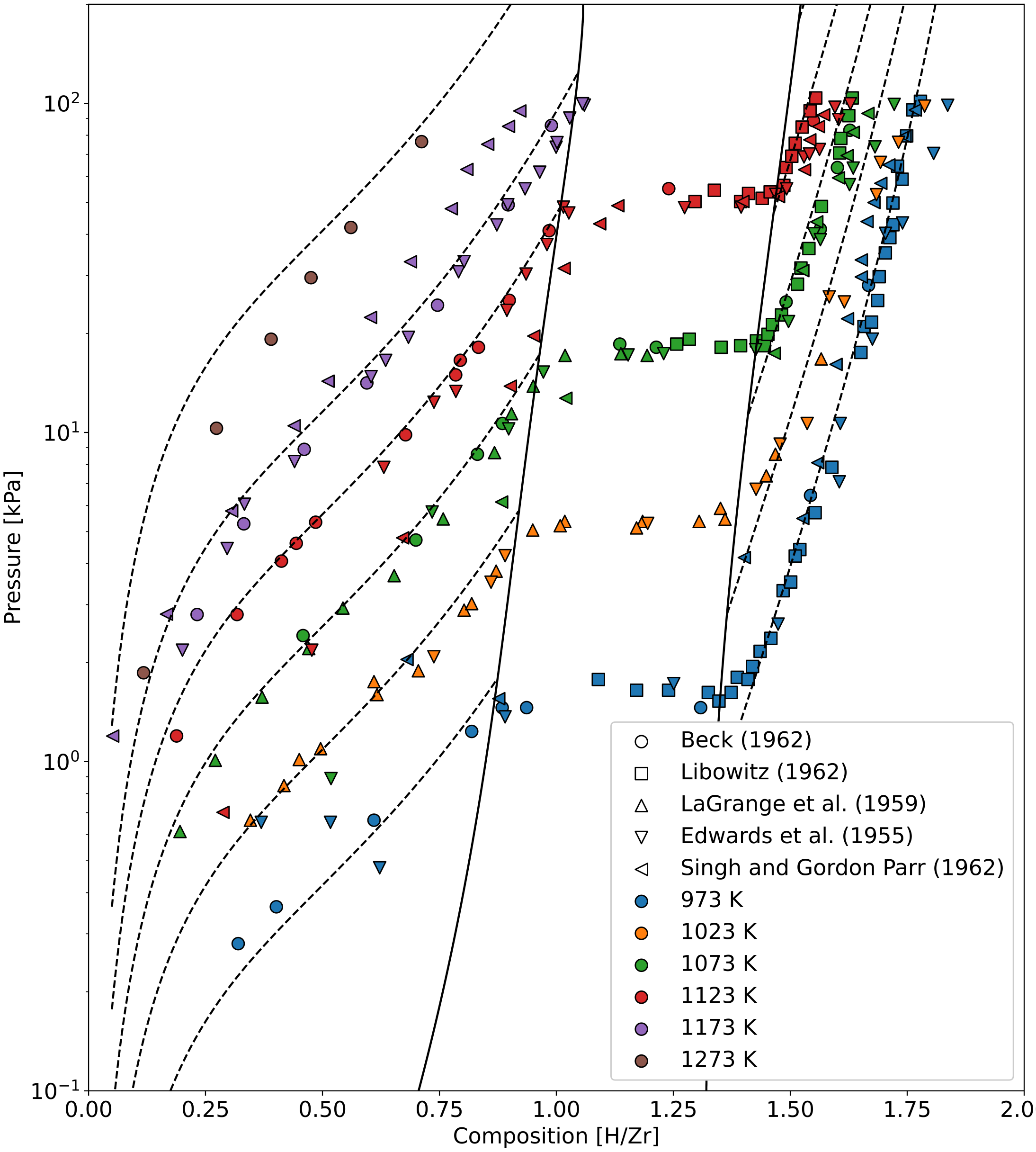

Figure 6-3: Compilation of available PCT data between 973 K and 1273 K for the Zr–H system [130–134]. The dashed and solid lines, representing isotherms and phase boundaries, respectively, are taken from Wang and Olander [53].

Properties of unirradiated zirconium hydride

6.3 Fabrication

Zirconium hydride fabrication is generally more difficult and alloy-specific than yttrium hydride fabrication due to the more complicated phase space. Each phase transformation induces a different amount of volume expansion as hydrogen is absorbed into the metal, which can cause cracking [135]. The transformation from α- zirconium to the δ- hydride at 773 K results in a volume change of approximately 20%. In contrast, the volume change arising during the transformation from the high temperature β-zirconium phase at 1073 K is <10%. High temperatures also allow for easier accommodation of stresses and deformation. Transforming from δ- to ϵ-phase zirconium hydride at 1073 K results in a 4% volume contraction. This transformation typically produces a band structure throughout the entire material which is believed to be twinning due to a martensitic-type transformation [135–137]. The band microstructure changes depending on the starting zirconium alloy and fabrication parameters. Similar to yttrium hydride, fabrication is typically performed by heating zirconium metal feedstock in a vacuum furnace and exposing the metal to hydrogen at temperature and pressure conditions described by the pressure-composition-temperature diagrams. In a Sievert's Apparatus type setup, hydrogen is slowly released into a reaction vessel and allowed to equilibrate at a particular temperature. Each aliquot slightly increases the partial pressure inside the reaction vessel, allowing the metal to equilibrate at a slightly higher H/Zr. The process continues until the final H/Zr is reached, at which point the sample is cooled rapidly to room temperature. This method helps to prevent cracking but takes longer, especially for larger components. In a flowing furnace setup, the sample is heated to high temperature in vacuum and hydrogen is continuously flowed over the sample at a particular partial pressure. The latter method is faster, but more difficult to control the absorption rate and therefore cracking. Both of these methods experience challenges with maintaining the desired H/Zr on cooling. Cooling in hydrogen can lead to surface enrichment, and cooling in vacuum can lead to hydrogen loss. The rate of enrichment or loss depends on the temperature, ramp rate, and surface reactions. Ideally, components are cooled along an isochore to maintain a specific H/Zr throughout the process. Recently, He et al. [138] developed a method for densifying zirconium hydride monoliths without hydrogen loss using high-pressure spark plasma sintering. Zirconium seems particularly susceptible to zirconium nitride formation, which forms as a gold-colored film on the surface, during hydriding. The zirconium nitride layer is well documented [139, 140] and slows hydriding kinetics. The hydriding reaction can cause segregation of alloying elements. For moderator applications, Zircaloy-4 is often selected as the feedstock alloy due to its low hafnium content. In Zircaloy-4, pre-existing $Zr(Fe,Cr)_2$ (Laves phase) precipitates dissociate during hydriding and Sn comes out of solution to form large precipitates with minor additions of Fe and Cr, often at grain boundaries [141].

6.4 Hydrogen migration in bulk zirconium hydrides

ZrH_x moderators are subject to appreciable temperature gradients. In such fields, hydrogen transport is not governed solely by concentration–driven Fickian diffusion; a thermodiffusion (Soret) contribution also arises, in which a temperature gradient drives a net hydrogen flux. In the absence of a stress gradient, the flux of hydrogen in bulk ZrH_x can be described using,

$$J_H = -D_H \nabla C_H - \frac{D_H C_H Q^*}{RT^2} \nabla T, \tag{38}$$

where D_H and C_H are the diffusivity and hydrogen concentration, respectively, R is the gas constant, and Q^* represents the heat of transport. The first and second terms in this equation represent the flux of hydrogen due to Fickian diffusion and the Soret effect, respectively. A positive Q^* drives hydrogen toward cooler regions

Most hydrogen diffusion measurements in ZrH_x (and YH_x) have been performed by nuclear magnetic resonance (NMR) methods. The measurements were taken using one of the three methods, namely, pulse field gradient, spin-lattice relaxation (T_1), or spin-spin relaxation (T_2). Pulse field gradient use the application of a magnetic field gradient during the NMR experiment, which allows direct measurement of the diffusion constant. Measurement of either T_1 or T_2 relaxation provides an indirect determination of diffusion coefficient by revealing the activation energy or enthalpy, respectively. In the case of the T_2 relaxation measurement, this is a more qualitative measurement of the mobility rather than a quantitative one. It should be noted that Phua et al. [142] performed an NMR diffusion study on YH_x samples containing various impurity concentrations and found that paramagnetic impurities (e.g. as low as 50 ppm Gd) can influence the measured diffusion properties. However, paramagnetic impurities have been shown to affect the relaxation rate by electron-nuclear coupling. The electronic contribution to the T_1 relaxation is temperature independent when there is an absence of paramagnetic species, however, when they are introduced, the electronic contribution becomes temperature dependent. In the study by Phua et al. [142], the effect of hydrogen diffusion and electron-nuclear coupling were not separated and it is therefore not possible to determine if the change in apparent diffusion was purely due to the diffusion process.

In ZrH_x, diffusion is believed to occur primarily by jumps between adjacent tetrahedral interstitial sites in the FCC structure (T-T diffusion). Sharp increases in the activation energy for diffusion, E_a, were observed as x approaches 2 by several authors [143–146]. This has been attributed to two possible factors. Hydrogen is most often believed to jump to octahedral interstitial sites at higher temperatures when $x \geq 1.9$. Bowman et al. [143] suggest that because tetrahedral sites are mostly full at high x, E_a becomes dependent on the vacancy formation energy, E_f, at high compositions. Instead of $E_a = E_m$, $E_a = E_m + E_f$, increasing the activation energy. They estimated $E_f \sim 0.7$ eV. Wipf et al. [147] measured E_a at low temperatures and found that, when they extrapolated their data to higher temperature, it did not align with the NMR results collected by other authors at higher temperatures. This suggests that different diffusion mechanisms occur at high and low temperatures and potentially confirms the theory of hydrogen jumping to octahedral sites at high temperatures.

Table 6-2 provides diffusion parameters for ZrH_x ($x \sim 1.6$), where $D_H\,[\mathrm{m}^2/\mathrm{s}] = D_0 \exp\left(\frac{E_a}{kT}\right)$. The proton T_1 relaxation NMR studies do not provide D_0, so D_0 was estimated using the equation $D_0 = 16zf\lambda^2\omega_0$, where z is the number of nearest neighbor sites (6 for δ-phase), f is a correlation factor, estimated to be 0.74 [148] assuming primarily T-T diffusion, and $\lambda = 0.5a$, where a is the lattice parameter. The ω_0 term is the pre-factor to the jump frequency, which is measured by NMR along with E_a. The diffusion coefficients were utilized to calculate the characteristic hydrogen diffusion length, using the equation $L = \sqrt{Dt}$, and are shown as a function of time in Figure 6-4.

In the most recent measurement listed in Table 6-2, that performed by Majer et al. [146], it was demonstrated that hydrogen diffusivity increases as the H/Zr ratio decreases, which is consistent with a vacancy-mediated transport mechanism. Following the approach of Terrani et al. [149], the Arrhenius relationship obtained by Majer at an H/Zr ratio of 1.58 can be extrapolated across stoichiometries by modifying the pre-exponential factor based on the probability that a neighboring tetrahedral site is unoccupied by another hydrogen atom. This probability is determined by the stoichiometry and structure of the system, resulting in an expression for hydrogen diffusivity in

Table 6-2: Diffusion of hydrogen in Zr-H, measured at a composition close to $ZrH_{1.6}$. D_0 values were calculated as described in the text when not provided in the reference.

x	D_0 (m^2s^{-1})	E_a (eV)	Author(s)
1.50-1.70	2.50×10^{-5}	0.772	Paetz and Lücke [153]
1.56-1.86	5.99×10^{-2}	1.509	Albrecht and Goode [154]
1.58	1.53×10^{-7}	0.612	Majer et al. [146]
1.58	2.46×10^{-7}	0.57	Han et al. [144]
1.58	2.91×10^{-7}	0.58	Han et al. [144]
1.58	1.10×10^{-7}	0.55	Han et al. [144]
1.6	1.30×10^{-6}	0.550	Harkness and Young [155]
1.60	3.56×10^{-8}	0.50	Bowman and Craft [143]
1.60	1.09×10^{-7}	0.49	Gulbransen and Andrew [156]
1.60	-	0.49	Wipf et al. [147]
1.629	4.19×10^{-7}	0.58	Korn and Goren [157]

δ-ZrH_x as

$$D_H\left[\mathrm{m}^2/\mathrm{s}\right] = 7.29 \times 10^{-7}\left(1 - \frac{x}{2}\right)\exp\left(\frac{-0.612}{k_B T}\right), \tag{39}$$

where x is the H/Zr ratio. This equation is applicable for compositions ranging from approximately $x = 1.5$ to $x = 1.7$. As x approaches 2, Majer noted that a small fraction of hydrogen atoms located on interstitial sites contribute significantly to the measured diffusivity.

The heat of transport (Q^*) describes the strength of the Soret effect, the second term in Equation (38). The most frequently used value for Q^* originates from measurements by Sommer and Dennison, $Q^* = 5.44$ kJ/mol [150]. Previous reviews [151] of ZrH_x properties identified this as the only measurement in the literature, however another study exists, that of Merten et al. [152], which found no measurable hydrogen redistribution when $ZrH_{1.6}$ was subjected to a temperature gradient, attributing Sommer and Dennsion's result to interaction of the sample with the gas phase. This finding implies that Q^* is likely much lower than previously assumed. This is not to say that non-isothermal operation and low Q^* means insignificant temperature-driven hydrogen migration as hydrogen can redistribute via the gas phase. In accordance with the PCT relations (see Figure 6-3), the equilibrium H_2 pressure above ZrH_x is strongly temperature dependent: higher over hotter regions and markedly lower over cooler ones. As a result, hot areas desorb hydrogen (higher p_{eq}), while cooler surfaces take it up, driving a net transfer of hydrogen through the intervening gas. The kinetics of hydrogen desorption are necessary to predict the rate of this process, and are summarized in the succeeding section.

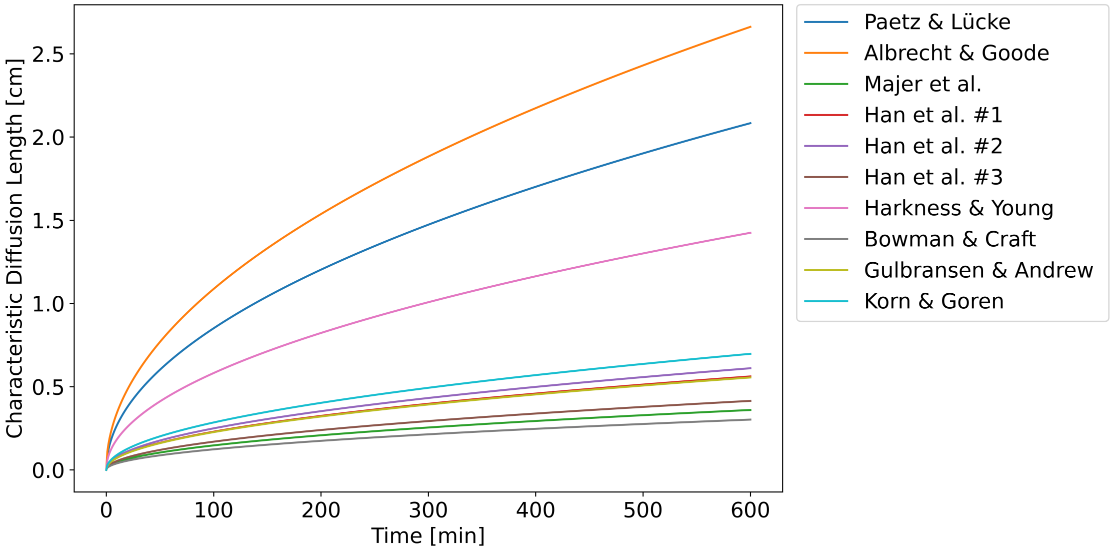

Figure 6-4: Characteristic diffusion lengths, $\sqrt{Dt}$, for hydrogen in ZrH$_{1.6}$ at 1173 K [143, 144, 146, 153–157]. Diffusion parameters used to calculate the plot are provided in Table 6-2.

6.5 Hydrogen release in zirconium hydrides

The moderator is thermally stable until a temperature or pressure regime is reached where the hydrogen begins to release from the material, referred to as hydrogen desorption or a de-hydride reaction. To predict hydrogen desorption kinetics in a temperature excursion environment, the H_2 partial pressure and stoichiometry should be measured as a function of time at several temperatures. The length of time required to reach pressure equilibrium should be determined at each temperature to quantify desorption reaction kinetics. Most thermal desorption studies performed on ZrH_x apply dynamic vacuum to continuously pump H_2 out of the analysis chamber [158–161]. Depending on hydrogen diffusion kinetics, desorption in vacuum could result in phase transformations. Additionally, the time to reach pressure equilibrium within the δ-phase cannot be measured with this method. Terrani et al. [162] measured hydrogen pressure build-up as a result of de-hydriding ZrH_x in a closed vessel. 1 mm thick hydride disks were heated to various temperatures and held at temperature until pressure equilibrium was reached. Equilibrium conditions were reached in a matter of minutes at each temperature studied. This measurement conflates stoichiometry and pressure but is more representative of a reactor environment.

Experimental investigations into the desorption of hydrogen from δ-ZrH_x have demonstrated that a zero-order kinetic model best describes the process [159, 162]. This observation indicates that the recombination of atomic hydrogen into molecular hydrogen at the surface is the rate-determining step in the desorption process. As such, the flux of hydrogen, per unit area, between the surface and environment can be approximated using:

$$J_H = K(p_{\text{eq}} - p), \tag{40}$$

where p is the pressure, p_{eq} is the equilibrium pressure, and K is a reaction constant.

Measurements of the desorption rate constant, defined as $k_{\text{des}} = Kp_{\text{eq}}$, have been reported by multiple authors [159, 160, 162, 163] and are plotted in Figure 6-5. Our independent recalculation of the data published by Terrani et al. [162], enabled by their detailed reporting of hydrogen pressure

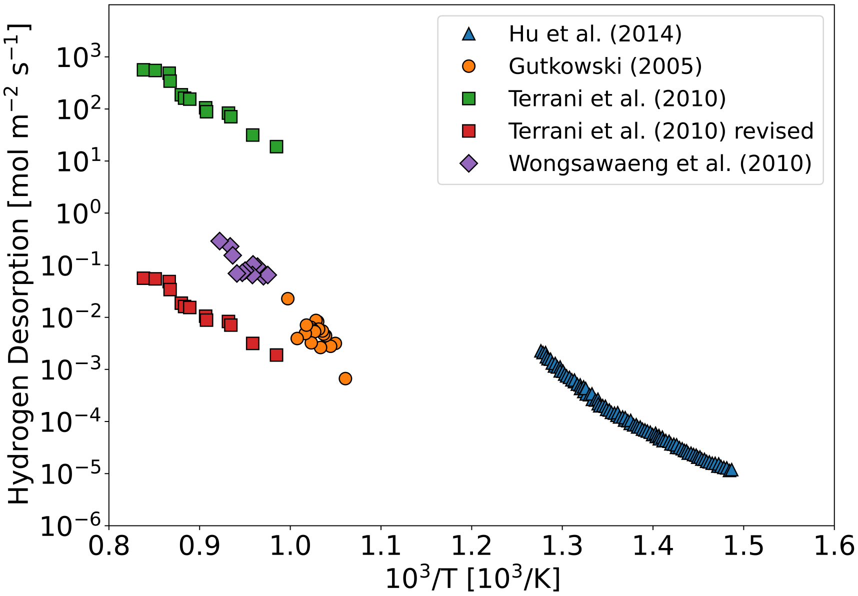

Figure 6-5: Experimental measurements of hydrogen desorption kinetics [159, 160, 162, 163] in ZrH_x. Note that the Gutwowski measurement was taken from Ref. [151], Terrani et al.'s measurements have been adjusted based on recalculations described in the text, and Hu et al.'s data was gathered by correcting the inconsistent x axis in the original publication.

evolution in closed vessels, indicates that the final values originally reported are approximately four orders of magnitude too high. The adjusted values, shown in Figure 6-5, align more closely with other experimental measurements at comparable temperatures. Nonetheless, Figure 6-5 highlights persistent discrepancies among reported desorption rates. Although the adjusted Terrani et al. values may provide the most reactor-relevant representation.

6.6 Thermophysical Properties

6.6.1 Heat Capacity

Heat capacity refers to the amount of heat required to produce a temperature change in a mass of material. Heat capacity measurements have been performed in ZrH_x and are shown in Figure 6-6. At room temperature, the heat capacity is similar to the base metal heat capacities. This is due to contribution primarily from the acoustic modes of lattice vibration at room temperature. Hydrogen vibration, which is considered an optical mode, markedly increases the heat capacity as temperature increases [164]. For this reason the heat capacities of the base metals remain mostly constant in the temperature ranges shown in Figure 6-6, while the hydride heat capacities increase continuously with temperature. Figure 6-6 shows little dependence of the heat capacity on the specific ZrH_x composition within the δ-phase phase.

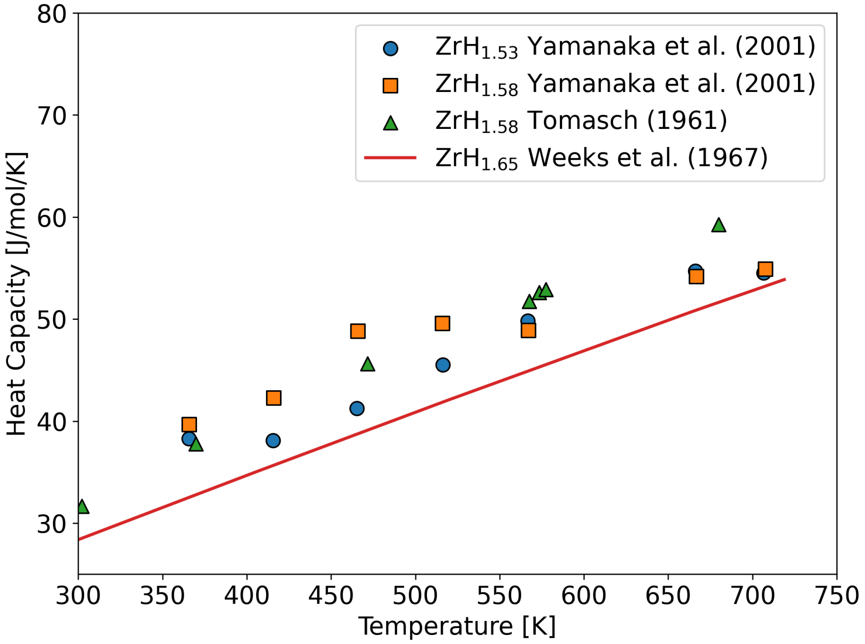

Figure 6-6: Heat capacity data for δ-phase ZrH$_x$, collected by Yamanaka et al. [164], Tomasch [165], and Weeks et al. [166]. The different compositions (H/M) used for these studies are provided in the legends.

6.6.2 Thermal Diffusivity

Thermal diffusivity refers to the transfer rate of heat from the hot end to the cold end of a material. Available literature data are shown for ZrH_x in Figure 6-7. Diffusivity measurements cannot be collected above 600-700 K in ZrH_x due to hydrogen release occurring. Near 300 K, the thermal diffusivity of $ZrH_{1.9}$ is around 0.17 cm^2/s, while the thermal diffusivity of $YH_{1.9}$ is approximately 0.47 cm^2/s. At higher temperatures the thermal diffusivity of $YH_{1.9}$ is closer to $ZrH_{1.9}$. At 600 K the thermal diffusivity of $ZrH_{1.9}$ is approximately 0.095 cm^2/s and the thermal diffusivity of $YH_{1.9}$ is approximately 0.14 cm^2/s. Figure 6-8 shows how thermal diffusivity increases with x in ZrH_x. The thermal diffusivity curve begins to increase with increasing hydrogen content just above the transition from δ-phase to ε-phase zirconium hydride, which occurs at approximately $x = 1.69$. Thermal diffusivity in δ-phase zirconium hydride remains constant with increasing hydrogen content, while thermal diffusivity in ε-phase increases with hydrogen content.

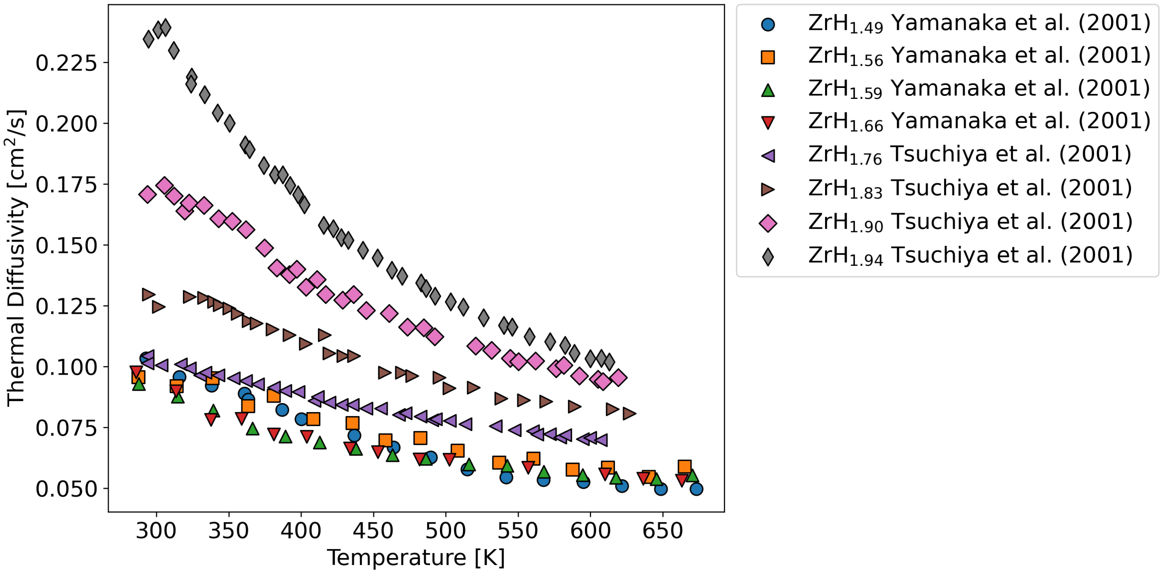

Figure 6-7: Literature data showing thermal diffusivity as a function of temperature for various hydride compositions in ZrH$_x$. ZrH$_x$ samples with $x > 1.69$ were in δ-phase and samples with $x > 1.69$ were in ε-phase. Data was collected by Yamanaka et al. [164] and Tsuchiya et al. [167].

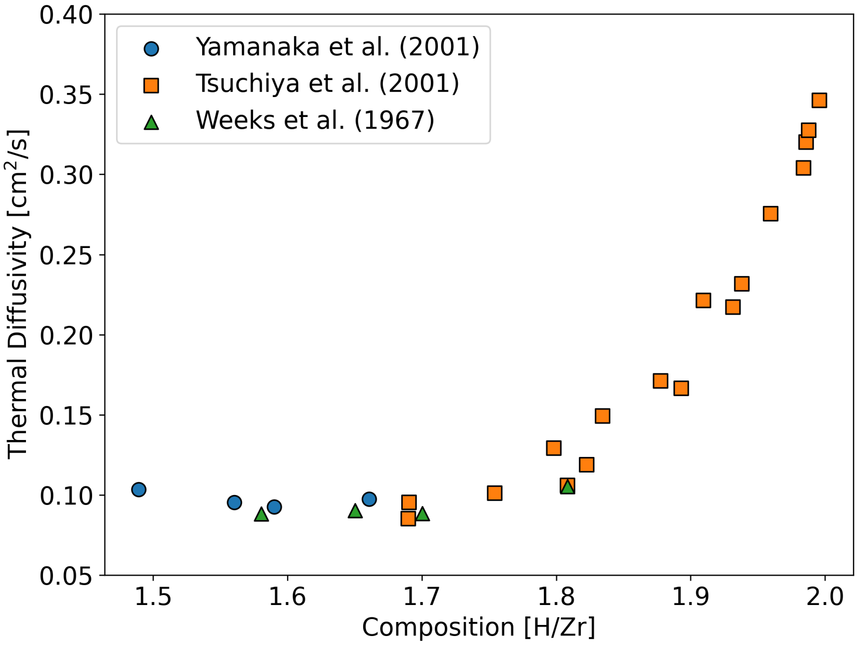

Figure 6-8: Literature data from Yamanaka et al. [164], Weeks et al. [166], and Tsuchiya et al. [167] showing thermal diffusivity at room temperature as a function of ZrH$_x$ composition.

6.6.3 Thermal Conductivity

Thermal conductivity, k, can be calculated from the thermal diffusivity using Equation (41), where δ is the thermal diffusivity, C_p is the heat capacity, and ρ is the density.

$$k = \delta C_p \rho. \tag{41}$$

Figure 6-9 shows that thermal conductivity increases with hydrogen content in ZrH_x. At lower temperatures, the thermal conductivity of $YH_{1.9}$ is higher than $ZrH_{1.9}$. At 300 K, the thermal conductivity is approximately 0.45 $Wcm^{-1}K^{-1}$ in $ZrH_{1.9}$ and 0.77 $Wcm^{-1}K^{-1}$ in $YH_{1.9}$. Following the same trend as thermal diffusivity, the thermal conductivities of $YH_{1.9}$ and $ZrH_{1.9}$ become more similar at higher temperatures. At 600 K, the thermal conductivity is approximately 0.35 $Wcm^{-1}K^{-1}$ in $ZrH_{1.9}$ and 0.45 $Wcm^{-1}K^{-1}$ in $YH_{1.9}$.

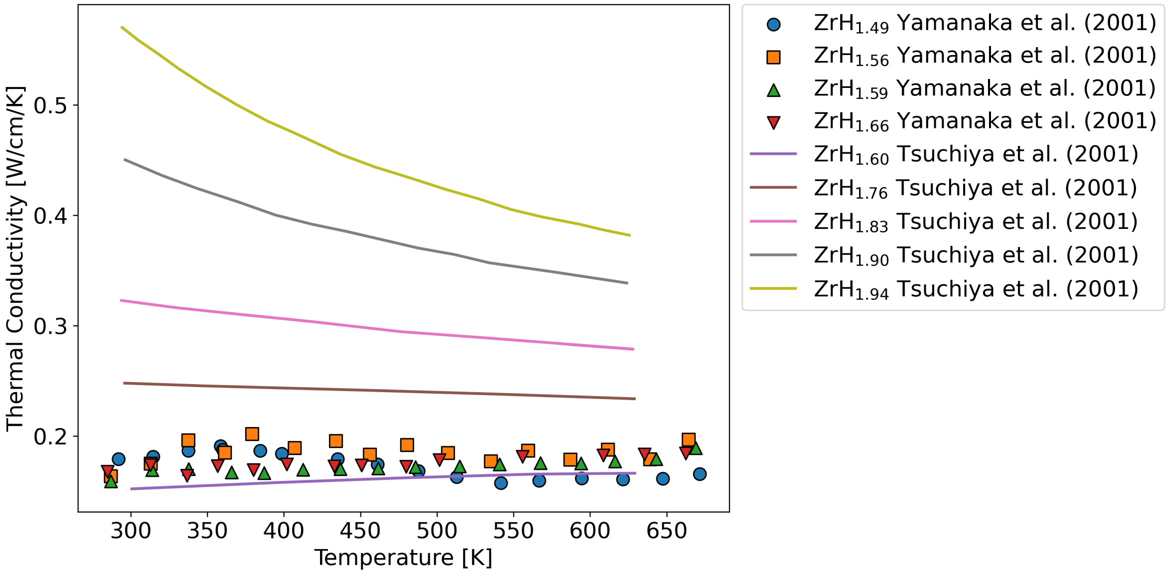

Figure 6-9: Literature data showing thermal conductivity as a function of temperature for various hydride compositions in ZrH_x. Data was collected by Yamanaka et al. [164] and Tsuchiya et al. [167] (note that Tsuchiya et al. did not measure heat capacity and sourced from literature).

6.7 Mechanical Properties

The mechanical and elastic properties of the δ- and ε-ZrH_x, have been extensively studied. Yamanaka et al. [168] employed pulse-echo ultrasound to obtain a comprehensive dataset of elastic properties for the δ-phase. They report a Young's modulus of approximately 130 GPa, which was observed to decrease slightly with increasing H/Zr ratio. Alongside modulus measurements, they also reported Poisson's ratio and microhardness values, providing a comprehensive dataset for this phase. Puls et al. [169] conducted compression and hardness tests on multiple ZrH_x compositions. Their results showed a significant drop in both Young's modulus and yield strength within the H/Zr range of 1.6–1.8, coinciding with the transition from the δ to the ε phase. Lanin et al. [170] determined the Young's modulus of ε-$ZrH_{1.85}$ to be 67.7 GPa using tensile mechanical testing. Torres et al. [27] applied resonant ultrasound spectroscopy (RUS) to ε-$ZrH_{1.81}$, reporting a modulus of approximately 64 GPa. Their work represented the first experimental determination of the adiabatic

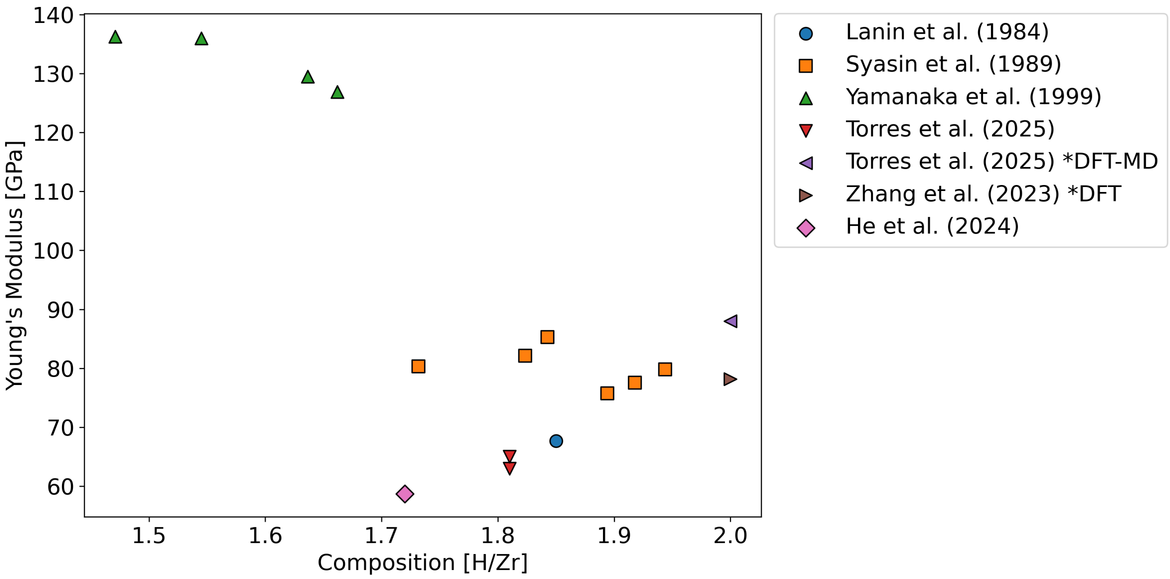

Figure 6-10: Literature data showing direct measurements of Young's modulus in ZrH$_x$ [27, 138, 168, 170, 171] and theoretical calculations of ZrH$_2$ [27, 185].

elastic constants of bulk ε-hydride. Non-monotonic changes in the Young's modulus of ZrH$_x$ were observed by Syasin et al. [171] over the range $1.7 < x < 1.95$. Processing routes also play a role: He et al. [138] measure a lower Young's modulus for high-pressure spark plasma sintered ε-ZrH$_{1.72}$.

Nanoindentation studies have also been widely used to study the mechanical properties of these hydrides. Cinbiz et al. [172] investigated δ-ZrH$_{1.61}$ and ε-ZrH$_{1.79}$, demonstrating that both the elastic modulus and indentation hardness decrease with increasing temperature and increasing hydrogen content (for these two compositions, at least). Xu and Shi [173] reported a reduced Young's modulus of 60–71 GPa for ε-ZrH$_{1.83}$ from nanoindentation measurements. Kuroda et al. [174] conducted both nanoindentation and Vickers hardness tests, also showing that hardness slightly decreases with increasing hydrogen content. According to nanoindentation studies by Oono et al. [175, 176], the ε-phase exhibits lower hardness than the δ-phase, and irradiation leads to a hardness increase in both phases.

Additional work has focused on hydrides in Zircaloy and Zirlo, particularly in the form of rims, blisters, and platelets [177–184].

Figure 6-10 presents Young's modulus as a function of hydrogen-to-metal ratio using values compiled from the literature, restricted to studies that directly measured the modulus. As shown, reported values for the ε-phase are scattered between 50 and 90 GPa. Torres et al. [27] speculated on the origin of this variability. This included the potential influence of microcracking, differences in experimental methodology, and deviations from the assumptions of a homogeneous isotropic continuum. In particular, when grain size is large or grains exhibit preferred orientation, the elastic response would become direction-dependent due to microstructural anisotropy.

Figure 6-11 shows hardness as a function of hydrogen-to-metal ratio, based on values compiled from the literature. To ensure comparability, the dataset is restricted to nanoindentation measurements performed on bulk material. Other approaches, such as Vickers hardness testing, are not directly comparable, while extensive studies on hydride rims, blisters, and platelets generally exhibit much greater variability.

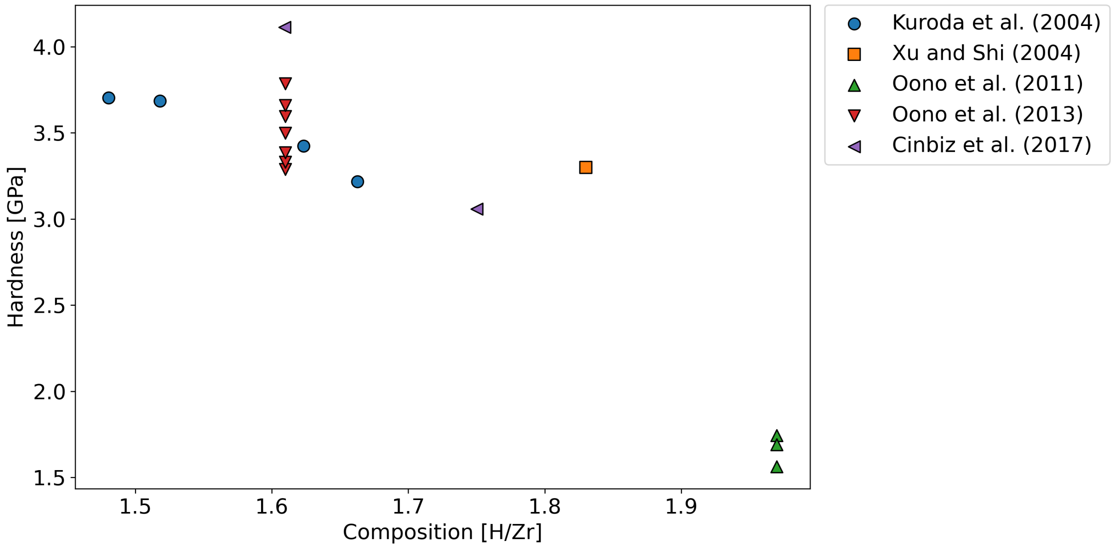

Figure 6-11: Literature data showing hardness as a function of composition in ZrH_x, collected for experiments on bulk zirconium hydride measured with nanoindentation [172–176].

Table 6-3: Yield stresses reported in literature for δ-zirconium hydride at approx. room temperature.

Author(s)	Methods	Yield Stress (MPa)
Cherubin et al. [177]	nanoindentation/model	862-904
Cherubin et al. [178]	micropillar compression	1084
Wang et al. [179]	nanoindenatiuon/model	800
Rico et al. [184]	nanoindenation/model	710
Puls et al. [169]	compression	630–990
Weekes et al. [186]	micropillar compression	900-1600
Chan et al. [187]	microcantilever	1160-1390

Properties of unirradiated zirconium hydride

As summarized in Table 6-3, literature values for the yield stress of δ-zirconium hydride at approximately room temperature show noticeable variation. Cherubin et al. [178] suggested that this scatter arises from two primary factors: differences in the source material or synthesis method, which can affect grain size and flaw populations within the hydride, and the specific experimental technique employed to obtain the measurement. Measurements using nanoindentation methods and a analytical models appear in fairly good agreement. Furthermore, experimental data [177, 179] indicate that the yield stress decreases approximately linearly with temperature in the range from room temperature to 300 °C.

7 Neutronic considerations

The figures of merit for the neutronic performance of moderators are the moderating power and the moderating ratio [188]. The moderating power is defined as the logarithmic energy decrement per collision (also called lethargy), ξ, multiplied by the macroscopic neutron scattering cross section, Σ_S. The moderating ratio is defined as the ratio of the moderating power to the macroscopic neutron absorption cross section, Σ_A. Both parameters are necessary for moderator qualification, as the former describes the efficiency with which neutrons are slowed down, while the latter describes the ability to moderate with minimal neutron absorption. It should be noted that materials with very high moderating power may have low moderating ratios due to high absorption cross sections. For example, gadolinium dihydride, $\mathrm{GdH_2}$, has a very high hydrogen density at room temperature (7.43×10^{22} atoms cm^{-3} [57]), but a very low moderating ratio because it also has a very high neutron absorption cross section: isotopically average cross section of approximately 49,000 barns [5]. Conversely, some materials may have a very low moderating power but a very high moderating ratio. For example, beryllium metal, Be, has a very low moderating power because it is relatively massive for a moderator material, but has a very high moderating ratio because it has a very low neutron absorption cross section.

7.1 Moderating power

Neutron lethargy Neutron lethargy is defined as the average effectiveness of a substance in slowing down neutrons for all collisions based on an assumption of equal probability for all collision angles between 0° and 180° [188]. For a neutron colliding with a nucleus of element i, with mass A_i, the equation for the lethargy is:

$$\xi_i = 1 + \frac{(A_i - 1)^2}{2A_i} \ln \frac{A_i - 1}{A_i + 1} \tag{42}$$

For example, the lethargy for beryllium is:

$$\xi_{\mathrm{Be}} = 1 + \frac{(9-1)^2}{2 \times 9} \ln \frac{9-1}{9+1} \approx 0.207$$

Equation (42) may be approximated as

$$\xi_i = \frac{2}{A_i + 2/3} \tag{43}$$

The approximation in Equation (43) is good for values of A_i greater than 10, but still quite accurate for small values of A_i. For $A = 1$ (H-1 nucleus), $\xi = 1$. Lethargy may also be used to calculate the average number of collisions required to slow down a neutron from one energy to another, $\bar{n}$, which is defined as:

$$\bar{n} = \frac{\ln\left(E_0/E\right)}{\xi} \tag{44}$$

For example, the average number of collisions required to thermalize 1 MeV neutrons using beryllium would be:

$$\bar{n}_{\mathrm{Be}} = \frac{\ln\left(E_0/E_{th}\right)}{\xi_{\mathrm{Be}}} = \frac{\ln\left[\frac{1\times10^6\mathrm{eV}}{0.025\mathrm{eV}}\right]}{0.207} = 84.7$$

Neutronic considerations

Table 7-1: Lethargy and average number of collisions required to thermalize 1 MeV neutrons for various nuclei of interest for nuclear reactor moderator applications.

Nucleus	Mass number	ξ	$\bar{n}$ to thermalize a 1-MeV neutron
${}^{1}_{1}\mathrm{H}$	1	1.000	17
${}^{2}_{1}\mathrm{H}$	2	0.725	24
${}^{4}_{2}\mathrm{He}$	4	0.425	41
${}^{9}_{4}\mathrm{Be}$	9	0.207	85
${}^{12}_{6}\mathrm{C}$	12	0.158	111
${}^{16}_{8}\mathrm{O}$	16	0.120	146

Thus, beryllium requires, on average, 85 collisions to thermalize a 1 MeV neutron. Values for ξ and $\bar{n}$ for various nuclei relevant to moderator materials are summarized in Table 7-1. In this table, it is seen that ${}^{1}_{1}\mathrm{H}$ nuclei are the most efficient at thermalizing 1 MeV neutrons, requiring approximately 17 collisions, on average.

Moderating power The moderating power, P, of a material is defined as:

$$P = \sum_{i} \xi_i \Sigma_{s,i} = \sum_{i} \xi_i N_i \sigma_{s,i} \tag{45}$$

where $\Sigma_{s,i}$ is the macroscopic scattering cross section of nucleus i, which is defined as the product of the atomic density of nucleus i, N_i and the microscopic scattering cross section of nucleus i, $\sigma_{s,i}$. Because of the dependence of Equation (45) on lethargy and scattering terms, moderating power may be thought of as an efficiency of moderation. That is, neutrons will slow down with fewer collisions using moderators with higher P-values.

The purpose of slowing neutrons is to obtain thermal neutrons from fast neutrons. Thus, the appropriate scattering cross sections to use are in the epithermal regime [188]. In general, elastic scattering is considered the primary mechanism for energy loss through collisions except for nuclei with very high atomic numbers.

The atomic density, N_i, may be calculated readily from the mass density and the stoichiometry. For all materials, the mass density changes as a function of temperature. Given a reference density, ρ_i^0, at a reference temperature, T_0, and a known secant coefficient of thermal expansion, α_i, the mass density as a function of temperature, $\rho_i(T)$, is calculated as [103]:

$$\rho_i(T) = \frac{\rho_i^0}{\left[1 + \alpha(T - T_0)\right]^3}$$

For metal hydrides, the equilibrium hydrogen composition changes as a function of temperature, and metal hydrides have lattice parameter changes with hydrogen content changes [6]. However, the lattice parameter changes with hydrogen content contribute much less to overall atom density than does the hydrogen content change with temperature. Moderating power as a function of temperature in 101.325 kPa of pure hydrogen for some materials considered for nuclear reactor moderator applications is presented in Figure 7-1. Note that Figure 7-1 does not account for cross section changes due to temperature. Figure 7-1 plots the moderating power as a function of temperature for various candidate moderator materials including water, metal hydrides, beryllium compounds, and graphite. It is observed that the moderating power of water and metal hydrides is significantly

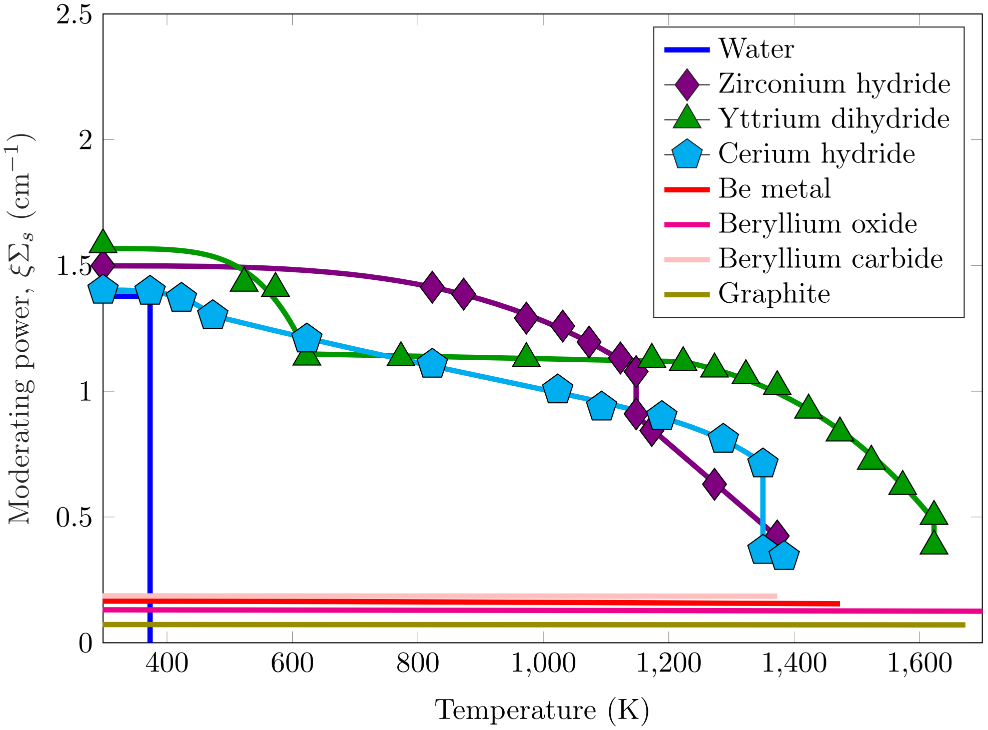

Figure 7-1: Moderating power as a function of temperature for various candidate moderator materials. All data points are taken from literature for materials at 101.325 kPa pressure. Data for metal hydrides were determined for those materials under 101.325 kPa of pure hydrogen [22, 24, 57, 59, 84, 189–201].

higher than for beryllium compounds and graphite. This makes sense, as the primary moderating nucleus in water and metal hydrides is hydrogen, which is much more efficient at slowing down neutrons than any other nucleus. As a result, metal hydrides and water are more efficient at thermalizing neutrons than are the beryllium-based compounds and graphite. However, one advantage of beryllium-containing compounds and graphite is that their moderating power is nearly constant over temperature with only small changes due to thermal expansion. Conversely, metal hydrides may have large changes in moderating power with temperature due to changes in equilibrium hydrogen content as a function of temperature. It is for this reason that yttrium dihydride (YH_2) is attractive as a metal hydride moderator, as its hydrogen content is relatively constant from approximately 600 to 1200 K under atmospheric pressures of pure hydrogen, where zirconium hydride and cerium hydride lose hydrogen with temperature in this regime. However, maintaining a hydrogen pressure is optimistic. In most realistic scenarios, hydrogen dissociation will occur.

7.2 Moderating ratio

The equation for moderating power, Equation (45), does not account for the loss of neutrons due to neutron absorption. A simple parameter to account for this is the macroscopic neutron absorption cross section, Σ_a. Combining the moderating power with the macroscopic absorption cross section results in the moderating ratio, R, which is a dimensionless quantity.

For a moderator with the chemical formula $\mathrm{A}_a\mathrm{B}_b\mathrm{C}_c \cdot .. \mathrm{Z}_z$, the density of each atomic specie, K,

Neutronic considerations

Table 7-2: Moderating lethargy, power, and ratio for various candidate moderator materials at room temperature and ambient pressure.

Material (-)	ξ (-)	P (cm^{-1})	R (-)
H_2(g)	1.00	5×10^{-4}	61.5
H_2O (l)	0.707	1.38	62.1
$ZrH_{2.0}$(s)	0.674	1.66	37.5
$YH_{2.0}$(s)	0.674	1.22	17.3
$CeH_{2.0}$(s)	0.671	0.94	22.9
Be (s)	0.207	0.17	134
BeO (s)	0.163	0.13	174
Be_2C (s)	0.190	0.19	149
Graphite	0.158	0.07	202

is given as:

$$N_K = \eta_K \frac{\rho_t N_A}{M_t} \tag{46}$$

where η_K is the number of atoms of specie K in the chemical compound, ρ_t is the total mass density of the compound, and M_t is the total molar mass of the compound. As before, N_A is Avogadro's number. Thus,

$$P = \frac{\rho_t N_A}{M_t} \sum_i \xi_i \eta_i \sigma_{s,i} \tag{47}$$

$$\Sigma_a = \frac{\rho_t N_A}{M_t} \sum_i \eta_i \sigma_{a,i} \tag{48}$$

$$R = \frac{\sum_i \xi_i \eta_i \sigma_{s,i}}{\sum_i \eta_i \sigma_{a,i}} \tag{49}$$

As seen in Equation (49), the macroscopic cross sections are present in the numerator and denominator of the moderating ratio. Thus, the dependence of the moderating ratio on the atomic density disappears. This means that the moderating ratio provides information on the moderating ability of a chemical compound and ignores density. For example, the moderating ratios of liquid water and steam are both 62.1, although liquid water is a much better moderator, due to its higher density of hydrogen atoms (over three orders of magnitude higher than that of steam). As another example, an ideal gas of hydrogen has a very low atomic density. Its moderating power is very low ($5 \times 10^{-4}\,\mathrm{cm}^{-1}$) but its moderating ratio is very high (61.5) because it is 100% hydrogen. A selection of moderating ratios for some candidate moderator materials at room temperature are summarized in Table 7-2, which shows that the materials with high hydrogen density tend to have high moderating power, but low moderating ratio due to neutron absorption by other atoms in the compounds. Conversely, the beryllium-containing and carbon-containing moderator compounds have very low moderating powers, but very high moderating ratios, due to the small neutron absorption cross sections of beryllium-9, oxygen-16, and carbon-12. The compounds shown here are the primary candidate moderator materials of interest.

7.3 Effect of hydrogen diffusion on neutronic properties

As mentioned in section 1, the technical challenge of using zirconium hydride as a moderator is that, in the absence of a hydrogen impermeable cladding, at above approximately 800 K it begins to lose substantial amounts of hydrogen [189]; these loss rates are further increased with temperature [202, 203]. The latter could be detrimental for reliable reactor operation, and thus the use of zirconium hydrides is limited to lower-temperature applications. YH_2 was tested as a higher temperature moderator during the 1960s as part of the aircraft propulsion project [55, 113]. YH_2 was studied, but never fully developed for use in a working reactor system. Yet it was recognized even then that YH_2 could be used at temperatures up to 1100 K with no significant change in the hydrogen density.

One of the challenges of metal hydrides is that under the influence of a temperature gradient, hydrogen redistributes within the hydride's adjacent metallic bond and migrates [204]. This hydrogen diffusion under a temperature gradient is due to Soret diffusion (high temperature particles having higher energy, thus diffusing) and to Fick diffusion resulting from pressure-composition-temperature (PCT) relations (equilibrium concentrations along isobars change as a function of temperature) [54]. This weakness has been a critical argument against the use of metal hydrides in reactors due to the inherent non-linearity in reactor dynamics resulting from hydrogen migration. Simply put, when hydrogen migrates inside a reactor core, it leads to fluctuations in the behavior and performance of the system. The hydrogen relocates within the yttrium hydride moderator, leading to local changes in material properties. As such, the neutronic, mechanical/structural, and heat transfer physics are directly affected. In terms of neutronic effects, local fast and thermal cross sections are interrupted due to changes in the availability of hydrogen. The shift in hydrogen leads to changes in thermophysical properties, which, in turn, would lead to deviations in the temperature and material stress profile. Asymmetric geometrical changes in materials and evolving temperature profiles change the microscopic and macroscopic neutron cross sections, which develop into further neutronic complications. Note that during this convoluted physical process, it is still necessary to account for overall actinide and non-actinide inventory of the fuel for proper neutronics modeling. All the details described above result in a shift of the local and global neutron energy spectra, and thus, effective neutron multiplication of the system, which affects criticality. It is easy to imagine how non-linear and complicated it can become to design a hydride-moderated reactor without accounting for the hydrogen migration complications and the fluctuations within the reactor system from the beginning until the end of reactor life. This effect is described in the paragraph below.

Lower hydrogen concentrations result in a decrease the heat capacity of YH_2 due to lower availability of hydrogen. Lower hydrogen content (H/Y ratio) introduces phonon splitting in the YH_2 crystal, which in turn, ends up increasing the thermal scattering properties, $S(\alpha, \beta)$, per atom for certain energies [47]. Higher hydrogen concentration tends to make the YH_2 material less ductile, thus causing it to be more likely to crack, break, or pulverize [24, 101]. On one hand, more hydrogen content in a reactor is beneficial from a neutron-stopping-power perspective. On the other hand, more hydrogen could compromise the structural integrity of moderator material in the reactor. As such, localized regions of high hydrogen concentration in the moderator material could lead to severe material deformation and/or failure. Higher temperatures in the hydride favor higher hydrogen diffusion rates, but also lower concentrations. This drives the reactor to be more dynamic, which requires more predictive tools, which are currently being developed to help understand hydrogen dynamics in metal hydrides [54].

8 Historical irradiation in the Fast Flux Test Facility

Irradiation tests can provide moderator behavior under various neutron irradiation environments for licensing purposes. Three different sets of data can be obtained from irradiation experiments: (1) characterization of materials under irradiation for the first time, (2) justification of the behavior of a reactor in both normal and accident conditions through graded NQA-1 experiments, and (3) assessment and/or confirmation of the byproducts created by irradiation (e.g., gas generation, chemical attack).

Due to its properties, yttrium dihydride (YH_2) was selected as the high temperature moderator for the Fast Flux Test Facility (FFTF) at the Hanford Site for various anticipated missions related to the production of beneficial isotopes. YH_2 moderator was irradiated in the FFTF for 138 equivalent full power days (EFPD) during Cycle 9A (September 1986) in the Cobalt Test [205], for 10 EFPD during Cycle 11A (May 1989) for the Multiple Isotope Irradiation (MIP) Test [206], for 185 EFPD in the Materials Open Test Assembly (MOTA)-1D (August 1985), and for 203 EFPD in the fusion MOTA-2B (May 1991). In addition, YH_2 was selected for the high temperature moderator for the Space Isotope Production (SIP) core in FFTF for producing ^{238}Pu with low ^{236}Pu for the National Aeronautics and Space Administration from the irradiation of ^{237}Np [206]. In preparing for these various missions, in-reactor and out-of-reactor tests were completed that assessed the properties of YH_2, such as the hydrogen to yttrium ratio, the hydrogen diffusion and permeation rates, the effect of microstructure on hydriding, the effect of impurities on performance, and the effects of the hydriding procedure on the material properties. These were integral performance tests of specific configurations rather than basic materials properties tests.

The behavior of YH_2 in a microreactor-specific design must be known before it can be licensed for use. To fully qualify YH_2 in a microreactor, a Nuclear Quality Assured (NQA-1) experiment must achieve a representative fluence. The User's Guide for Experiments in FFTF included a table relating the various test requirements to NQA-1 requirements.

For FFTF irradiations and laboratory tests, the hydrogen content in YH_2 pellets was measured by a scale that determined the weight change from the hydriding process. The requirements were that the weight had to change by the amount expected from the hydriding process, and the YH_2 had to pass through a go-no go diameter gage. Bowing of the 5 cm long pellets was checked by the gage, and some machining of the pellets was allowed so that the pellet could fit through the gage. The cladding was exposed to the sodium and was relied on for structural integrity. The temperature of the YH_2 was calculated for the proposed configuration and materials, and as long as the calculated YH_2 temperature was below the value that would result in high hydrogen partial pressure, then the test could proceed, as the hydrogen pressure would not be exceeded. Coatings to reduce hydrogen permeation from free hydrogen were used on the inside and outside of the steel cladding tubes for the Cobalt Test and some MOTA tests, but later tests (such as the MIP test) did not have these coatings, and no coatings were proposed for the SIP project.

No post irradiation information for YH_2 from these FFTF tests (such as phase diagrams) was located.

9 Post-irradiation examination of yttrium dihydride irradiated in the Advanced Test Reactor

9.1 Introduction to the ATR irradiations

As presented in the previous sections, a significant amount of data exists for the thermodynamics and thermophysical properties of yttrium dihydride (YH_2). This material has been used in reactors, most notably the Fast Flux Testing Facility (FFTF) reactor. However, post-irradiation examination (PIE) data of this material are lacking and, thus, inadequate to support its use in microreactors. To establish a materials qualification strategy for solid moderators, the impact of neutron irradiation effects on the solid moderator's form and function must be qualified. Therefore, the effect of irradiation on the critical material properties and dimensional stability must be determined for irradiated YH_2. This result will serve as the basis for solid moderator qualification and will inform microreactor performance and safety codes.

To that end, fission reactor neutron irradiations of YH_2 were performed in the B2 position of the Advanced Test Reactor (ATR) at Idaho National Laboratory (INL). A total of 102 YH_2 specimens, 36 titanium-zirconium-molybdenum (TZM) sheets, passive instrumentation (12 melt wires, 6 fluence wires, and 3 silicon carbide passive thermometry sticks) were encapsulated in 6 TZM capsules. These capsules were irradiated in ATR for two months (60 full power days) starting on February 19, 2021, and ending on April 19, 2021. Samples were transported to INL's Hot Fuels Examination Facility (HFEF) on June 16, 2021. The irradiation assembly was disassembled on October 6, 2021, after which PIE commenced.

The rest of this section describes the PIE of YH_2 completed through fiscal year 2023 (FY23). Much of this work has been documented extensively in technical reports prepared for the Microreactor Program [207–210].

Neutron radiography of the irradiated assembly was the first PIE activity completed. After this, specimens were retrieved from capsules in the HFEF hot cells. Specimens were catalogued and packaged with serial numbers. Fluence wires were shipped to Pacific Northwest National Laboratory (PNNL) for study. Silicon carbide passive thermometry sticks and melt wires were studied at INL. YH_2 samples were shipped to INL's Analytical Laboratory for basic inspection, including optical microscopy, as well as mass, volume, and density measurements. Hydride samples were subsequently measured for thermal diffusivity using laser flash analysis and temperature-dependent energetics using differential scanning calorimetry.

9.2 Hydride fabrication

The starting material for all YH_2 samples prepared for this experiment was legacy yttrium metal stock that was available in the Sigma Division of Los Alamos National Laboratory (LANL). From here on, this metal ingot and the metal samples produced from it will be referred to as Sigma yttrium. Figure 9-1 shows this ingot with holes cored out to prepare samples for the irradiation.

Slices of the Sigma yttrium ingot were sent to NSL Analytical Services, Inc. (Cleveland, OH) for chemical analysis using inductively coupled plasma mass spectroscopy. The composition of the Sigma yttrium with 95% confidence intervals of each element composition is given in Table 9-1. The fact that the confidence intervals for the chemistry are large indicates a large degree of inhomogeneity in the ingot. Indeed, the three sets of samples were measured to have zirconium compositions of 2200 ppm, 9200 ppm, and 5300 ppm by weight.

Post-irradiation examination of yttrium dihydride irradiated in the Advanced Test Reactor

(a) Ingot

(b) Example samples

Figure 9-1: (a) Legacy stock yttrium ingot available at the Sigma Division of LANL. (b) Example metal samples machined from the yttrium ingot. Figures courtesy of M. Pate (LANL).

Table 9-1: Composition summary of yttrium metal used for ATR sample fabrication.

Element (-)	Composition (wt. ppm)
Y	bal.
Zr	5567 ± 6840
O	2900 ± 1103
N+C	275 ± 69
Fe	223 ± 92
Transition metals (excl. Fe and refractories)	190 ± 69
Refractories (excl. Zr and Ta)	110 ± 138
Group I metals	100 ± 89
Group II metals	93 ± 63
Rare Earth metals	70 ± 59
Nonmetals (excl. O, C, N)	50
Metalloids	41 ± 55

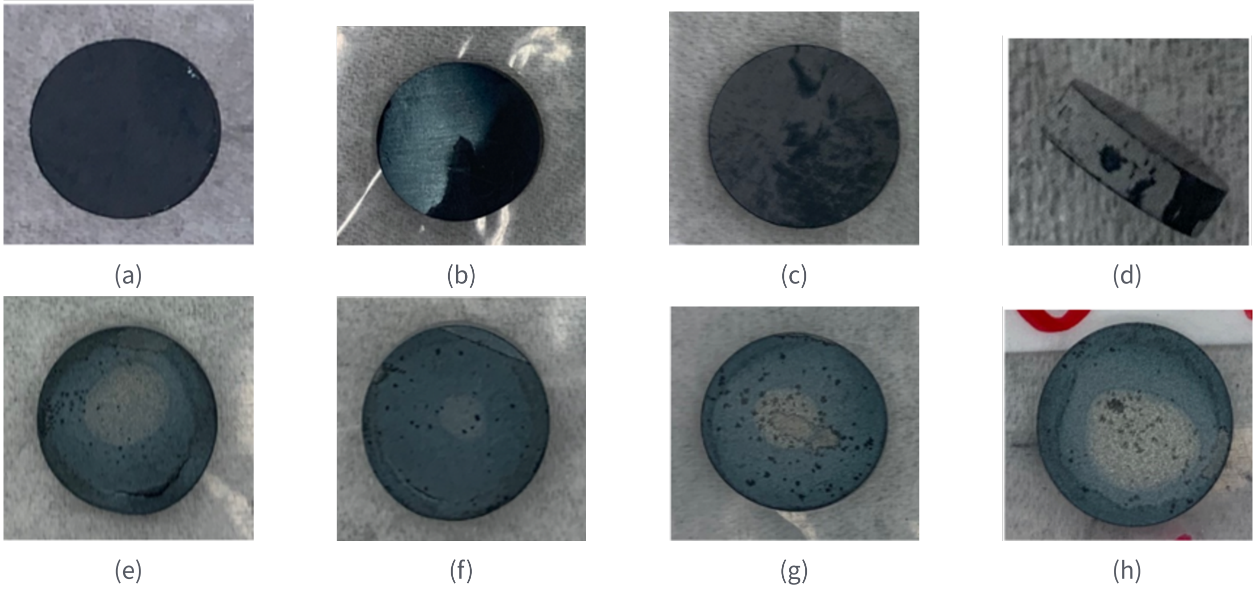
(a) (b) (c) (d)
(e) (f) (g) (h)

Figure 9-2: Example samples prepared for ATR irradiation experiments. (a)-(d) show examples of direct hydride samples, while (e)-(h) show examples of powder metallurgy samples.

YH_2 samples were fabricated in a variety of geometries for this experiment. Materials were fabricated using either the direct hydriding (DH) method or the powder metallurgy (PM) process. Both of these processes are described in section 4. For each targeted irradiation temperature, 17 samples were fabricated using each method (i.e., 17 DH samples and 17 PM samples). DH samples and PM samples to be irradiated at the same temperature were placed in separate irradiation capsules. Examples of as-fabricated samples are shown in Figure 9-2. A complete list of samples fabricated for the ATR irradiation is presented in Tables 9-2 and 9-3; Table 9-2 summarizes the initial data for all PM samples, while Table 9-3 summarizes the initial data for all DH samples. Both tables contain comments on the appearance of samples prior to loading into irradiation capsules.

In Figures 9-2(e) to 9-2(h), discolorations are observed on several PM samples. As will be shown in section 9.6.4, these discolorations appear to be associated with regions of low hydrogen content. From this, it is likely that many of the PM samples did not have homogeneous hydrogen contents in the as-fabricated state, which makes interpretation of PIE data challenging for these samples.

Table 9-2: Data summary of PM samples prepared for ATR irradiations. Density was compared against a theoretical value of $4.28\,\mathrm{g\,cm^{-3}}$ [22].

Sample ID (-)	Diameter (mm)	Thickness (mm)	Mass (g)	Density (% of TD)	Comment (-)
022020-3	12.11	2.09	1.004	97.45	PITTING
, 022020-4	12.16	2.08	1.000	96.72	
022020-10	12.13	2.15	1.009	94.88	PITTING
022420-1	12.2	2.1	1.002	95.37	PITTING ONE SIDE, DISCOLORATION OTHER SIDE
022420-2	12.17	2.17	0.986	91.26	CIRCULAR CRACK, DISCOLOR
022420-3	12.2	2.09	0.964	92.19	
022420-5	12.21	2.1	0.952	90.46	
022520-5	4.88	1.58	0.121	95.67	SMALL CHIP
022520-6	4.88	1.57	0.12	95.48	
022520-7	4.85	1.57	0.122	98.27	
022520-9	4.87	1.59	0.122	96.24	MINOR OXIDATION, PITTING
030520-7	12.26	2.07	0.96	91.79	MINOR PITTING
030520-9	12.17	2.09	0.979	94.09	MINOR OXIDATION, PITTING
030520-10	12.17	2.07	0.967	93.83	MINOR OXIDATION, MINOR PITTING
030520-11	12.23	2.01	0.962	95.19	MINOR OXIDATION, PITTING
030520-13	12.15	1.98	0.951	96.79	MINOR PITTING, MINOR OXIDATION
030520-15	12.13	1.98	0.957	97.72	MINOR PITTING, MINOR OXIDATION
030520-18	12.17	2.02	0.955	94.96	CIRCULAR CRACK, PITTING
0306-11	4.88	1.52	0.117	96.15	
030620-1	12.25	9.56	4.774	99.00	MINOR OXIDATION, PITTING POSSIBLE
030620-5	4.94	1.47	0.118	97.85	
030620-6	4.88	1.52	0.116	95.33	
030620-9	4.88	1.41	0.107	94.80	SMALL CHIP
030620-10	12.28	9.5	4.778	99.22	OXIDATION, PITTING,
030620-13	12.2	9.51	4.752	99.87	MINOR PITTING, MINOR OXIDATION
030620-17	4.86	1.44	0.108	94.46	
030620-22	12.26	9.49	4.779	99.67	
030920-1	12.18	9.79	4.912	100.61	PITTING, EDGE CHIP
030920-4	4.86	1.73	0.132	96.10	MINOR PITTING
030920-6	4.86	1.54	0.118	96.51	PITTING ON ONE SIDE
030920-8	4.86	1.55	0.119	96.70	PITTING ON ONE SIDE
030920-9	4.86	1.51	0.116	96.76	
030920-12	4.91	1.43	0.109	94.06	MINOR OXIDATION
031020-1	12.25	9.80	4.944	100.01	MINOR OXIDATION
031020-4	12.25	9.77	4.926	99.95	SEVERE CIRCULAR CRACK, PITTING
031020-5	12.26	9.81	4.956	99.99	MINOR CIRCULAR CRACK, MINOR PITTING
031020-6	12.28	9.78	4.94	99.65	OXIDATION, PITTING,
031020-8	12.15	2.09	0.998	96.23	SEVERE CIRCULAR CRACK, MINOR PITTING
031020-9	12.13	2.08	0.997	96.91	PITTING
031020-10	12.12	2.11	0.995	95.50	PITTING
031020-11	12.13	2.14	1.004	94.86	PITTING
031020-12	12.12	2.13	0.996	94.70	MINOR CIRCULAR CRACK, MINOR PITTING
031120-2	12.19	2.12	0.986	93.11	DISCOLOR, MINOR PITTING
031120-4	12.14	2.10	1.000	96.12	MINOR OXIDATION, PITTING POSSIBLE
031120-5	12.14	2.09	0.993	95.90	MINOR CIRCULAR CRACK, PITTING
031120-6	12.16	2.09	0.994	95.68	CIRCULAR CRACK, PITTING
031120-7	12.19	2.12	0.997	94.15	CIRCULAR CRACK, PITTING
031120-12	4.88	1.44	0.11	95.42	MINOR OXIDATION
031120-13	4.88	1.45	0.111	95.63	
031120-14	4.9	1.43	0.109	94.44	CIRCULAR CRACK ONE SIDE
031120-15	4.92	1.42	0.107	92.60	ROUGH SURFACE

Table 9-3: Data summary of DH samples prepared for ATR irradiations. Hydrogen content was determined gravimetrically after hydriding, assuming all mass gain was due to hydrogen absorption.

Sample ID (-)	Diameter (mm)	Thickness (mm)	Mass (g)	H content (H/M)	Comment (-)
172-3	12.408	5.07	9.988	1.97	GROUND TO FINAL SIZE
182-2	12.425	5.07	9.987	1.89	ONE SIDE GROUND, ONE SIDE ROUGH
182-3	12.402	5.08	9.977	1.9	GROUND TO FINAL SIZE, DISCOLORATION BROWN/WHITE
186-1	12.402	5.07	9.95	1.88	GROUND TO FINAL SIZE, DISCOLORATION BROWN/WHITE
186-3	12.472	5.1	9.953	1.88	OXIDATION
186-4	12.45	5.03	9.924	1.88	OXIDATION
194-1	4.95	0.12	1.478	1.88	MODLED APPEARANCE
194-2	12.068	0.93	1.968	1.89	MINOR OXIDATION
194-3	12.135	0.88	1.886	1.83	MODLED APPEARANCE
194-4	12.209	0.86	1.888		OXIDATION ON SIDES
194-5	12.085	0.87	1.838	1.8	MINOR OXIDATION
194-6	12.176	0.94	1.94	1.88	OXIDATION ON SIDES
194-7	12.044	0.93	1.97	1.85	MINOR OXIDATION
194-8	12.096	0.92	1.934	1.86	OXIDATION ON SIDES
194-9	12.144	0.91	1.935		MINOR OXIDATION ON SIDES
194-10	12.12	0.82	1.768	1.88	EDGE MINOR OXIDATION
204-4	12.499	5.24	10.016	1.9	PARTIAL GRIND
210-1	12.49	5.21	10.003	1.94	GRIND ONE SIDE
210-4	12.505	5.23	10.009	1.92	GRIND ONE SIDE
210-9	12.09	0.87	1.842		GROUND TO FINAL SIZE
216-1				1.65	GROUND TO FINAL SIZE, DARK GREY
216-2	4.938	0.13	1.508	1.64	GROUND TO FINAL SIZE, DARK GREY
216-3	4.94	0.12	1.498	1.65	GROUND TO FINAL SIZE, DARK GREY
216-4	4.935	0.12	1.493	1.65	GROUND TO FINAL SIZE, DARK GREY
216-5	4.932	0.11	1.507	1.65	GROUND TO FINAL SIZE, DARK GREY
216-8	4.927	0.12	1.484	1.65	GROUND TO FINAL SIZE, DARK GREY
216-9	4.941	0.12	1.491	1.65	ODD SHINE FROM POLISH
216-10	4.94	0.12	1.495		
221-2	4.927	0.12	1.479	1.71	GROUND TO SIZE
221-3	4.934	0.11	1.492	1.99	
221-4	4.935	0.12	1.46	1.78	GROUND TO SIZE
221-6	4.925	0.12	1.483	1.72	
221-8	4.928	0.12	1.506	1.96	
221-9	4.959	0.12	1.464		GROUND TO SIZE, OXIDATION ON SIDES
221-10	4.936	0.12	1.508	1.84	GROUND TO SIZE
221-11	4.913	0.12	1.501	1.79	
221-12	4.942	0.11	1.494	1.85	GROUND TO SIZE
221-14	5.008	0.12	1.508	1.58	GROUND ON ONE SIDE
252-A3	12.419	1.02	1.981	1.8	GROUND TO SIZE
252-A4	12.461	1.02	1.986	1.8	GROUND TO FINAL SIZE
252-A5	12.587	1.04	2	1.81	GROUND TO FINAL SIZE
252-A6	12.389	1.01	1.991	1.81	GROUND TO SIZE
252-A7	12.482	1.03	1.985	1.79	GROUND TO FINAL SIZE
252-A8	12.456	1.04	1.989	1.84	GROUND, ROUGH SURFACE
252-A9	12.451	1.02	1.998		GROUND TO FINAL SIZE
252-A10	12.456	1.03	1.995	1.84	GROUND TO SIZE
261-1	12.44	1.032	1.999		GROUND TO SIZE ONE SIDE
261-2	12.421	1.035	2.001	1.84	GROUND TO SIZE ONE SIDE
261-3	12.451	1.033	1.991	1.89	GROUND TO SIZE ONE SIDE
261-4	12.43	1.001	1.951	1.81	PARTIAL GRIND ONE SIDE
261-5	12.468	1.052	1.988	1.85	PARTIAL GRIND TWO SIDES

9.3 Irradiation capsule design

Six irradiation capsules were fabricated with the intention of studying the neutron irradiation response of YH_2 as a function of irradiation temperature and fabrication method. Each capsule was assembled with 17 YH_2 samples fabricated by either Sieverts gas absorption DH or the PM process. Capsules 1, 2B, and 3A contained samples fabricated by PM, while Capsules 4, 5, and 6 contained samples fabricated by Sieverts gas absorption DH. Samples were offset from one another using six TZM sheets and one TZM ring per capsule. Melt wires were inserted inside the TZM ring. YH_2 fabrication and capsule assembly were both performed by Sigma Division at LANL. Fluence wires, melt wires, and silicon carbide thermometry sticks were inserted in each temperature capsule inside the TZM rings. A schematic of an irradiation capsule is shown in Figure 9-3. Specimens were identified as RUS, glow discharge optical emission spectroscopy (GDOES), transmission electron microscopy (TEM), laser flash analysis (LFA), or differential scanning calorimetry (DSC), depending on the sample geometry for the desired PIE technique. Sample quantities and geometries are summarized in the Yttrium Hydride Post-Irradiation Examination Plan [207]. Assembled capsules are shown in Figure 9-4, except Capsule 2B. Surface oxidation on the capsule lids was noticed after welding. Capsules 1, 2, 3A, 4, 5, and 6 all passed helium gas leak checking. However, Capsule 2B successively failed helium leak checking, indicating a crack in the capsule. A crack at the weld section was observed using optical microscopy; this crack extended through the wall thickness of the TZM capsule. This is shown in Figure 9-5.

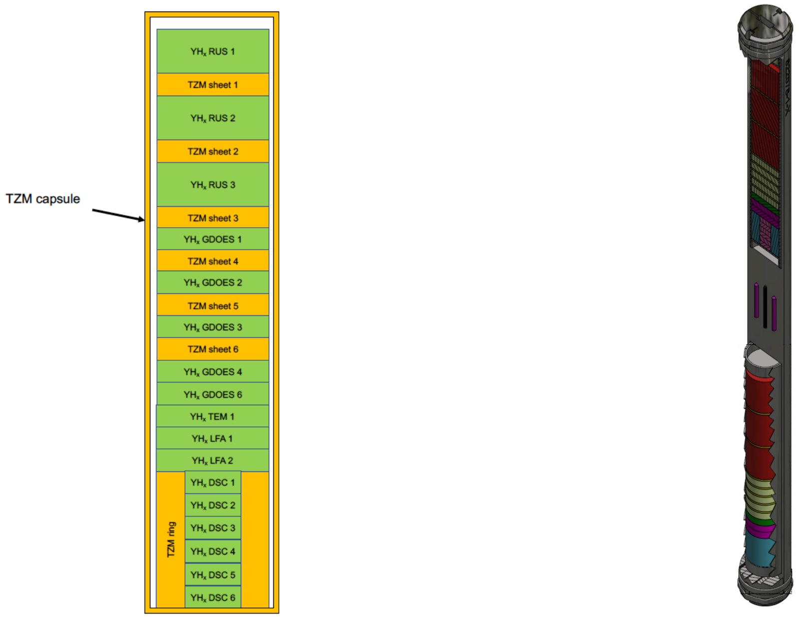

(a) (b)

Figure 9-3: Schematic of specimen stacking in TZM capsule. (a) A 2D cross section of the TZM irradiation capsule. Green: yttrium dihydride samples; orange: TZM fixturing. Samples are labeled with intended PIE technique. (b) A 3D rendering of two TZM capsules intended for a single temperature.

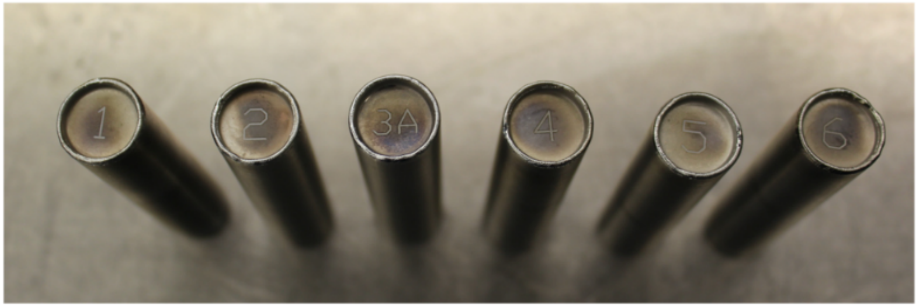

Figure 9-4: Picture of assembled capsules, except Capsule 2B.

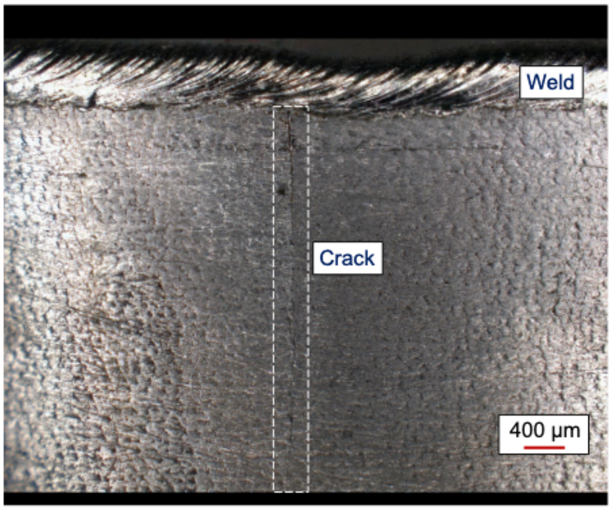

Figure 9-5: Optical micrograph of the weld section of Capsule 2B with the crack highlighted.

9.4 Summary of irradiation conditions

The three targeted temperatures for irradiation were 873, 973, and 1073 K (600 °C, 700 °C, and 800 °C). Irradiation temperatures were estimated based on vertical position in the reactor. The irradiation temperatures for the capsules were estimated as follows: capsules 1 and 4 were irradiated at 873 K, capsules 3A and 6 were irradiated at 1073 K, and capsules 2B and 5 were irradiated at 973 K. The fast neutron fluence exhibited a skewed cosine shape that was calculated to be between 1.05-1.25 cm^{-2}. The nominal average design temperature of each capsule and the fast fluence distribution are shown in Figure 9-6. The irradiation temperatures overlayed with capsule gas compositions are given in Figure 9-7. As noted above, Capsule 2B had a crack at the weld location [208]. The crack in Capsule 2B was expected to act as a path for gas exchange between the capsule and free volume of the ATR basket, which was filled with a helium/argon gas mixture. As such, the gas composition of Capsule 2B would not contain the intended 10 Torr (1333 Pa) of hydrogen gas. The thermal analysis of the irradiation was redone assuming the capsule was filled with air to estimate the worst condition. The consequence of the crack was that the average calculated temperature of Capsule 2B increased from 972 K to 1042 K. The impact to the expected temperatures of the other capsules was determined to be minimal.

Post-irradiation examination of yttrium dihydride irradiated in the Advanced Test Reactor

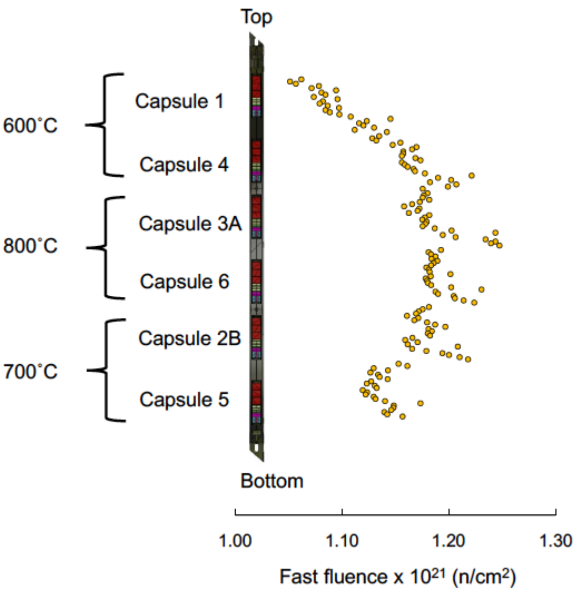

Figure 9-6: Calculated capsule design temperatures and the calculated fast fluence distribution.

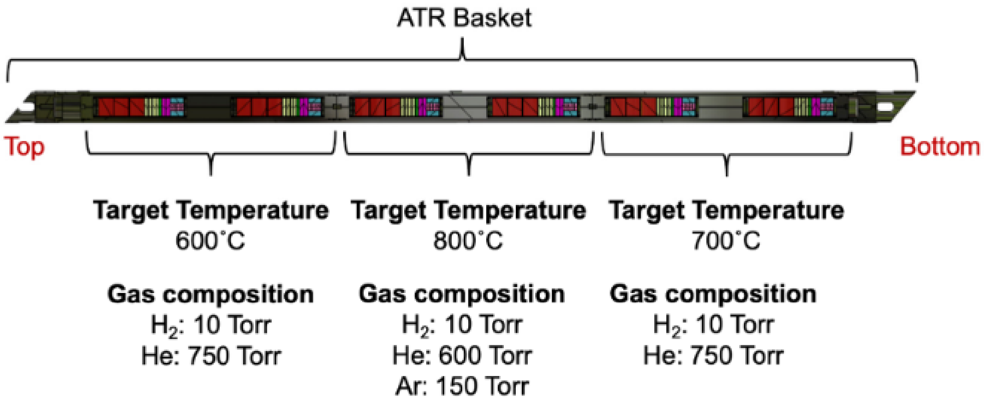

Figure 9-7: Predicted irradiation temperatures and gas compositions of irradiation capsules.

9.5 PIE techniques

Neutron radiography After irradiation, the basket containing the capsules was imaged using neutron radiography at the East Radiography Station of the Neutron Radiography Reactor (NRAD) at HFEF. The basket was placed in an aluminum carrier and sample positioning was determined using a gadolinium-filled ruler to enable ruler gradations to be viewed in transmission neutron images. The high spatial resolution indirect transfer method was used to produce images. Briefly, this method uses reactor neutrons to penetrate the sample; transmission neutrons interact with dysprosium, cadmium, and indium foils to image the thermal and epithermal neutrons. The radioactive foils are then placed on an electron sensitive X-ray film in a dark room for five half-lives for the β^- decay of dysprosium and indium. The image is formed through electron-stimulated chemical reactions in the X-ray film. The basket was imaged at two elevations with 190.5 mm overlap and three orientations of 0°, 120°, and 240° by manual rotation. Further details of the neutron radiography measurements are given in [209].

Fluence wire examinations Two types of neutron fluence wires were used in this study: (1) iron-titanium-niobium (FeTiNb) alloy wires and (2) aluminum-cobalt (AlCo) alloy wires. Six neutron fluence wires were fabricated at PNNL, where they were electron-beam sealed in vanadium capsules. Details of their fabrication are given in [211]. Following irradiation, the vanadium capsules and fluence wires were shipped back to PNNL for analysis. At PNNL, the fluence wires were removed from the capsules. The FeTiNb wires were dissolved in a mixture of nitric and hydrofluoric acids and small aliquots of the dissolved wire were deposited on filter paper. This aliquoted filter paper was then counted for gamma rays using low energy germanium detectors to measure the X-rays emitted by niobium-93m, which has a half-life of 16.1 years. Gamma detectors were calibrated using National Institute of Standards and Technology (NIST) traceable standards following ASTM standard E1297 [212].

Melt wire examinations Melt wires of pure or alloyed metals with known compositions and melting points were used to passively determine peak irradiation temperatures during the test. These melt wires were encapsulated in quartz ampoules and were placed inside specific capsules based on the target irradiation temperature. Two melt wires were placed in each capsule in the TZM rings. After irradiation, melt wires were inspected visually using an optical microscope to determine whether melting had occurred, which indicates the range of the peak temperature experienced by the capsule during the test.

Optical inspection of samples After removal from the capsules, YH_2 samples were inspected using a Dino-Lite AM73915MZTL digital microscope calibrated using a NIST-certified external standard purchase from Klarmann Rulings. This standard enabled dimensional inspections with $\pm$ 7×10^{-4} mm uncertainties.

Density measurements YH_2 samples were measured for mass changes using a Mettler-Toledo XPR204 four-place analytical balance that had been calibrated by the INL Calibrations and Standards Laboratory. Balance performance was checked daily and corrected for temperature fluctuations. Hydride sample volumes were measured using a Micromeritics AccuPyc II 1345 Gas Displacement Pycnometer. This system operates under a similar principle as a Sieverts apparatus, but uses inert gas (helium, in this case) to measure the volume of a sample by calibrating against known sample volumes. Finally, the density was calculated using mass and volume measurements with uncertainties propagated from both mass and volume measurement techniques.

Hydrogen content measurements An ELTRA ONH-2000 inert gas fusion (IGF) analyzer was used for hydrogen measurements. Prior to reference standard and irradiated specimen tests, blank runs with empty tin capsules were performed to evaluate and correct for the hydrogen content of the capsules during the data analysis. The instrument was calibrated with NIST traceable and certified reference standards, having hydrogen contents bounding those predicted for the sample. The calibration runs were then checked by analyzing an independent NIST traceable certified reference standard with hydrogen content near the middle of the calibrated range. After calibration checks, the specimens were tested. An additional check standard run was applied at the end of the sample batch and at least every hour during the analysis to evaluate the detector drift.

The hydrogen concentration of each sample (c_H^{sample}) was calculated using Equation (50):

$$c_H^{\text{sample}} = \frac{K_H\, A_{\text{sample}} - A_{\text{BG}}}{M_{\text{sample}}} \tag{50}$$

where K_H is the sensitivity constant of the instrument for hydrogen determined through the analysis of a known standard, A_{sample} is the sample peak area, A_{BG} is the sum of all background contributions to the peak area determined experimentally, and M_{sample} is the net weight of the sample minus the capsule weight. The average hydrogen content is then calculated as the arithmetic mean of a set of individual samples.

X-ray diffraction XRD measurements were performed in a Panalytical Empyrean equipped with a Pixel 3D detector using a 0.02 µm nickel filter. The goniometer radius was configured to 240 mm, Soller slits of 0.04 radians, anti-scatter slit of 0.25°, and divergence slit of 1.125° (140 mm distant from the sample). A silicon zero-background was used as the sample holder. Scans were acquired using Copper K_α radiation. Voltage and current were 45kV and 40mA, respectively, and 2θ ranged from 20 to 140° in Bragg-Brentano geometry, with step size of 0.013° and 200 seconds per step.

Phase identification was carried out in Highscore software from Panalytical, using PDF4+ database. Rietveld refinements were done with TOPAS software from Bruker, version 4.2. Significant grain size effects were noted for most samples. To reduce the influence of this effect, some crystalline phases were refined with preferential orientation using the March-Dollase algorithm embedded in the TOPAS software.

Thermal diffusivity The thermal diffusivities of the irradiated hydride samples were measured using a glovebox Netzsch LFA using ASTM standard E1461 [213]. The glovebox was maintained with 1 ppm oxygen and less than 5 ppm water. Thermal diffusivity standards used to verify instrument calibration included Pyroceram 9600 (magnesium aluminosilicate glass) and pure iron ($>$ 99.9% pure). Specimen holders were painted with yttrium(III) oxide to minimize interaction between hydride specimens and the surroundings. Ultra-high purity argon gas was used as the cover gas. Sample measurements were made at 25 and 50 K temperature increments. Specimens were measured up to 1123 or 1273 K temperature. Thermal diffusivity was determined using the pulse-corrected Cowan model.

Differential scanning calorimetry DSC scans were measured using a Netzsch DSC 404F1 differential scanning calorimeter. Samples were placed in platinum-rhodium crucibles lined with yttrium(III) oxide. DSC was measured upon heating and cooling at a rate of $10\,\mathrm{K\,min^{-1}}$. Ultra-high purity argon was used as the cover gas at a flow rate of $20\,\mathrm{mm^3/min}$ after passing it through an oxygen gettering furnace. Oxygen impurity levels were below the parts-per-billion range based on the measured performance of the gettering furnace. All instruments were contained within an argon atmosphere glovebox with less than 1 parts-per-million oxygen.

9.6 PIE results

9.6.1 Neutron radiography

Neutron radiographs of the ATR fixture at orientations of 0°, 120°, and 240° are shown in Figure 9-8. The six capsules contained specimens from top to bottom. The color map in Figure 9-8 depicts black to white regions as having zero to full neutron absorption contrast. That is, black regions had full transmission of neutrons, while white regions had almost no transmission of neutrons. No defects or failures of the ATR basket or TZM capsules were detected after irradiation and following transport from ATR to NRAD.

A closeup of the individual capsules at 240° is shown in Figure 9-9. In this figure, it is observed that some regions of the YH_2 samples exhibited neutron transmission contrast variations. This is most clearly seen in Capsules 1, 2B, and 4. This contrast variation indicates some hydrogen concentration variation within specific samples, though this behavior is not observed in all samples of a particular capsule or in all capsules. The temperature of Capsule 1 was 883 K, and Capsule 2B was 1088 K, as calculated using finite element analysis. Specimens in Capsules 1 and 2B were prepared by PM. Specimens in Capsule 3A were fabricated using PM methods but did not exhibit such behavior, and specimens in Capsule 4 showed subtle gradation in the neutron radiographs but were fabricated using DH. The contrast variation in specimens which were irradiated at 873 K (target), appeared to have a continuity for axially stacked specimens. Melt wire data from the bottom of Capsule 1 suggested a radial temperature gradient, as will be discussed below. However, the same contrast difference was not observed in other samples of the same capsule.

Another observation was the contrast variation in the specimens which were irradiated in the 973-1083 K Capsule 2B. The first specimen and the third specimen (starting from the top) both exhibited a contrast variation in the radial direction, but the second specimen had no visible contrast variation. These observations could also be indicative of some manufacturing-related effect. As will be shown in later sections, these samples also had optically visible features corresponding to the contrast variations, which were also observed prior to irradiation. Acknowledging the caveat of the specimen temperature measurements, the observed contrast variation was likely caused by a manufacturing-related effect or the non-uniform cooling after irradiations.

Post-irradiation examination of yttrium dihydride irradiated in the Advanced Test Reactor

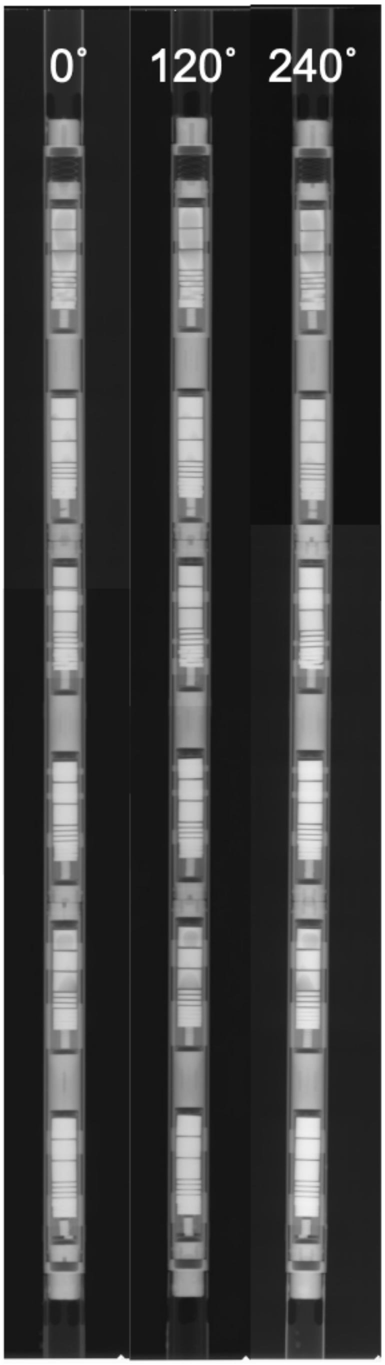

Figure 9-8: Neutron radiography of the ATR basket and yttrium dihydride irradiation capsules with specific hydride samples. Images were taken at 0°, 120°, and 240°.

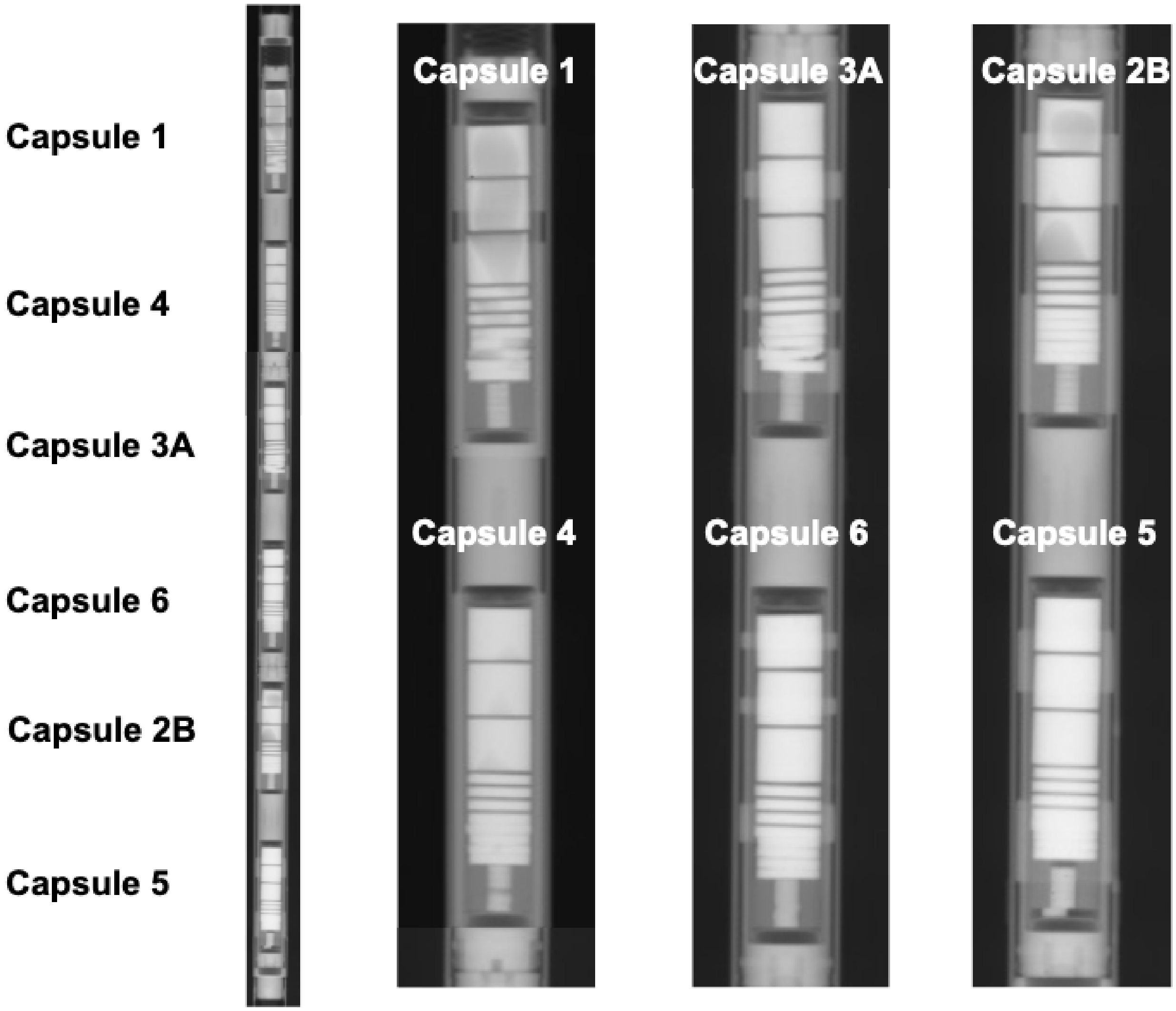

Figure 9-9: Neutron radiographs of individual capsules at an angle of 240°.

9.6.2 Specimen integrity during retrieval

Because YH_2 is brittle, one important attribute is its mechanical integrity after irradiation. The neutron radiographs in Figures 9-8 and 9-9 indicated that all samples were intact within the irradiation assembly. Table 9-4 shows the status of the samples and planned PIE activities after capsule opening at HFEF's main hot cell. Upon opening the capsule, several samples mechanically failed prior to handling with hot cell manipulators. Additionally, several samples had bonded to one another. The number of broken, powdered, and bonded specimens were three, five, and six respectively.

For Capsule 3A, the bonded specimens were all DSC type (5 mm diameter, 1.5 mm thickness). No TZM sheet was present in between these specimens. Within this capsule, DSC-1, -2, and -3 were bonded together to form a single specimen, while DSC-4 and -5 bonded to form another. Additionally, GDS-5 and LFA-1 samples were broken. GDS specimens of Capsule 4, fabricated using DH, came out of the capsule as powders. These specimens had TZM sheets in between. Within Capsule 5, sample GDS-3 bonded to the adjacent TZM sheet and DCS-5 was broken. In total, 88 of 102 hydride specimens were retrieved intact. Additional specimens were broken during inter-facility transfers. Retrieved pieces of an individual broken specimen were used for multiple characterizations, as allowed.

Table 9-4: The planned PIE activities (color-coded). Capsules 1, 2B, and 3A contained PM specimens, while Capsules 4, 5, and 6 contained directly hydrided specimens.

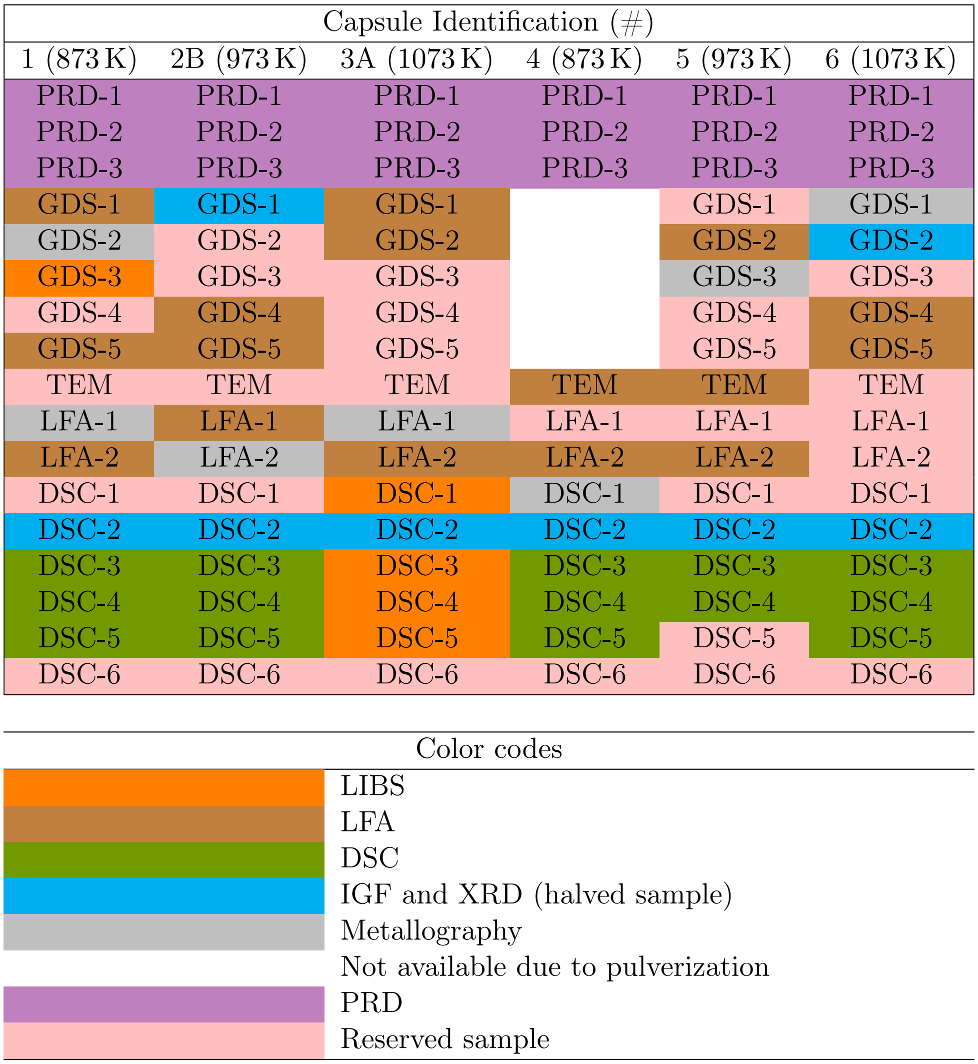

Capsule Identification (#)					
1 (873 K)	2B (973 K)	3A (1073 K)	4 (873 K)	5 (973 K)	6 (1073 K)
🟪 PRD-1	🟪 PRD-1	🟪 PRD-1	🟪 PRD-1	🟪 PRD-1	🟪 PRD-1
🟪 PRD-2	🟪 PRD-2	🟪 PRD-2	🟪 PRD-2	🟪 PRD-2	🟪 PRD-2
🟪 PRD-3	🟪 PRD-3	🟪 PRD-3	🟪 PRD-3	🟪 PRD-3	🟪 PRD-3
🟫 GDS-1	🟦 GDS-1	🟫 GDS-1	⬜	🟥 GDS-1	▒ GDS-1
▒ GDS-2	🟥 GDS-2	🟫 GDS-2	⬜	🟫 GDS-2	🟦 GDS-2
🟧 GDS-3	🟥 GDS-3	🟥 GDS-3	⬜	▒ GDS-3	🟥 GDS-3
🟥 GDS-4	🟫 GDS-4	🟥 GDS-4	⬜	🟥 GDS-4	🟫 GDS-4
🟫 GDS-5	🟫 GDS-5	🟥 GDS-5	⬜	🟥 GDS-5	🟫 GDS-5
🟥 TEM	🟥 TEM	🟥 TEM	🟫 TEM	🟫 TEM	🟥 TEM
▒ LFA-1	🟫 LFA-1	▒ LFA-1	🟥 LFA-1	🟥 LFA-1	🟥 LFA-1
🟫 LFA-2	▒ LFA-2	🟫 LFA-2	🟫 LFA-2	🟫 LFA-2	🟥 LFA-2
🟥 DSC-1	🟥 DSC-1	🟧 DSC-1	▒ DSC-1	🟥 DSC-1	🟥 DSC-1
🟦 DSC-2	🟦 DSC-2	🟦 DSC-2	🟦 DSC-2	🟦 DSC-2	🟦 DSC-2
🟩 DSC-3	🟩 DSC-3	🟧 DSC-3	🟩 DSC-3	🟩 DSC-3	🟩 DSC-3
🟩 DSC-4	🟩 DSC-4	🟧 DSC-4	🟩 DSC-4	🟩 DSC-4	🟩 DSC-4
🟩 DSC-5	🟩 DSC-5	🟧 DSC-5	🟩 DSC-5	🟥 DSC-5	🟩 DSC-5
🟥 DSC-6	🟥 DSC-6	🟥 DSC-6	🟥 DSC-6	🟥 DSC-6	🟥 DSC-6

Color codes	
🟧	LIBS
🟫	LFA
🟩	DSC
🟦	IGF and XRD (halved sample)
▒	Metallography
⬜	Not available due to pulverization
🟪	PRD
🟥	Reserved sample

9.6.3 Neutron fluence and thermometry

Fluence wires Three sets of fluence wires were contained within the irradiation capsule. Detailed analysis of the fluence wires has been provided by PNNL and included in the PIE documentation. Table 9-5 shows the fluence wire results along the ATR reactor elevation at the B2 irradiation position, based on activity measurements. The fast fluence for neutron energies greater than 0.1 MeV was measured as 1.28, 1.40, and 1.27 $1 \times 10^{21}\,\mathrm{cm}^{-2}$.

Melt wires Most of the melt wires were damaged during retrieval. Therefore, limited information was extracted from the melt wire assessment (see Table 9-6). The main takeaways from the melt wire analysis were as follows:

- The capsules that were expected to be at 883 K likely experienced a radial temperature gradient where one side was higher than 903 K and the other side was lower than 850 K

Post-irradiation examination of yttrium dihydride irradiated in the Advanced Test Reactor

Table 9-5: Measured and calculated fluences of irradiation capsules.

Capsule (-)	Calculated fast ($E \geq 0.1$ MeV) fluence ($1 \times 10^{21}\,\mathrm{cm}^{-2}$)	Measured fast ($E \geq 0.1$ MeV) fluence ($1 \times 10^{21}\,\mathrm{cm}^{-2}$)
1 4	1.61	1.28
3A 6	1.71	1.40
2B 5	1.67	1.27

- Capsules that were expected to be around 1083 K likely experienced higher temperatures, above 1138 K
- For capsules at 988 K and 1042 K, no maximum temperature was determined due to lack of melt wires operating around 973 K.

Table 9-6: Melt wire examination results.

Capsule (-)	Temperature (K)	Wire composition (-)	Melting point (K)	Capsule condition (-)	Result (-)
1	882	88Al-12Si	850	Intact	No melt
1	882	100Sb	903	Intact	Melt
4	883	100Sb	903	Intact	Melt
4	883	88Al-12Si	850	Broken	Unknown
3A	1084	98.2Cu-1.8Be	1138	Damage	Probable melt
3A	1084	98.2Cu-1.8Be	1138	Damage	Probable melt
6	1086	98.2Cu-1.8Be	1138	Broken	Unknown
6	1086	98.2Cu-1.8Be	1138	Broken	Unknown
2B	1042	100Al	933	Broken	Melt
2B	1042	49Au-16Cu-23Zn-7.5Mn-4.5Ni	954	Broken	Unknown
5	988	49Au-16Cu-23Zn-7.5Mn-4.5Ni	954	Intact	Melt
5	988	100Al	933	Intact	Melt

Silicon carbide passive thermometry Maximum and minimum irradiation temperatures of the ATR capsule were measured with a silicon carbide (SiC) passive monitor (see Table 9-7). All irradiated passive monitors were evaluated with optical dilatometry during an isochronal heat treatment. SiC monitors were located between capsules of the same target temperature, in the middle of the clam shell fixture. At these locations, finite element analysis (FEA) computed higher temperatures than the maximum specimen temperatures in the capsules. All three SiC monitors exhibited some level of physical degradation during the capsule disassembly process in the hot cells, but maintained enough integrity to be used for the dilatometry measurements. The SiC monitor that was aimed for 1060 K was measured as 1133 K maximum temperature.

Table 9-7: SiC temperature monitor results with FEA-calculated target temperatures at monitor locations.

	Irradiation temperature (K)				
	FEA-calculated		SiC-measured		Difference
Sample	At SiC location	Specimen max	Min	Max	|Max − Target|
1	942	883	863	903	39
2	1060	1042	1123	1133	63
3	1108	1086	1083	1123	15

9.6.4 Metallography of irradiated yttrium dihydride

Optical inspection of each sample was conducted to determine morphological changes or degradation (e.g., cracking) that was visible to the naked eye. This was followed by more detailed optical microscopy, as well as scanning electron microscopy (SEM) with energy-dispersive X-ray spectroscopy (EDS) and electron backscatter diffraction (EBSD). The samples with contrast change, as depicted in Figure 9-9, were carefully inspected using microscopy to understand the effect of this contrast change on microstructure. Instead of providing all the optical pictures of specimens, specimens with important observations are presented below.

Sample integrity and inspection Small diameter specimens (DSC samples) showed better mechanical integrity than the large diameter specimens. DSC specimens of Capsule 3A (PM) were retrieved as bonded to each other, except one.

Figure 9-11 shows typical DSC-type specimens after removal from their respective irradiation capsules. In this figure, the samples fabricated using PM are shown on the left and the direct hydride samples are shown on the right. Generally, the samples exposed to lower temperatures (Capsules 1 and 4) showed very little decomposition but did exhibit some surface color variations. As Capsules 2, 3, 5, and 6 were all exposed to temperatures at, or near, 1073 K, degradation was expected to be uniform. However, some specimens appeared to have completely dehydrided (see samples 700-2B and 800-6 in Figure 9-11), while others appeared to remain hydrides (see samples 700-5 and 800-3A in Figure 9-11). This will be discussed in greater detail in section 9.6.5.

Microscopy of direct hydride specimens Figure 9-12 shows EBSD information for the DSC-1 specimen of Capsule 5, while Figure 9-13 shows EDS data for the same regions. Briefly, this sample was cross-sectioned and polished and then measured in an SEM using the aforementioned techniques. Scans were performed in the center of the sample, halfway to the outer edge, and at the outer edge. This was done for several DH and PM samples.

Generally, Figure 9-12 shows a fairly textured specimen where each grain crystallographically indexed well to YH_2. It is observed that the EBSD maps that index well to YH_2 actually stop short of the specimen edges at the bottom and at the right. This could be due to hydrogen loss at the periphery of the sample, as the phase identity at this location would be yttrium metal if this were the case. This sample was retrieved from Capsule 5, which had a target temperature of 988 K, though this could have been higher, as indicated by the SiC passive thermometry (see Table 9-7). At these temperatures, slow hydrogen loss would not be unexpected. Although hydrogen loss has only been observed starting around 1073 K under similar conditions [25], those results were for short-time tests (order of hours) where this irradiation took place over 60 days.

The EDS results in Figure 9-13 show similar features to those in Figure 9-12. That is, regions

Post-irradiation examination of yttrium dihydride irradiated in the Advanced Test Reactor

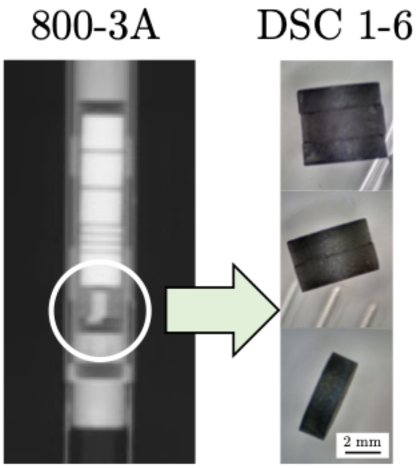

Figure 9-10: DSC samples of capsule 800-3A (Powder metallurgy)

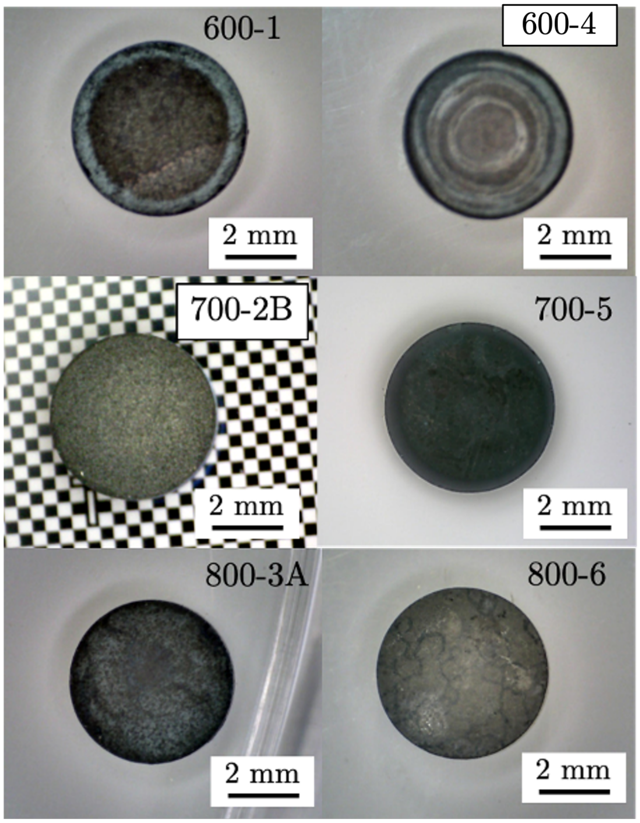

Figure 9-11: Typical DSC samples for depiction of observed surface features.

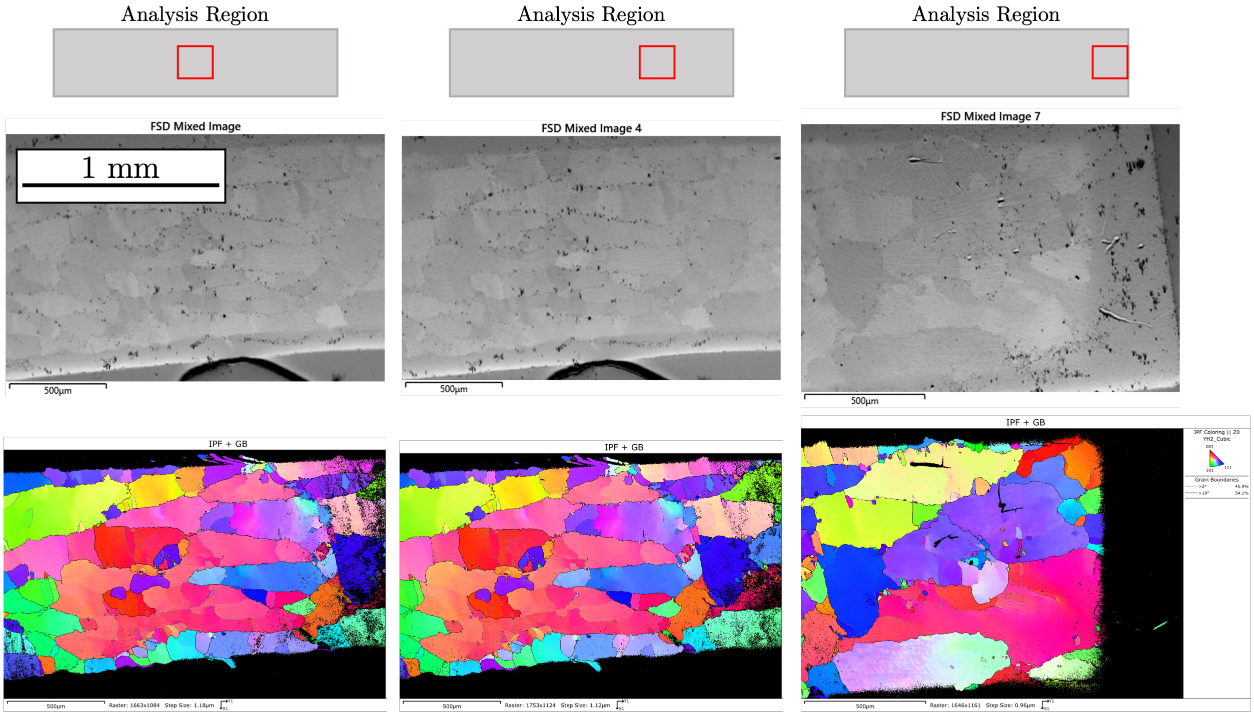

Figure 9-12: EBSD data taken from the DSC-1 sample of Capsule 5 (direct hydride). Note that the scale bar is the same for all images.

in the sample of DSC-1 at the periphery exhibit differences in yttrium fluorescence intensity, which may indicate hydrogen redistribution. Additionally, small oxygen-rich particles dotting the YH_2 phase boundaries are observed. it is not currently known whether these particles were present in parent metal material (Sigma yttrium), were formed during the hydriding process, were formed due to irradiation, or were formed during the sample preparation process. The lack of prior data makes interpretation of PIE results difficult. This result highlights the importance of specimen characterization prior to irradiation.

Microscopy of powder metallurgy specimens Figures 9-14 and 9-15 show the EBSD and EDS information for the LFA-1 specimen of Capsule 2B, respectively. Note that Capsule 2B was the cracked capsule that was anticipated to have a higher target temperature than originally planned. The sample was examined in a similar manner as the DSC-1 specimen of Capsule 5; that is, the sample was cross-sectioned and examined in the center, far edge, and halfway between the center and far edge.

Unlike the DH specimen in Figure 9-12, the PM specimen in Figure 9-14 has a much more equiaxed, randomly oriented grain structure, which is expected of a sample produced using PM. The specimen appears to have many surface features that appear to coincide with higher oxygen content, as shown in Figure 9-15. It is likely that many of these features formed during sample preparation, as they are out of plane with the sample surface. However, it is also likely that many of these oxygen-rich regions were also present in the as-fabricated state, as oxidation was noted for several samples in Tables 9-2 and 9-3. More extensive characterization prior to irradiation would have enabled better interpretation of this result. As with the DH sample, the specimen edges appear

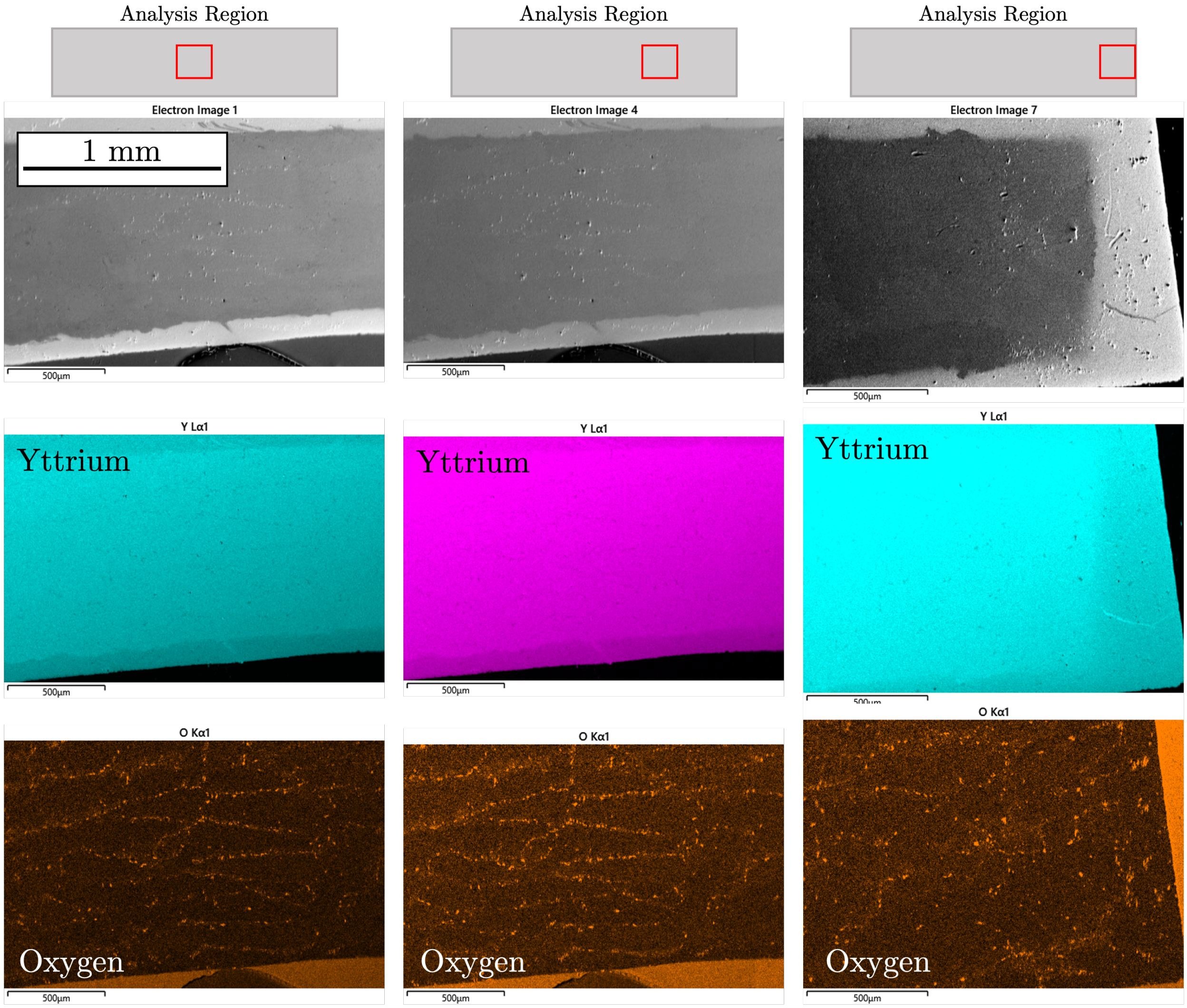

Figure 9-13: EDS data taken from the DSC-1 sample of Capsule 5 (direct hydride). Note that the scale bar is the same for all images.

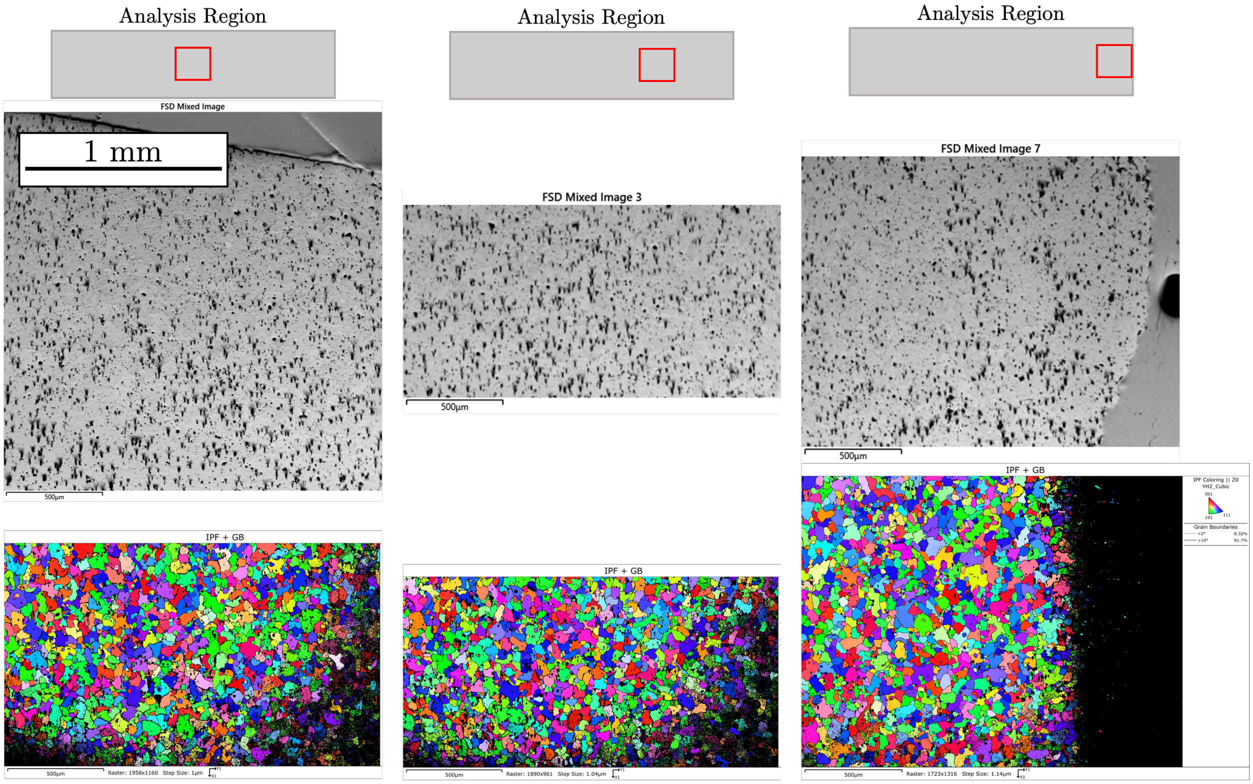

Figure 9-14: EBSD data taken from the LFA-1 sample of Capsule 2B (powder metallurgy). Note that the scale bar is the same for all images.

to not index well to YH_2 and the EDS maps of the periphery region show lower yttrium content at the edges, which again appears to indicate hydrogen loss from this region of the sample.

Hydrogen content variations in certain powder metallurgy samples Specimens from Capsule 1 with visible contrast variations in the neutron radiography of large diameter specimens exhibited a significant color difference ranging from gold, gray-blue, light-gray, and dark-gray, dependent on the particular light conditions. The color alteration was volumetric, verifying the radiography data, and not limited to the surface of samples. Microscopy examination using EBSD showed that the majority of grains indexed as the YH_2 phase, except oxide, Y metal, and other precipitates (see Figure 9-16) which indicated that the color alterations were related to the grain morphology and potential lack of hydrogen.

Further elemental analysis at the color-changing regions with EDS detected molybdenum at noise levels (Figure 9-17), which indicates that the discoloration was not due to diffusion of molybdenum from the TZM foils placed between samples. Oxygen was also observed together with yttrium, indicating the presence of oxide precipitates. Zirconium was determined as present in the starting YH_2 material. Thus, the observed color changes were considered related to hydrogen content variations inside the YH_2 samples. Based on the images taken of the as-manufactured samples, it is determined that the hydrogen content variations and, thus, color changes, were present in several PM samples prior to irradiation, as shown in Figure 9-2. Thus, it is difficult to deconvolute the effect of irradiation from the manufacturing.

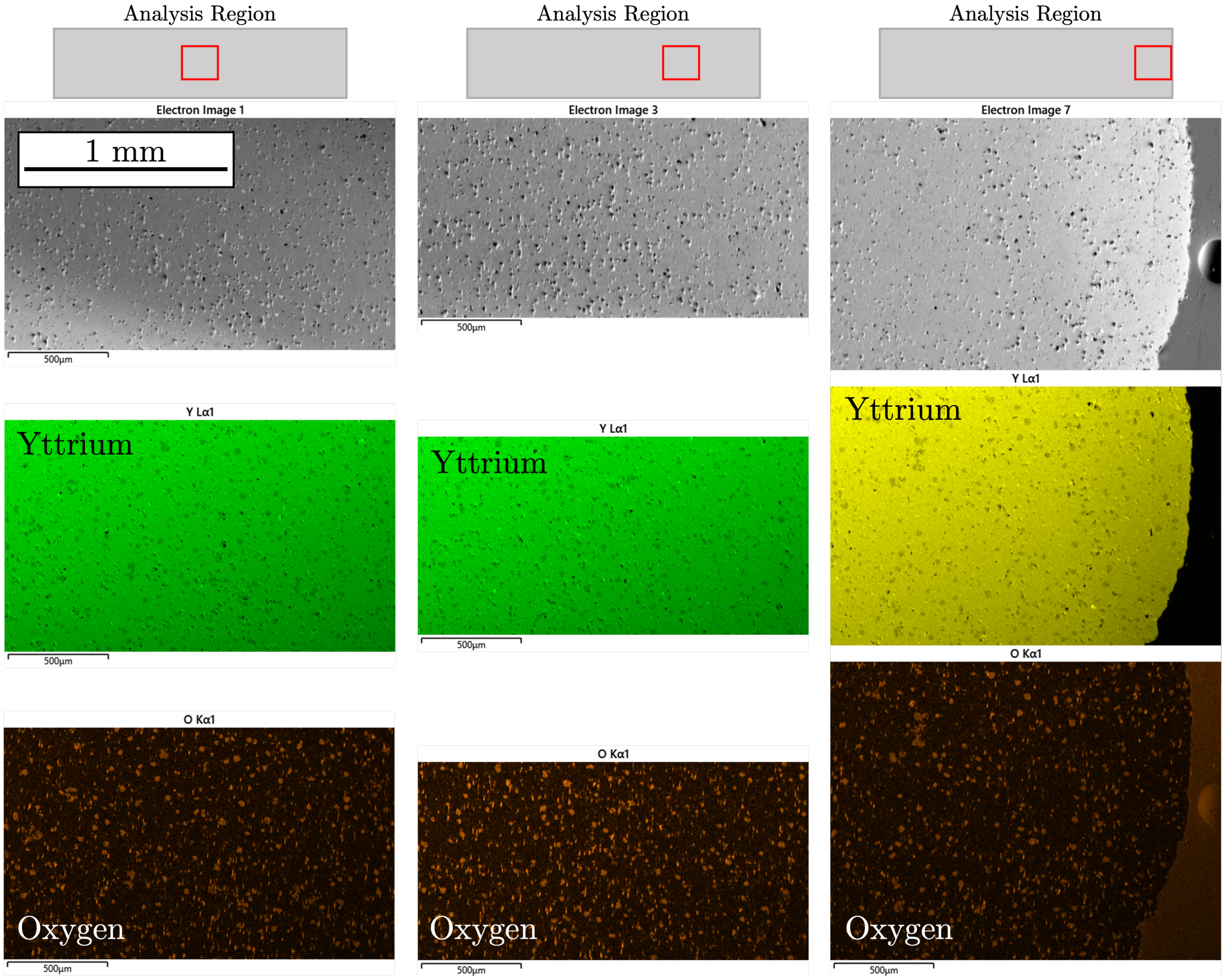

Figure 9-15: EDS data taken from the LFA-1 sample of Capsule 2B (powder metallurgy). Note that the scale bar is the same for all images.

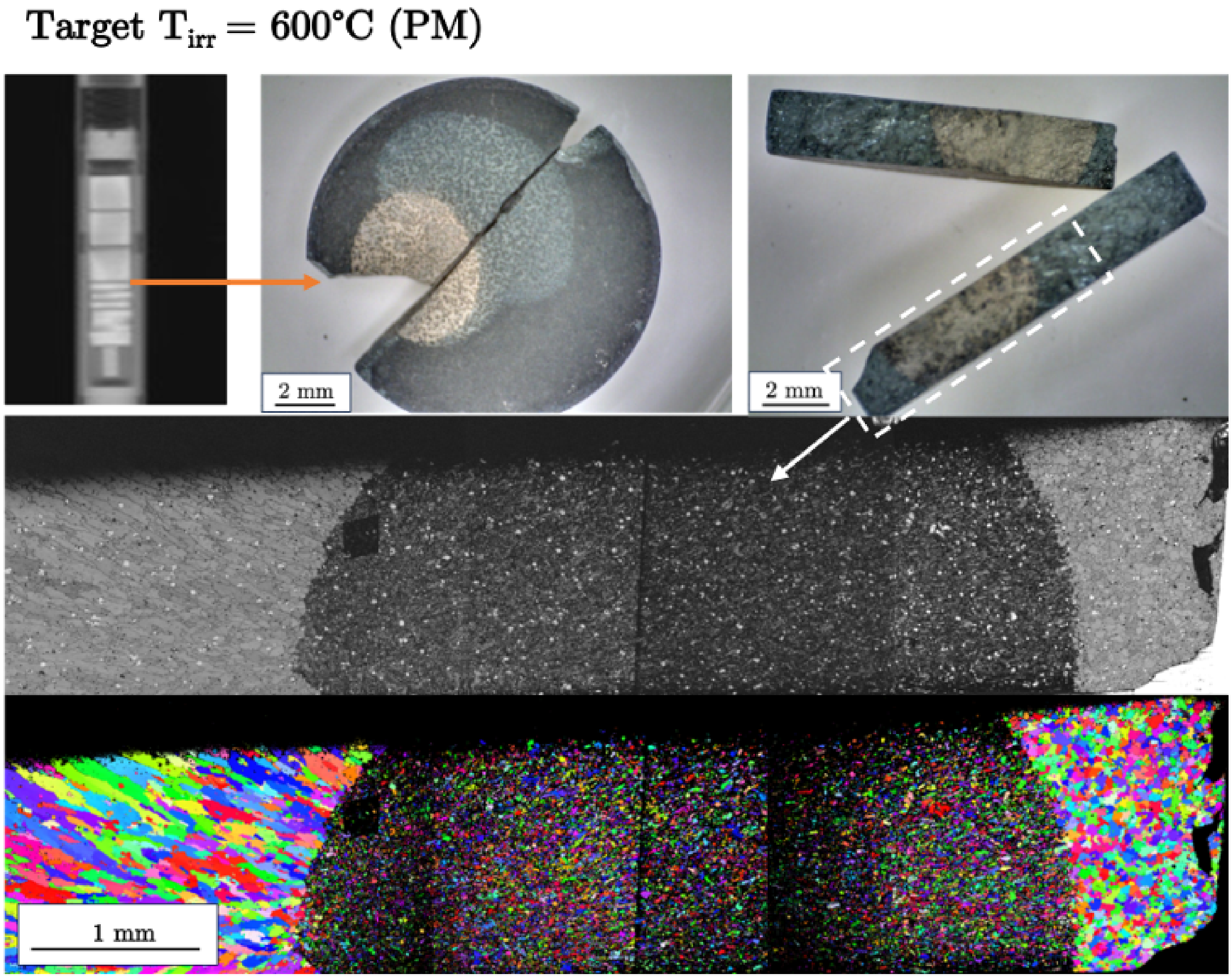

Figure 9-16: Optical and microscopy examinations of a typical specimen with significant color alteration. EBSD indexed all major grains, except oxides and other precipitates, as YH_2.

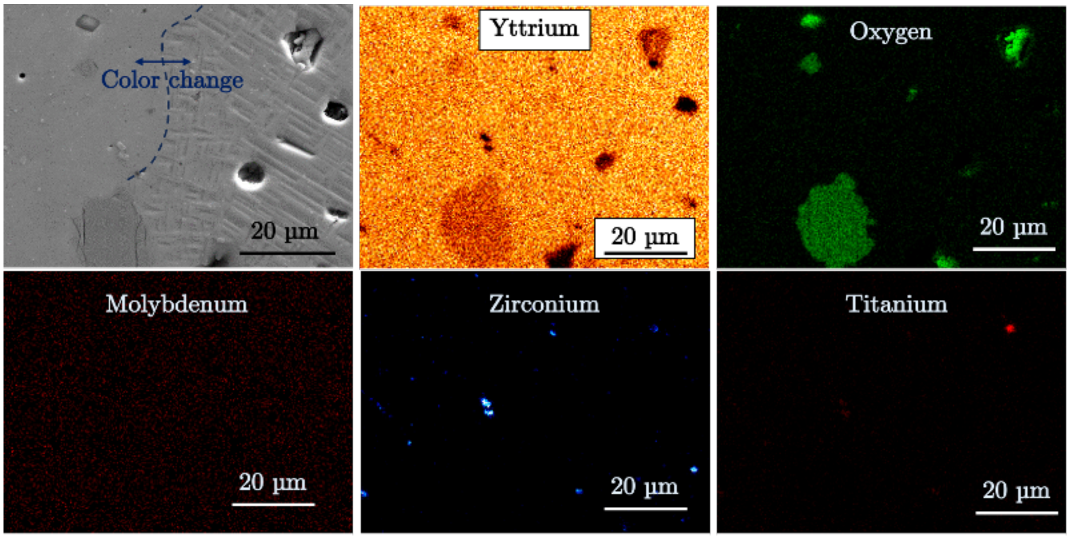

Figure 9-17: Secondary electron image of the specimen where color change occurs and EDS elemental maps. Molybdenum is at the noise level of the EDS signal.

This result highlights the importance of characterizing these samples prior to irradiation. Although high-quality samples have been produced in the past using both the DH and PM processes [6, 25], the samples produced for this irradiation were not sufficiently characterized to determine phase purity and, thus, sample quality prior to irradiation.

9.6.5 Post-irradiation hydrogen content and phase purity

Inert gas fusion measurements The hydrogen content of six specimens (color-coded with blue in Table 9-4) were measured. Two additional samples from Capsules 2B (cracked) and 6 (DH) were tested to assess the impact of pressure boundary loss and the highest irradiation temperature on hydrogen retention. In total, eight irradiated specimens were prepared at the Analytical Lab at INL. Samples were stored in an inert atmosphere as long as possible prior to examination, apart from in-air storage during the first several weeks after capsule disassembly. Despite mostly being stored under inert conditions, the GDS-2 sample from Capsule 6, which was used for hydrogen content measurements, experienced significant mechanical degradation during storage.

Specimens were sheared into halves. One half of each sample was designated for XRD characterizations for phase identifications. The other halves were used for hydrogen measurements using the IGF technique. Each IGF specimen was then crushed, mixed, and sub-sampled six times (replicates). The exact method of material mixing and sampling is detailed in [209]. The results of the replicates were used to calculate the average hydrogen concentration for the YH_2 disk from which they were taken.

Table 9-8 shows the total mass measurements of the large specimens and average hydrogen contents, as determined by the IGF. Hydrogen contents of the irradiated samples showed values both lower and higher than the expected approximate value of 21,000 ppm. Hydrogen content was estimated by considering only yttrium and hydrogen. No oxygen or fluorine was included; thus, actual hydrogen contents are expected to be lower than 21,000 ppm. The original hydrogen contents for some unirradiated samples were determined by mass measurements. This technique assumes

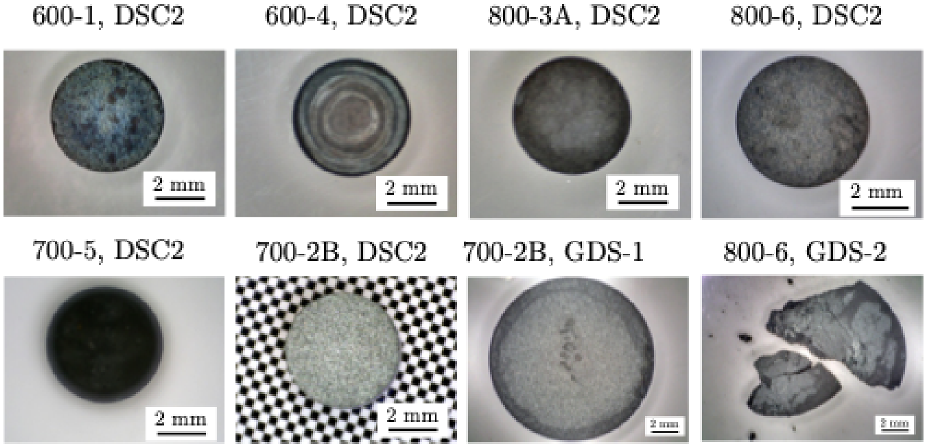

Figure 9-18: Pictures of the selected samples that were subject to IGF analysis.

that all mass gain in the sample upon hydriding is due to hydrogen uptake with no consideration of impurities. Therefore, the uncertainty in these measurements is unknown.

The hydrogen content of specimens from Capsules 1, 4, 5, and 6 was higher than expected, indicating a stoichiometry increase for those YH_2 specimens. The TZM capsules containing YH_2 samples for irradiation contained a 1.33 kPa (10 torr) partial pressure of hydrogen, as indicated in Figure 9-7. This provided an initial pressure-temperature-composition (PCT) equilibrium condition that would discourage hydrogen desorption from the YH_2 samples. It is possible that this partial pressure could have absorbed into some of the YH_2 samples of lower hydrogen content; however, it is unclear why this behavior would not be consistent for all samples. For Capsule 2B (cracked), DSC-2 and GDS-1 specimens had 15,400 and 18,200 ppm of hydrogen. For the cracked capsule's specimens, the hydrogen contents were low, as expected, due to hydrogen loss through the cracked region. The same behavior was also determined for samples from Capsule 6, where hydrogen contents of GDS-2 and DSC-2 sample were determined to be 21,200 and 16,300 ppm. It is unclear what would cause the hydrogen content in samples within the same capsule to vary so significantly. These results might suggest that some hydrogen was lost either during irradiation or post-irradiation activities. Thus, hydrogen content measurements of YH_2 were based on what was present after the capsule opening, sample storage, and specimen preparations, as well as the cooling period after irradiation. In addition, the hydrogen content of fabricated YH_2 samples prior to irradiation was estimated using mass measurements, which does not account for mass gain from impurities, such as oxygen. A scarcity in fabrication details also contribute to the lack of conclusive behavior of the post-irradiated specimens.

X-ray diffraction results Figure 9-19 shows the XRD patterns of specimens from Capsules 1 and 4. XRD indicated that YH_2 was the dominant phase, although a minority yttrium metal phase was present, as shown in the zoomed-in section of the XRD line profile. Furthermore, multiple minor phases indexed as yttrium(III) oxide and yttrium oxy-fluoride (YOF) (not shown in the figures) were determined. Because hydride intensity was significantly higher than the intensity of the metal phase, it could be qualitatively commented that hydrogen loss was minor on these specimens, which were irradiated around 873 K. Table 9-9 summarizes the phase fractions of main phases from Rietveld refinement and also includes the associated hydrogen contents. It should be noted that diffraction

Table 9-8: The masses average hydrogen contents of specimens (not replicates). Data was obtained from six replicates from each specimen.

Capsule (-)	Sample (-)	Mass (mg)	Initial H content (ppm | H/Y)	PIE H content (ppm | H/Y)
1	DSC-2	17.8 ± 0.2	-	22400 ± 2690 | 2.00 ± 0.24
4	DSC-2	17.7 ± 0.2	20605 | 1.85	22100 ± 2210 | 1.98 ± 0.20
2B	DSC-2	17.8 ± 0.2	-	18200 ± 2000 | 1.63 ± 0.18
2B	DSC-2	17.7 ± 0.2	-	15400 ± 2160 | 1.38 ± 0.19
5	DSC-2	17.5 ± 0.2	18377 | 1.65	22400 ± 1340 | 2.00 ± 0.12
3A	DSC-2	18.0 ± 0.2	-	17000 ± 1910 | 1.52 ± 0.17
6	DSC-2	17.6 ± 0.2	-	16300 ± 1790 | 1.46 ± 0.16
6	GDS-2	17.9 ± 0.2	20493 | 1.84	21200 ± 2970 | 1.90 ± 0.27

data originates from a limited volume of each sample close to the outer surface. Therefore, XRD results may not fully represent the bulk YH_2 samples.

Table 9-9: Hydrogen content of the specimens and XRD with the estimated volume fractions of important phases. DH: direct hydriding and PM: powder metallurgy. Irradiation temperatures are given as the temperatures calculated by FEA.

Capsule	Sample	T	Type	Initial H	Final H	XRD Volume fractions (%)			
(-)	(-)	(K)	(-)	(ppm)	(ppm)	YOF	Y_2O_3	Y	YH_2
1	DSC-2	873	PM	-	22400	11.09	11.98	2.42	73.38
4	DSC-2	873	DH	20605	22100	0.13	16.41	9.28	74.17
2B	DSC-2	1042	PM	-	18200	2.40	6.19	23.58	67.04
2B	GDS-2	1042	PM	-	15400	0.86	21.52	23.97	53.41
5	DSC-2	988	DH	18377	22400	0.90	3.40	45.81	49.89
3A	DSC-2	1084	PM	-	17000	4.85	32.87	12.08	49.23
6	DSC-2	1086	DH	-	16300	1.03	0.98	79.15	18.83
6	GDS-2	1086	DH	20493	21200	3.40	2.10	14.65	79.08

Figure 9-20 shows the XRD patterns of specimens in Capsule 6. GDS-2 and DSC-2 specimens were at different axial locations in Capsule 6. While the normalized intensity of YH_2 peaks were more noticeable than that for yttrium metal peaks in the GDS-2 sample, metal phase peaks were higher than the intensity of the hydride peaks, which indicated a significant hydrogen loss from that specimen.

The primary observations were:

1. Some specimens contained yttrium oxy-fluoride and yttrium(III) oxide phases at significant phase fractions. Acknowledging the factors, such as the limited X-ray penetration depth and yttrium oxidation during specimen handling, volume fractions of the secondary phases showed no consistency.

2. For specimens irradiated in Capsules 1 and 4, YH_2 phase fractions were significantly higher than that of yttrium metal, which indicated high hydrogen retention at 873 K.

3. XRD results of specimens irradiated in Capsule 6 (1073 K) indicated large hydrogen content variations and correlated XRD calculated volume fraction values between two specimens taken

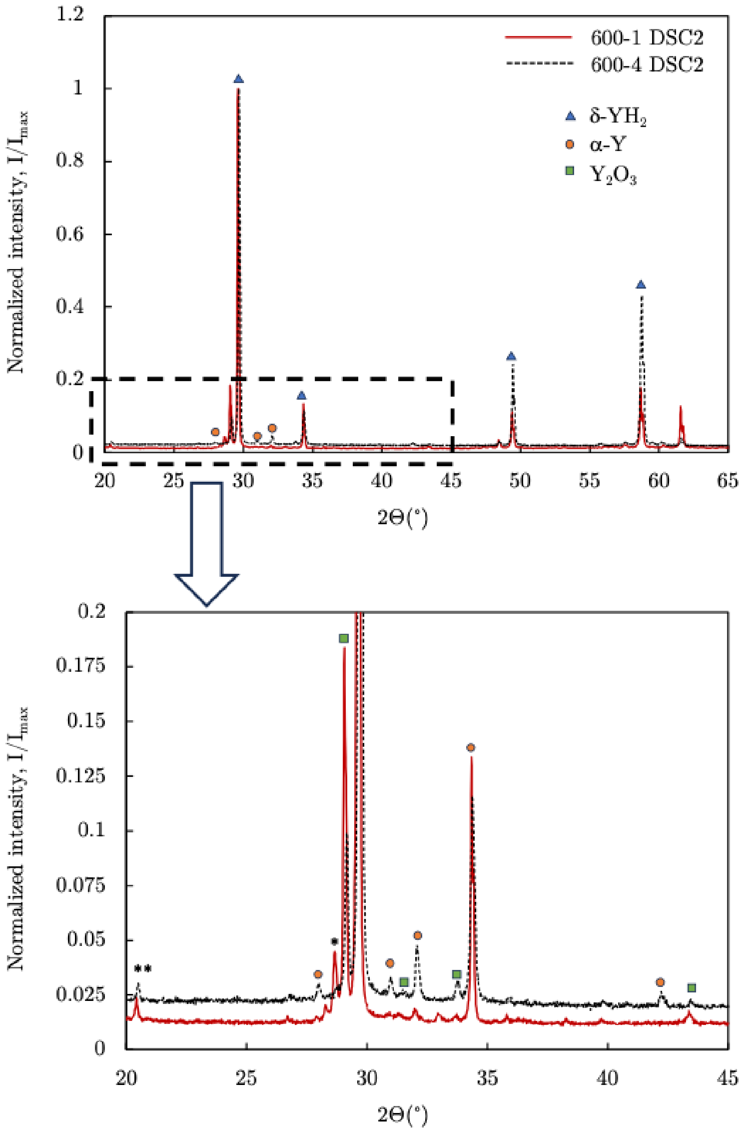

Figure 9-19: XRD patterns of specimens from Capsules 1 and 4, irradiated at 873 K.

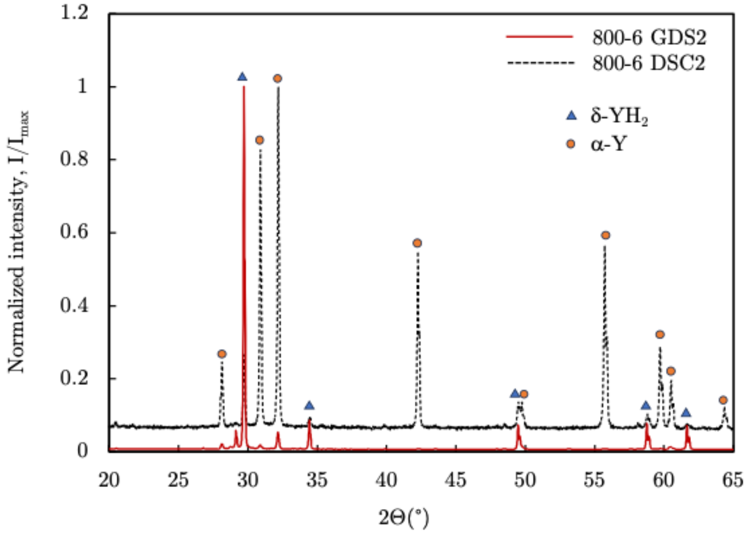

Figure 9-20: XRD patterns of specimens from Capsule 6 irradiated at 1073 K.

from different locations. Under the assumption that these samples had similar initial hydrogen contents, these observations suggested hydrogen redistribution within the capsule. Thus, it is anticipated that hydrogen redistribution is important at temperatures near 1073 K.

4. Specimens from the cracked capsule (Capsule 2B) had lower hydrogen contents and the XRD-calculated phase fractions were consistent with this observation.

9.6.6 Thermal properties of irradiated yttrium dihydride

LFA and DSC measurements were performed on ATR-irradiated YH_2 specimens, as depicted in Table 9-4, to determine the thermal diffusivity and heat capacity. Note that these measurements were not taken under hydrogen partial pressure by following the PCT curves. Therefore, the LFA and DSC results should not be treated as absolute property measurements. For a specific moderator environment, LFA and DSC results may differ. It is suggested that data from the initial heating runs could be used as a representative thermal property for the fuel performance codes. Because LFA and DSC measurements were taken up to 1073 K, hydrogen loss was expected to change the specimen hydrogen content and, thus, the collected data. This enabled tracking of the hydrogen loss using thermal property signature.

LFA measurements The thermal diffusivity (in $\mathrm{mm}^2\,\mathrm{s}^{-1}$) values of fresh and irradiated YH_2 discs are shown in Figures 9-21 to 9-23 for samples irradiated at target temperatures of 873, 973, and 1073 K, respectively. The main observations of thermal diffusivity measurements were:

1. Irradiated specimen thermal diffusivities were lower than those of the fresh specimens. This was likely related to the hydrogen content change as a result of hydrogen loss during irradiation and the following examination steps. Because initial hydrogen content of initial samples was not available, the amount of hydrogen loss was unclear. In addition, the thermal diffusivity of hydrogen-free irradiated yttrium metal and the effect of defect recombination is unknown.

2. All specimens, except the fresh ones, had similar thermal diffusivities (independent of hydrogen content) at elevated temperatures.

3. PM-prepared specimens that were irradiated at 873 K showed an increase in thermal diffusivity during cooling from 800 °C (1073 K), which could be associated with the redistribution of hydrogen in the samples during measurement which increased the local hydrogen content of the depleted central section with observed contrast variations. PM samples irradiated at target temperatures of 973 and 1073 K did not follow this trend. However, they also did not have the same level of inhomogeneity as the samples shown in Figure 9-2.

4. DH specimens showed no difference in their heating and cooling runs, which is an indication of minimal hydrogen loss during thermal property measurement.

Thermal diffusivities for samples of each capsule were aggregated and fit to a function of the form:

$$\alpha^{-1}\left(\frac{\mathrm{mm}^2}{\mathrm{s}}\right) = A + BT \tag{51}$$

where α is the thermal diffusivity in $\mathrm{mm}^2\,\mathrm{s}^{-1}$ and the temperature scale units are °C. Capsule averaged fitting parameters are summarized in Table 9-10.

Table 9-10: Capsule averaged thermal diffusivities of irradiated samples. Note that the temperature scale units are °C.

Capsule (-)	Type (-)	Target T (K)	A ($1\times10^{-2}\,\mathrm{s\,mm^{-1}}$)	B ($1\times10^{-4}\,\mathrm{{}^\circ C\,s\,mm^{-2}}$)
1	PM	873	2.24	2.397
4	DH	873	2.16	1.676
2B	PM	973	0.68	2.984
5	DH	973	1.70	2.232
3A	PM	1073	1.12	2.647
6	DH	1073	0.65	2.738

DSC measurements The DSC signal of an irradiated YH_2 specimen, 600-4 DSC-5, is shown in Figure 9-24. The main observations are discussed.

DSC signal of fresh YH_2 with hydrogen content close to 2 H/Y units exhibits a smooth monotonically increasing behavior during heating to 1073 K. At this temperature, the rate of hydrogen loss increases, and H/Y ratio decreases (see also hydrogen desorption data [88]). With the start of cooling at 1073 K, the effect of the H/Y ratio is manifested as a sudden decrease in the DSC signal. For the subsequent heating cycle, the same effect is observed as a sudden increase in the DSC signal as well. Furthermore, the peak temperature during a sudden change in the DSC signal is a function of stoichiometry [88]. Thus, the DSC signal, as well as other thermal property measurement techniques, contain signatures related to the hydrogen content. This observation emphasizes the importance of careful use of YH_2 thermal property data in fuel performance codes. Figure 9-24 depicts the DSC data of DH specimens irradiated at target temperature of 873 K. DSC signal consistently showed the effect of the hydrogen loss from YH_2 through shift on local peak temperatures where sudden change occurs, as described above.

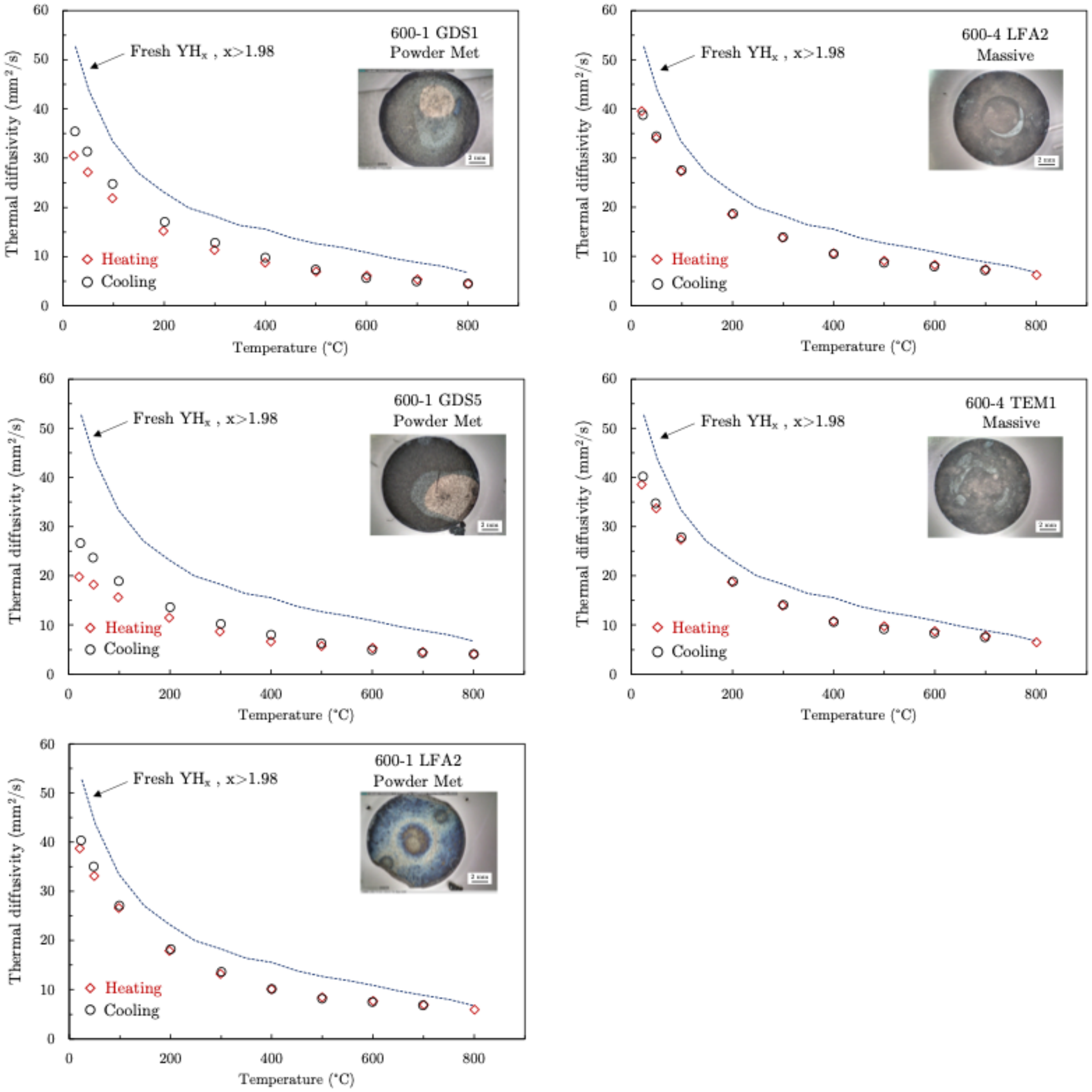

Figure 9-21: Thermal diffusivities of YH_2 specimens irradiated at a target temperature of $873\,\mathrm{K}$. Note that the temperature scale units are $^\circ\mathrm{C}$.

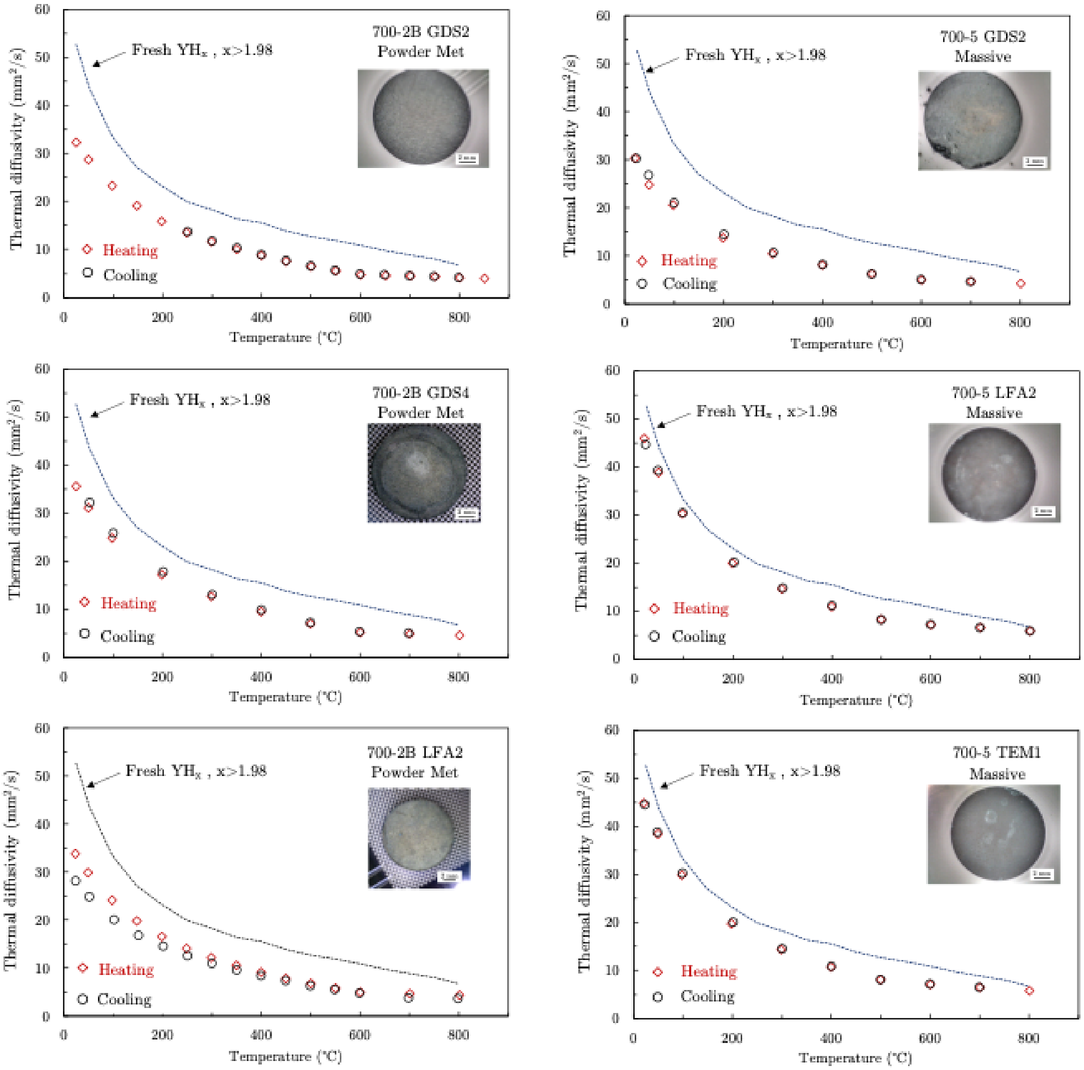

Figure 9-22: Thermal diffusivities of YH_2 specimens irradiated at a target temperature of $973\,\mathrm{K}$. Note that the temperature scale units are $^{\circ}\mathrm{C}$.

Post-irradiation examination of yttrium dihydride irradiated in the Advanced Test Reactor

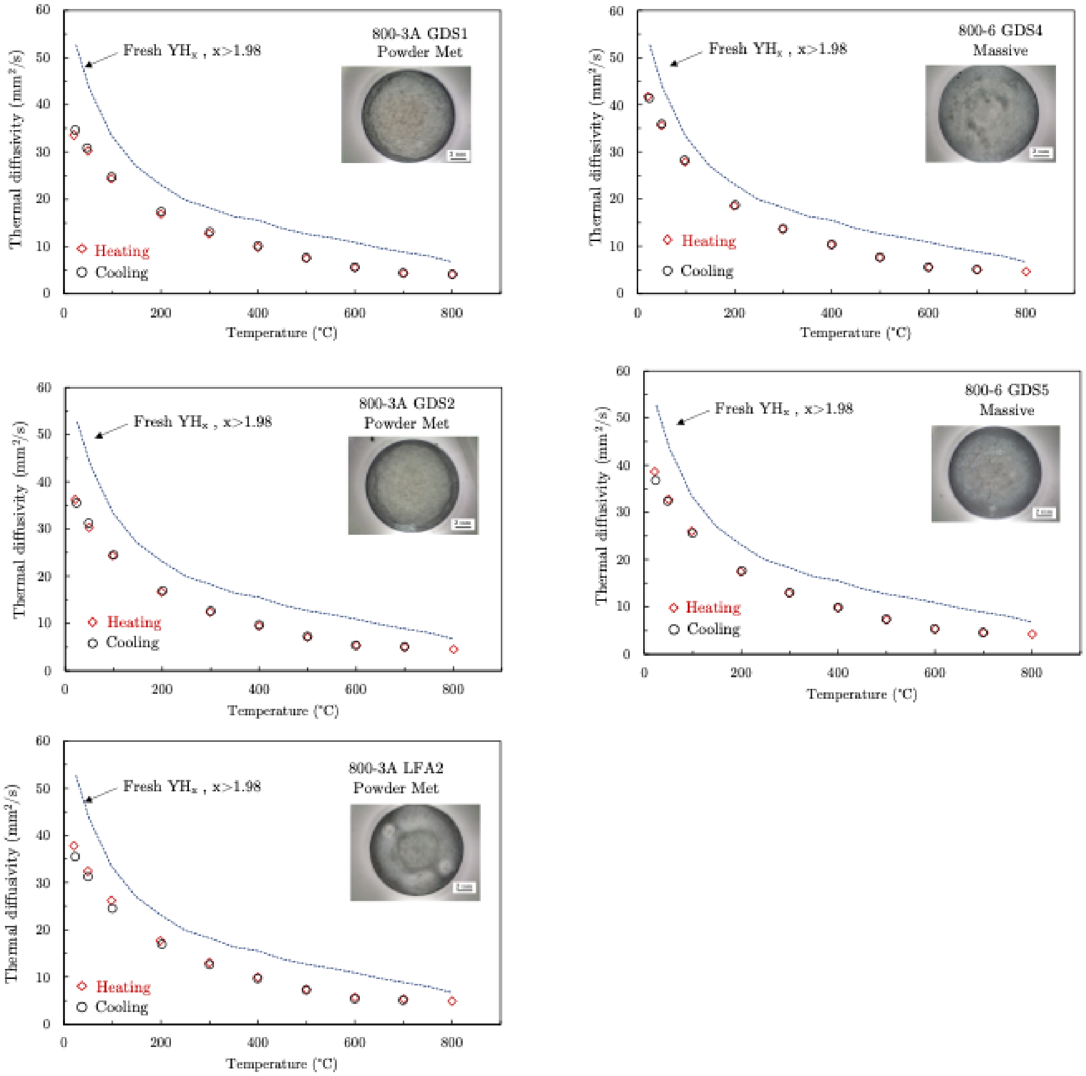

Figure 9-23: Thermal diffusivities of YH_2 specimens irradiated at a target temperature of $1073\,\mathrm{K}$. Note that the temperature scale units are $^{\circ}\mathrm{C}$.

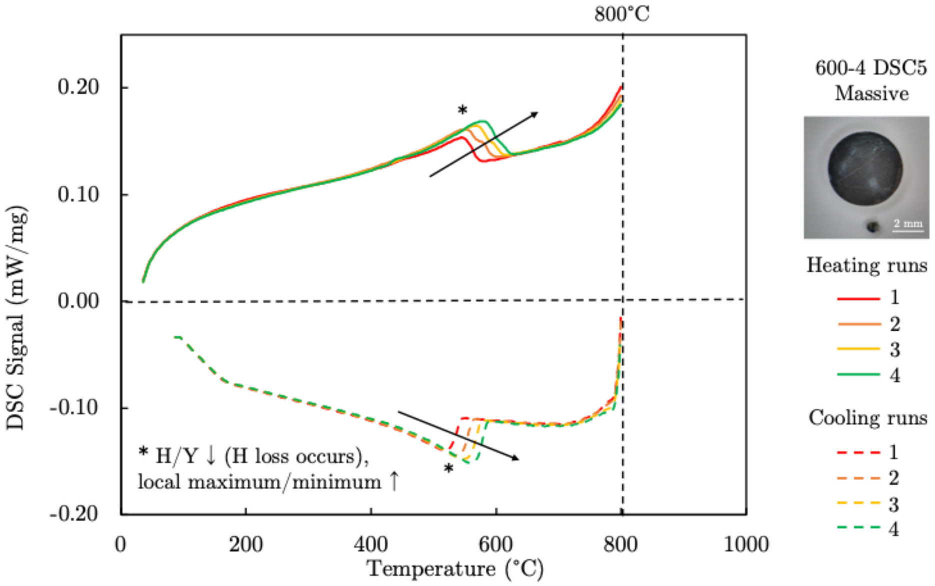

Figure 9-24: A typical DSC signal from irradiated YH_2. Note that the temperature scale units are °C.

9.7 Conclusions of ATR irradiations and future work

PIE activities aim to understand the solid moderator's high-temperature irradiation performance from geometrical stability, mechanical integrity, and predictable behavior perspectives. The behavior of hydrogen in YH_2 was investigated with hydrogen content measurements and XRD. Furthermore, thermal property measurements and metallography were performed to qualitatively investigate the behavior of hydrogen in YH_2. Passive temperature measurements suggested that the capsules targeting irradiation at 973 K (Capsules 2B and 5) experienced temperatures above 1073 K. Thus, only two temperature conditions (873 K and 1073 K) appear to have been met during the ATR irradiation.

Prior to the dismantling of the irradiation assembly, the geometrical stability and mechanical integrity of all hydride specimens was almost preserved with few exceptions, based on the neutron radiography data. Due to the brittle nature of YH_2, some specimens lost their mechanical integrity during specimen retrieval, handling, and transportation.

Neutron radiography also qualitatively revealed hydrogen distribution due to contrast variations. These contrast variations were observed in some samples with optical and electron microscopy where the grain morphology abruptly changes. However, comparison of these samples with images of as-manufactured samples indicated that these features were present in some samples prior to irradiation.

Hydrogen content measurements and XRD results showed fair correlation. However, limited information on the initial stoichiometry of specimens confounded solid conclusions on hydrogen's behavior. Thermal properties of the hydride specimens exhibited signatures of hydrogen loss or re-absorption where the stoichiometry impact was visible. All these methods showed a potential for being a metric to assess irradiated YH_2.

The lack of information on initial hydrogen contents and the lack of knowledge of the initial state of provided hydride samples shows the great importance of detailed sample characterization prior to irradiation. This includes detailed microscopy (optical and SEM/EDS/EBSD of representative samples), phase analysis (e.g., XRD), and hydrogen content measurements (e.g., gravimetry from fabrication, neutron-based methods, vacuum hot extraction, or IGF).

At 873 K, hydrogen is expected to be mostly retained in the dihydride phase, based on results of hydrogen content, XRD, and thermal diffusivity. A potential cladding will provide additional containment at this temperature. At 1073 K, a portion of hydrogen is to be contained in the hydride matrix, but cladding with high hydrogen permeation resistance is needed to extend the operation temperature.

The manufacturing readiness of YH_2 prior to irradiation is critical for qualification of this material and accurate determination of operating conditions. Thus, systematic irradiations that include the essential parameter space, such as time, fluence, temperature, and stoichiometry, are needed to finalize medium technological readiness levels for the use of YH_2 as a moderator.

10 The Hypatia Experiment: yttrium dihydride cross section evaluations

A significant effort is being put forward to determine the material properties and differential cross sections for yttrium dihydride (YH_2). This work also includes creation of $S(\alpha, \beta)$ cross sections for YH_2 in ENDF/B-VIII.0 [48]. The nuclear data pipeline does not end with the evaluation of differential measurements – integral experiments are needed to ensure that the nuclear data evaluations based on physics and differential measurements agree with reality; that is, they predict an accurate result of real systems. Thus, an integral experiment was designed to evaluate the cross section behavior in a critical system. This includes not only absolute k_{eff} values, but also reactivity deltas associated with non-nuclear heating. The designed experiment meets these purposes.

A full description of the Hypatia experiment is given in [50] and briefly summarized here.

10.1 Introduction to the Hypatia experiment

The Hypatia measurement campaign with YH_2 moderators and highly enriched uranium (HEU) was completed in January 2021 at the U.S. Department of Energy's National Criticality Experiments Research Center (NCERC) at the Nevada National Security Site. This measurement campaign provided unique integral measurements based on two experimental configurations and investigated the temperature effects of YH_2 ($H/Y = 1.8$ and 1.9) in a critical reactor system. The Hypatia experiment consisted of a fuel column composed of HEU, 93 wt.% U-235 discs, YH_2 canned in titanium-zirconium-molybdenum (TZM), aluminum oxide heater plates, and other moderator and reflector materials (beryllium, depleted uranium, and graphite) inserted into a thick beryllium reflector. Thermal and neutronic calculations predicted that YH_2 is a unique material that can exhibit a positive temperature coefficient of reactivity (i.e., reactivity can increase as the temperature in the hydride increases). Reactors using YH_2 should account for this unique feature during design, and the results of the Hypatia experiment significantly aid that process.

10.2 Experiment design

The Hypatia experiment was designed to test YH_2 as a primary component of a critical test, rather than as an add-on. The purpose of this was to provide an experiment for future code and nuclear data validation and to specifically evaluate the positive temperature moderator coefficient of YH_2. This was a proof-of-principle experiment and, as such, used primarily existing components, including fuel, moderators, and reflectors. The experiment was designed to be performed using the Planet vertical lift critical assembly machine. Additional components were fabricated for the test, including electric heaters, YH_2 moderator, graphite resistance temperature detector (RTD) plates, and an aluminum guide tube. Experimental configurations varied the amount of hydride moderator to evaluate the effect of the hydride temperature coefficient as a function of the HEU temperature coefficient. The experiment was predicted and validated using the Monte-Carlo N-Particle (MCNP) transport code MCNP6.1®[214].[1]

---

[1] MCNP®and Monte®Carlo N-Particle are registered trademarks owned by Triad National Security, LLC, manager and operator of LANL. Any third party use of such registered marks should be properly attributed to Triad National Security, LLC, including the use of the designation as appropriate. For the purposes of visual clarity, the registered trademark symbol is assumed for all references to MCNP within the remainder of this document.

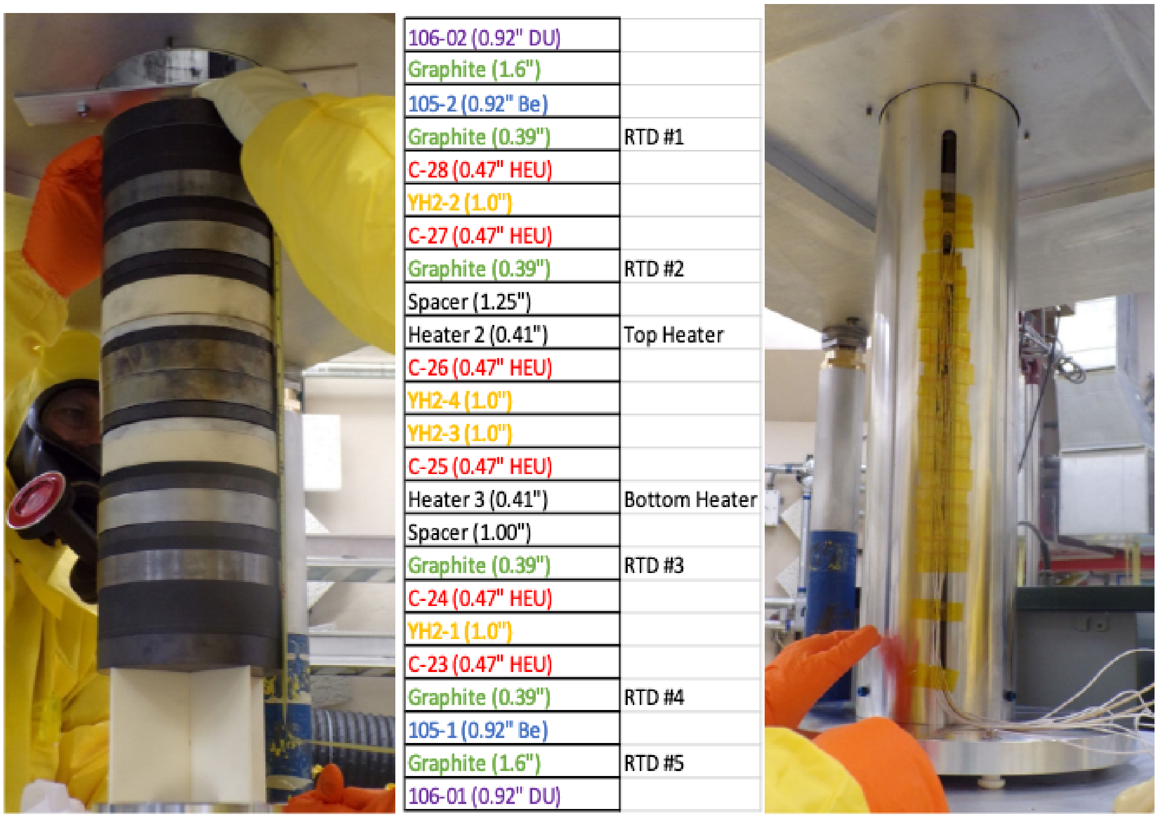

106-02 (0.92" DU)	
Graphite (1.6")	
105-2 (0.92" Be)	
Graphite (0.39")	RTD #1
C-28 (0.47" HEU)	
YH2-2 (1.0")	
C-27 (0.47" HEU)	
Graphite (0.39")	RTD #2
Spacer (1.25")	
Heater 2 (0.41")	Top Heater
C-26 (0.47" HEU)	
YH2-4 (1.0")	
YH2-3 (1.0")	
C-25 (0.47" HEU)	
Heater 3 (0.41")	Bottom Heater
Spacer (1.00")	
Graphite (0.39")	RTD #3
C-24 (0.47" HEU)	
YH2-1 (1.0")	
C-23 (0.47" HEU)	
Graphite (0.39")	RTD #4
105-1 (0.92" Be)	
Graphite (1.6")	RTD #5
106-01 (0.92" DU)	

Figure 10-1: Configuration 1 core column diagrams. The left figure shows the core column before heater controller and RTDs were installed. The middle figure shows the stacking order of components. The right figure shows the core column with the aluminum guide tube. Figure and caption from [50].

A series of approximately 15.24 cm diameter plates were stacked in a column and surrounded by a radial and axial beryllium reflector. The experiment was comprised of two configurations. In Configuration 1, four YH_2 containers were placed in the column alternating with the RTDs, and six different temperature-reactivity measurements were made. In Configuration 2, two containers of YH_2 were placed in the fuel column with the same number of temperature-reactivity measurements. These two configurations enable a comparison of the neutronic effects from the YH_2 components versus other components. Configuration 1 is shown in Figure 10-1, while Configuration 2 is shown in Figure 10-2.

For these experiments, the fuel column was maintained and controlled using an aluminum guide tube that ensured smooth insertion of the column into the assembly. The guide tube also ensured that components did not move during insertion and removal from the assembly. The fuel column mated to the beryllium reflector using graphite corner pieces.

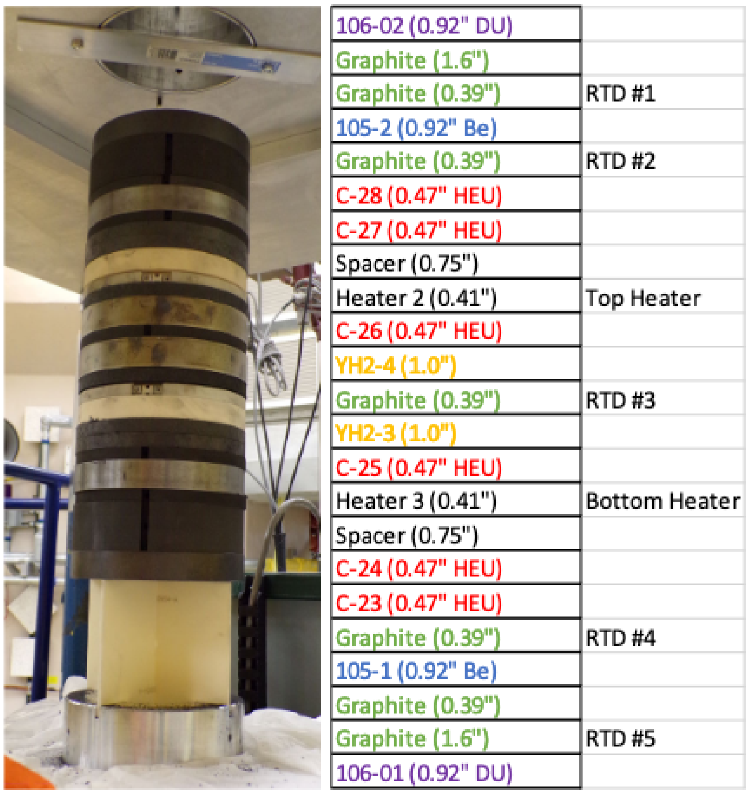

106-02 (0.92" DU)	
Graphite (1.6")	
Graphite (0.39")	RTD #1
105-2 (0.92" Be)	
Graphite (0.39")	RTD #2
C-28 (0.47" HEU)	
C-27 (0.47" HEU)	
Spacer (0.75")	
Heater 2 (0.41")	Top Heater
C-26 (0.47" HEU)	
YH2-4 (1.0")	
Graphite (0.39")	RTD #3
YH2-3 (1.0")	
C-25 (0.47" HEU)	
Heater 3 (0.41")	Bottom Heater
Spacer (0.75")	
C-24 (0.47" HEU)	
C-23 (0.47" HEU)	
Graphite (0.39")	RTD #4
105-1 (0.92" Be)	
Graphite (0.39")	
Graphite (1.6")	RTD #5
106-01 (0.92" DU)	

Figure 10-2: Configuration 2 core column diagrams. The left shows the core column before the heater controller and RTDs were installed. The component stacking order is shown on the right. Figure and caption from [50].

10.2.1 Fuel components

The fuel components consisted of six unalloyed HEU metal discs called C-discs. These C-discs were unclad. The dimensions and masses of these discs are given in Table 10-1.

Table 10-1: C-disc HEU component summary. The extended number of significant figures is given to enable others to model these results using transport codes. Table and caption modified from [50].

C-disc ID (-)	Diameter (cm)	Thickness (cm)	Mass (g)	Density ($\mathrm{g\,cm^{-3}}$)
C23	15.088	1.179	3920.6	18.607
C24	15.090	1.186	3922.3	18.489
C25	15.088	1.191	3926.1	18.434
C26	15.088	1.179	3923.9	18.622
C27	15.088	1.189	3930.5	18.494
C28	15.088	1.181	3917.3	18.551

10.2.2 Yttrium dihydride moderator

Hydride moderator components were fabricated in the Sigma Division of Los Alamos National Laboratory (LANL). The method to produce these components was described in [215]. Components were fabricated from Sigma yttrium, which was described in section 9. Using this method, 14 discs of YH_2 were fabricated and assembled in TZM containers in two layers of seven discs, each. These TZM containers were then welded closed. Two containers were fabricated in 2016 and the other two were fabricated in 2020. The discs fabricated in 2020 had hydrogen contents ranging between 1.8 and 1.9 H/Y units, while the components made in 2016 were not as well characterized; for the purposes of this experiment, they were assumed to be 1.9 H/Y units, though this could not be confirmed. An example of such a TZM container is shown in Figure 10-3. In the newer TZM containers, aluminum spacers were used to ensure no movement of the hydride components, while in the older TZM containers, anti-rotation pins were welded for the same purpose [215].

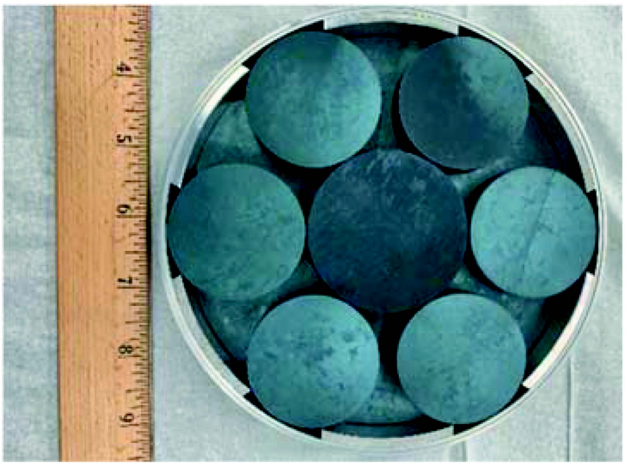

Figure 10-3: Yttrium dihydride discs within the TZM container before sealing. Figure and caption from [50].

10.2.3 Other components

Heaters Heaters used nichrome heating elements surrounded by aluminum(III) oxide. Heating was achieved up to 603 K to prevent degradation of the unalloyed HEU C-discs. Heaters were covered with aluminum(III) oxide plates.

Graphite RTD plates Graphite discs with slots for RTS were used to moderate neutron energy, help achieve a critical configuration, and provide locations for RTS to measure temperature. Discs were prepared from Grade 2114 nuclear graphite.

Spacers Aluminum(III) oxide spacers were added in certain locations as reactivity (criticality) control mechanisms. As predictions of criticality are not always accurate, a mechanism to change the distance between HEU plates during the experiment by increasing or decreasing the reactivity statistically with manual configuration changes was needed. Slightly different thicknesses of axial spacer plates served this purpose.

Aluminum guide tube An aluminum metal guide tube was fabricated for this experiment. The purpose of this component was to ensure smooth insertion of the core into the critical assembly and to ensure that experimental components did not move during raising and lowering of the platen.

Graphite corner pieces The cylindrical fuel column was mated to the rectangular reflector blocks using graphite corner pieces. These components were also fabricated using Grade 2114 nuclear graphite.

Radial reflectors Beryllium reflector components were made from existing beryllium parts at NCERC in a rectangular geometry.

Axial reflectors Additional beryllium and depleted uranium (DU) discs were also used as axial reflectors, with the DU discs placed on the axis ends. Axial reflectors ensured reactivity in the assembly for a critical configuration. Beryllium discs were placed inside depleted uranium discs.

Aluminum shroud The beryllium reflector was attached to an aluminum shroud, which minimized gaps between the beryllium reflector components and ensured no movement of the beryllium components during the experiment.

Table 10-2 summarizes all the materials used with dimensions and densities which were incorporated into the MCNP model. The MCNP model for Configuration 1 is shown in Figure 10-4(a), a schematic of the beryllium reflector is shown in Figure 10-4(b), and a schematic of the full assembly is shown in Figure 10-4(c).

Table 10-2: Summary of components, chemistries, and geometries used in the Hypatia experiment. Note that length and width are replaced by diameter for cylindrical components. Hydrogen content of outer moderator components is assumed. The composition of TZM is Mo-0.5%Ti-0.08%Zr-0.03%C. Note that the Al guide tube contains a $60.325\,\mathrm{cm} \times 1.524\,\mathrm{cm}$ slot. Table and caption modified from [50].

Component (-)	Chemistry (-)	Length (cm)	Width (cm)	Height/Thickness (cm)	Density ($\mathrm{g\,cm^{-3}}$)
Fuel		See Table 10-1			
Central moderator	$YH_{1.80\text{-}1.90}$	5.6134		1.219	3.7
Outer moderator	$YH_{1.90}$	4.5466		1.219	3.7
Moderator container	TZM	OD: 14.8082, ID: 14.7066		2.5396	10.23 [216]
Heater	Al_2O_3	14.859		1.041	3.8
RTD plate #1-4	Graphite 2114	15.240		1.000	1.81
RTD plate #5	Graphite 2114	15.240		4.000	1.81
Beryllium reflector disc	Be	15.062		2.337	1.85
dU reflector disc	DU	15.062		2.337	17
Al guide tube	Al 6061	OD: 15.240, ID: 15.494		127	2.7
Corner piece	Graphite 2114	Outer side length: 17, ID: 16.137		25.781	1.81
Reflector #1	Be	40.64	7.620	0.635	1.85
Reflector #2	Be	40.64	7.620	2.527	1.85
Reflector #3	Be	40.64	7.620	7.620	1.85
Shroud	Al 6061	-	-	-	2.7
Spacer	Al_2O_3	Variable, see Figures 10-1 and 10-2			0.2632

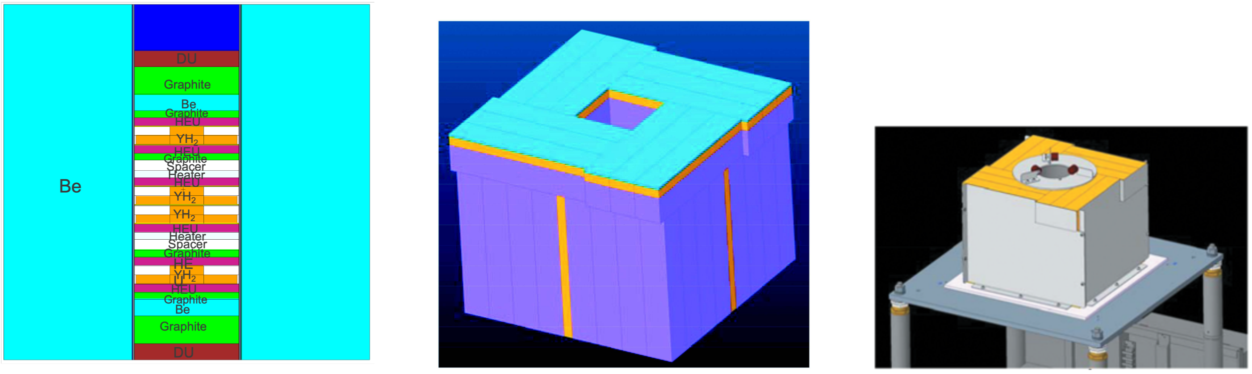

(a) (b) (c)

Figure 10-4: Component mating and geometries for the Hypatia experiment. (a) MCNP model of Configuration 1. (b) Schematic of the beryllium reflector parts. Note that each color is a different type, as given in Table 10-2. (c) Schematic of the full experimental assembly with the aluminum shroud. Figure and caption modified from [50].

10.3 Critical experiment methods

The purpose of the Hypatia experiment was to understand the temperature coefficients of YH_2 by varying the hydride:fuel ratio, as these are the two dominant components affecting reactivity change with temperature.

Approach to criticality MCNP was used to determine an approximate critical configuration at room temperature by using different spacer thicknesses. These different spacer thicknesses changed the value of k_{eff}. A $1/M$ method was used to approach criticality, where M is the subcritical multiplication factor. This is done by plotting neutron detector count rates as a function of configuration and extrapolating $1/\mathrm{M}$ to zero ($k_{\text{eff}} = 1$). The closer the configurations are to criticality, the more accurate the extrapolation is. A more detailed explanation of the approach to criticality method is given elsewhere [217]. Here, ^{252}Cf was used as an external source.

Measurements at temperature Once a critical configuration for a particular spacer thickness was determined, all the heating and instrumentation were installed. Excess reactivity was then measured again with the instrumentation in place. The core was removed from the reflector and the temperature was ramped at approximately $2\,\mathrm{K\,min^{-1}}$ in both heaters until the desired temperature was reached (in $50\,\mathrm{K}$ increments). Once the desired temperature was achieved, the column was held at isothermal conditions for $30\,\mathrm{min}$ to stabilize temperature. The heated column was then re-inserted into the reflector with the heaters still on. The system was maintained in a critical configuration until sufficient power was achieved to measure the reactor period (i.e., the amount of time required for power to increase by a factor of e). Reactor period was measured using compensated ion chambers (linear channels, LCs) for medium/high power measurement and ^{3}He tubes wrapped in polyethylene for low power measurements (startup detectors, SU). The data from these detectors was plotted and fit to determine an approximate reactor period. After measurements were made, the column was removed from the reflector and the process was repeated for the next target temperature. The full temperature and neutron count rate as a function of time for Configurations 1 and 2 are shown in Figures 10-5 and 10-6, respectively.

The Hypatia Experiment: yttrium dihydride cross section evaluations

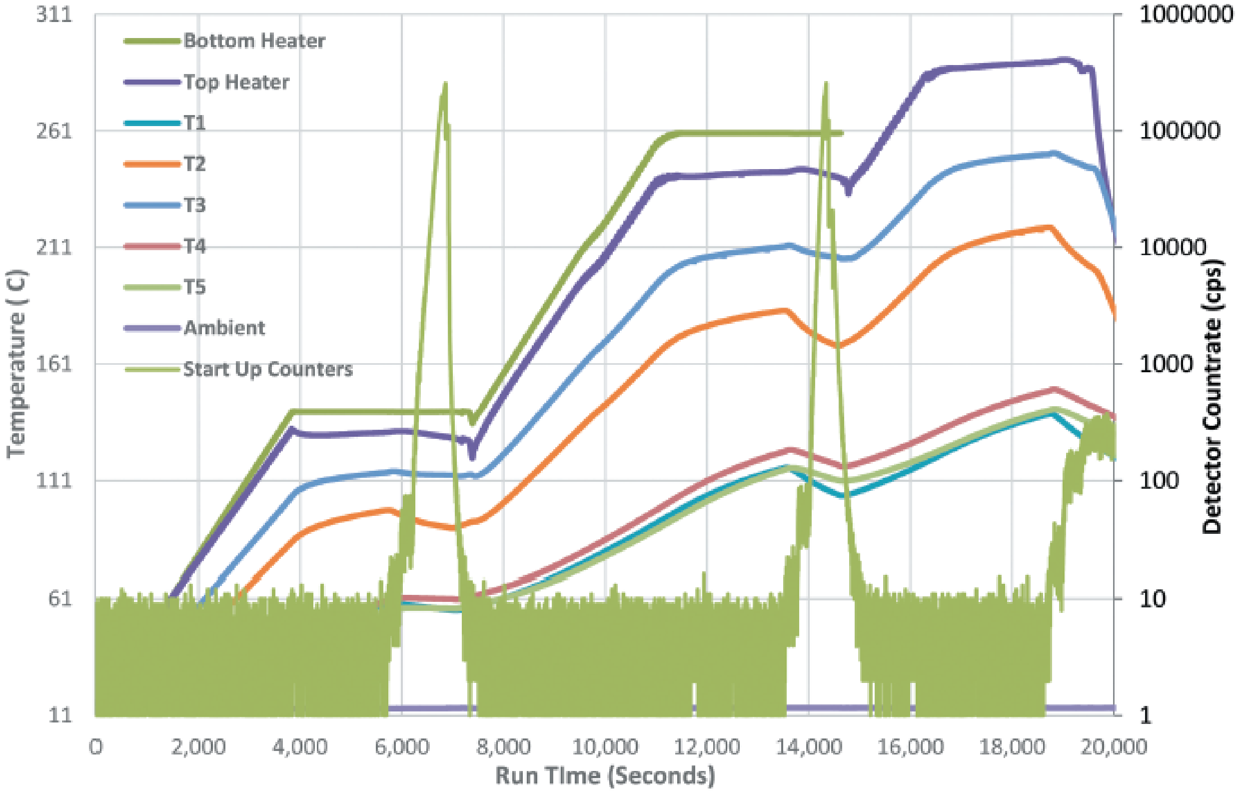

Figure 10-5: Full temperature and neutron detector count rate as a function of time for Configuration 1. Temperature is plotted on the left axis and neutron count rate is plotted on the right axis. Neutron power level is shown for startup counters. Figure and caption from [50].

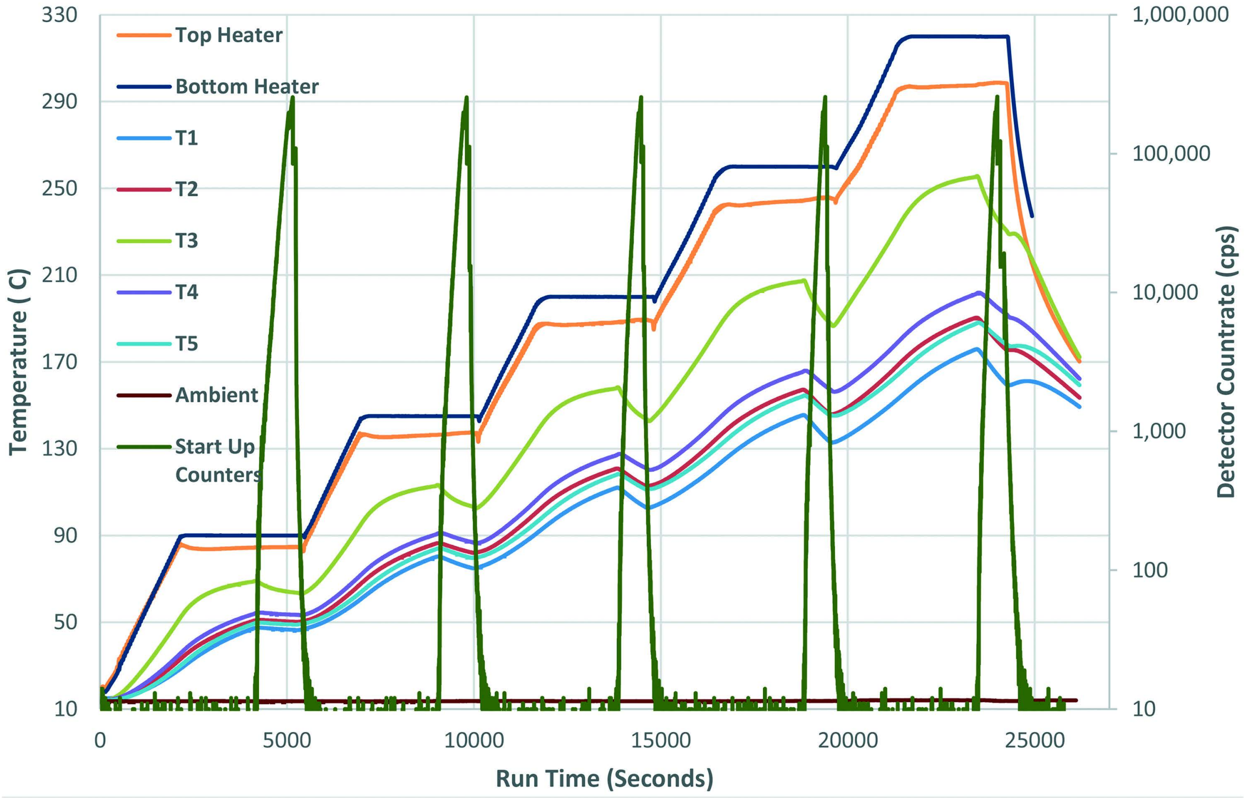

Figure 10-6: Full temperature and neutron detector count rate as a function of time for Configuration 2. Temperature is plotted on the left axis and neutron count rate is plotted on the right axis. Neutron power level is shown for startup counters. Figure and caption from [50].

10.4 Modeling approach

Aside from the neutronic effects of the system, the thermal and mechanical response were determined to be important to the experiment. In particular, the neutronic effects of YH_2 could not be accurately predicted until the exact temperature of each component was calculated, as RTDs were not present on each experimental component. As such, MCNP and Abaqus [218] models were developed to study these effects.

Neutronics model The Hypatia experiment was modeled in MCNP using the component geometries and compositions given in Table 10-2 in the configurations shown in Figure 10-4. The resulting simulations predicted excess reactivity with varying hydrogen content, temperature, spacer thickness, and separation distances and provided validation of cross sections with experimental data. Excess reactivities were calculated using cross sections from ENDF/B-VIII.0 for yttrium and hydrogen, as well as $S(\alpha, \beta)$ cross sections for each tested temperature for sub-stoichiometric YH_2 [5, 48]. Results using the newly generated cross sections were comparable to those calculated using standard cross-sections for YH_2.

Thermomechanical model A 3D model of the experiment was created to correlate YH_2 temperature with reactivity. This model was rendered in an unstructured mesh using Abaqus finite element analysis (FEA). All cylindrical components were modeled as perfect cylinders, but surface irregularities were modeled as degraded surface contact conductivities. In this model, the highest mesh resolution was applied to the moderator components. The model also accounts for heater temperature changes and the motion of the system in and out of the reflector. The geometry of the model is described in Figure 10-7, which shows (a) the unstructured mesh and (b) the FEA-calculated temperature distribution with cutout of moderator component temperature distributions. The temperatures of each moderator disc were calculated as the volume-averaged temperature to account for thermal gradients. Because there was no temperature measurement instrumentation in direct contact with the moderator elements, moderator temperatures were inferred by comparing the temperatures of instrumented components with their FEA-calculated values. Thus, temperature values for the five RTD components in the column were compared with volume-averaged, calculated values for those same components in the Abaqus model. Comparison was performed as a function of time and RTD temperature error was projected as an uncertainty range for the nearest moderator component. This was done for both Configuration 1 and 2.

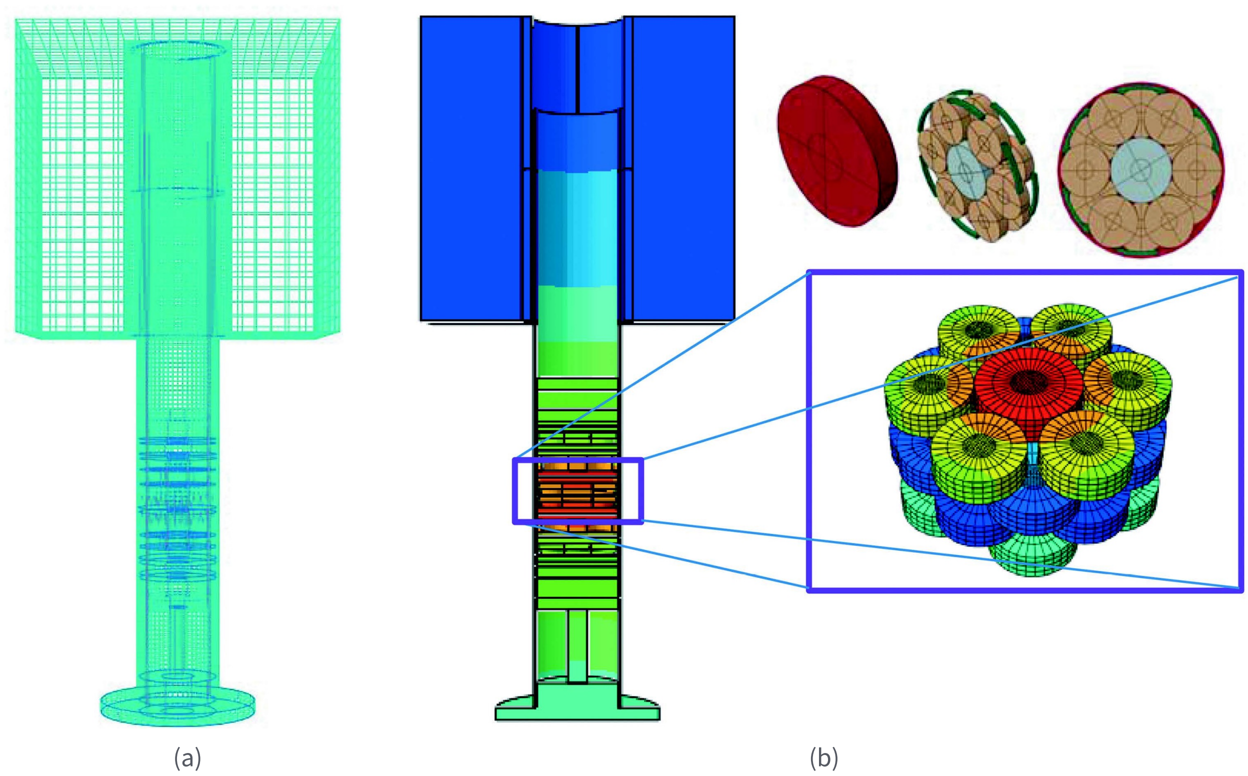

Figure 10-7: (a) Abaqus unstructured mesh. (b) FEA-calculated temperature distribution with a cutout of the temperature distribution for moderator elements. Geometry, mesh structure, and thermal contour resolution are demonstrated here, hence temperature map and times are not provided. Figure and caption from [50].

10.4.1 Comparative Analysis

Configuration 2 It was determined that the movement of the column in and out of the reflector changed the nuclear reactions and temperatures as a function of time, thus changing the thermal response of the system. This effect is observed in Figures 10-5 and 10-6 at the end of each isothermal hold, when the column was removed from the reflector; this is evident as changes in the neutron count rate and decreases in component temperature even though the top and bottom heater temperatures increase. To account for this, a step function velocity of the system into and out of the reflector was implemented. The simulated results for the volume-averaged RTD temperatures as functions of time for Configuration 2 are shown in Figure 10-8.

The thermal-displacement model results were nearly identical to the effects seen in RTD-3 in Configuration 2. RTD-3 was placed between the two moderator components and, thus, was ideally positioned for quantifying the uncertainties in YH_2 temperature estimates. The largest difference in simulated and measured temperatures was calculated to be 5%. Thus, a conservative 5% uncertainty range was uniformly applied for all temperature estimates in Configuration 2.

Configuration 1 The simulated results for the volume-averaged RTD temperatures as functions of time for Configuration 1 are shown in Figure 10-9. As shown in Figure 10-1, there were no RTDs in direct contact with any moderator elements. As such, characterization of moderator element temperature uncertainty was not as straightforward as it was for Configuration 2. Thus, all RTDs were analyzed for error calculation and representative moderator element temperatures were determined from the FEA simulations. The maximum temperature deviation for Configuration 1 was determined to be 20%, which was assigned as the uncertainty range for all moderator element temperatures.

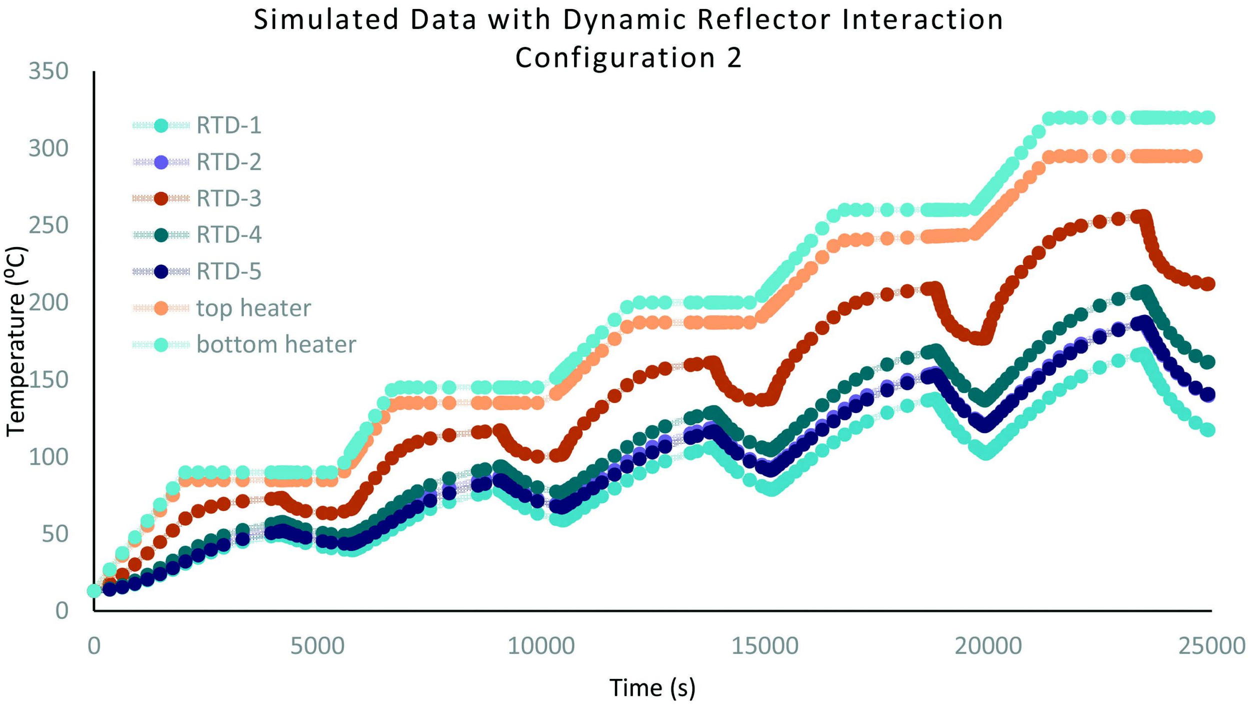

Figure 10-8: Simulated time-dependent RTD temperature values for Configuration 2. Figure and caption from [50].

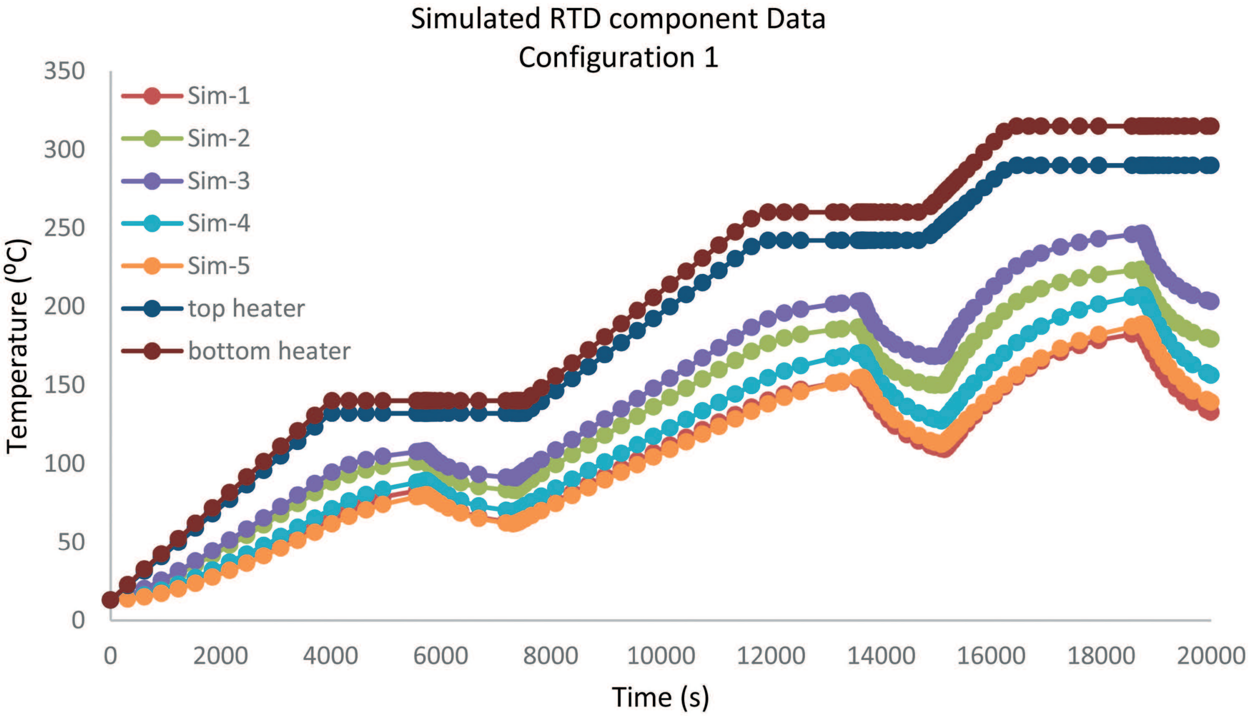

Figure 10-9: Simulated time-dependent RTD temperature values for Configuration 1. Figure and caption from [50].

10.5 Measured and simulated reactivity changes

Reactivity calculation from experimental data Reactivity (ρ) in units of cents (¢) was calculated from the Inhour equation using the reactor period

$$\rho(\$) = \frac{1}{\beta_{\text{eff}} T} + \sum_{i=1}^{6} \frac{\beta_i/\beta_{\text{eff}}}{1+\lambda_i T} \tag{52}$$

where β_{eff} is the effective delayed neutron fraction, β_i is the delayed neutron fraction for group i, and λ_i is the decay constant for delayed neutron group i. For the fast neutron system in this experiment, the parameters related to β_{eff} are fast uranium parameters. These are summarized in Table 10-3.

Table 10-3: Inhour equation parameters. Table from [50].

Group index, i (-)	Decay constant, λ_i (s^{-1})	Relative abundance, $a_i = \beta_i/\beta_{\text{eff}}$ (-)
1	0.0127	0.038
2	0.0317	0.213
3	0.115	0.188
4	0.311	0.407
5	1.40	0.128
6	3.87	0.026

For Configuration 1, the critical configuration was found using a 3.175 cm thick spacer in the lower portion of the column and a 2.54 cm thick spacer in the upper portion. At a temperature of 287 K, the reactor period was measured to be 238 s. From the SU neutron detectors, the reactivity was determined to be 5 ¢with a count rate of 1×10^4 counts per second (cps).

For Configuration 2, the critical configuration was found using two 1.905 cm thick spacers in the lower and upper portions of the column. At a temperature of 287 K, the reactor period was measured to be 171 s. From the SU neutron detectors, the reactivity was determined to be approximately 6 ¢with a count rate of 7×10^4 cps.

Comparison between experimental and calculated reactivities Excess reactivities calculated using MCNP were compared with those calculated using the Inhour equation for each temperature and configuration. The results of this analysis for Configuration 1 are shown in Table 10-4 and for Configuration 2 in Table 10-5. From these values, it is clear that reactivity increased with temperature. This is expected for YH_2, which is known to have a positive reactivity temperature coefficient. However, the measured values appear to be lower than the calculated ones. This could be due to thermal expansion, which will decrease reactivity, but also could be due to thermal gradient effects. More detailed analyses are underway to understand the effects of these phenomena.

Table 10-4: MCNP calculated reactivity compared with SU measured reactivity for Configuration 1. Table and caption modified from [50].

Heater temperature (K	MCNP k_{eff} (-)	MCNP reactivity change (¢)	SU measured reactivity change (¢)
286	0.99852	-	-
358	0.99895	2.9	3.2
413	0.99922	7.1	6.7
473	0.9995	11.1	11.4
533	0.99959	16.0	13.1
583	1.00016	18.1	18.4

Table 10-5: MCNP calculated reactivity compared with SU measured reactivity for Configuration 2. Table and caption from [50].

Heater temperature (K	MCNP k_{eff} (-)	MCNP reactivity change (¢)	SU measured reactivity change (¢)
286	0.99621	-	-
358	0.99625	2.1	1.5
408	0.9968	3.7	3.5
460	0.99706	4.9	5.2
515	0.9974	6.3	6.5
568	0.99716	7.4	7.5

10.6 Conclusions of the Hypatia experiment

A critical experiment to study temperature effects on the reactivity of YH_2 was performed at the NCERC. These experiments used HEU and YH_2 fuel and moderator components, respectively, with electric heaters to reduce competing effects from nuclear heating. Measurements of reactivity change as a function of temperature for two different fuel column configurations showed that the positive reactivity temperature coefficient appears to be less than the calculated values using simulated cross sections. This result still needs to be assessed in higher-fidelity multiphysics models to include expansion of the materials in the system and other effects.

11 Conclusions

From the numerous studies cited in this document, it is clear that a better understanding of yttrium and zirconium hydride performance is desired to implement this material in advanced reactors, including microreactors. The key highlights of this Handbook are summarized below.

Yttrium and zirconium hydrides were studied extensively in the past, including through the Aircraft Nuclear Propulsion and prior Space Nuclear programs. The thermodynamics of hydride stability and fabrication methods were developed. More recently, fabrication methods have been recaptured at a variety of US national laboratories, including Los Alamos and Oak Ridge. However, domestic supplies of high-purity yttrium and zirconium with low oxygen and very low neutron poison compositions are needed to produce YH and ZrH at the scale and purity required for reactor applications.

Thermodynamic properties across the literature must be studied in more detail, as there exists considerable spread in the pressure-composition-temperature (PCT) curves for the yttrium-hydrogen system. Zirconium hydride PCT curves have not been measured at pressures greater than 1 atm, which makes predicting performance in cladding at elevated temperature difficult. PCT curves are used to calculate thermodynamic properties and have been used to calculate hydrogen dynamic effects at temperature. As such, more accurate and well-characterized thermodynamic measurements are needed. The kinetics of phase formation, transformation, hydrogen absorption and desorption, and hydrogen diffusion are also severely lacking in the temperature ranges of interest and represent a research need.

The physical and mechanical properties of YH and ZrH are very well characterized for near-stoichiometric compositions. However, characterization of the evolution of these properties as a function of hydrogen content and temperature is needed to understand thermal performance as hydrogen is lost from the material at elevated temperature. To that end, more studies at elevated temperatures and under hydrogen partial pressure environments are needed to eliminate the effects of hydrogen content change during elevated temperature measurements.

YH_2 that was irradiated in the Advanced Test Reactor was characterized for specimen integrity, microstructure, phase evolution, and thermophysical properties as a function of irradiation temperature. Samples were prepared using two different methods: powder metallurgy and direct hydriding. The direct hydride materials performed in a manner as might be expected: that is, at lower temperatures, hydrogen loss appeared to occur at the surface. This was also observed in powder metallurgy samples; however, some samples were not produced to high quality, which makes comparison between as-fabricated and post-irradiated states difficult. Thermal diffusivity measurements showed that irradiated materials generally had lower diffusivities than as-fabricated materials. However, the irradiated powder metallurgy specimens appeared to recover thermal diffusivity upon thermal cycling, while direct hydride materials did not; this was related to the internal porosity of the powder metallurgy materials. More work is required to understand these phenomena.

YH_2 was also studied in a critical experiment at the National Criticality Experiments Research Center to evaluate cross sections of this material and provide validation of those cross sections as a function of temperature, and to determine the positive reactivity temperature coefficient of this material. Two different configurations of moderator elements provided different fuel-to-moderator ratios. Results showed that the measured reactivity changes with temperature were less than those predicted using Monte-Carlo N-Particle (MCNP) transport code calculations. It was hypothesized that this result could be due to thermal expansion

Overall, this body of work shows that significant progress has been made towards the qualification of YH and ZrH as moderator materials. More studies of engineering-scale components, such as the Hypatia experiment and ATR irradiation, are required to better understand moderator performance parameters that will feed into multiphysics codes to more accurately predict in-reactor moderator performance. Irradiations of both hydrides inside cladding at microreactor operating temperatures are needed. To that end, hydrogen dynamics at temperature and under irradiation represent a significant knowledge gap that must be addressed.

References

[1] Aditya Prahlad Shivprasad et al. *Advanced Moderator Material Handbook*. Tech. rep. Los Alamos National Lab.(LANL), Los Alamos, NM (United States), 2020.

[2] Aditya Prahlad Shivprasad et al. *Advanced Moderator Material Handbook (FY22 Version: Revision 2)*. Tech. rep. LA-UR-22-30557. Los Alamos National Lab.(LANL), Los Alamos, NM (United States), 2022.

[3] A.P. Shivprasad et al. *Advanced Moderator Materials Handbook (FY23 Version)*. English. Tech. rep. LA-UR–23-30491. Los Alamos National Laboratory, 2023. DOI: `10.2172/2204161`. URL: `https://www.osti.gov/biblio/2204161`.

[4] David I Poston et al. "Results of the KRUSTY nuclear system test". In: *Nuclear and Emerging Technologies for Space, American Nuclear Society Topical Meeting*. Richland, WA: American Nuclear Society, Feb. 2019.

[5] David A Brown et al. "ENDF/B-VIII. 0: the 8th major release of the nuclear reaction data library with CIELO-project cross sections, new standards and thermal scattering data". In: *Nuclear Data Sheets* 148 (2018). Publisher: Elsevier, pp. 1–142. ISSN: 0090-3752.

[6] A. P. Shivprasad et al. "Elastic moduli of high-density, sintered monoliths of yttrium dihydride". en. In: *Journal of Alloys and Compounds* 826 (June 2020), p. 153955. ISSN: 0925-8388. DOI: `10.1016/j.jallcom.2020.153955`. URL: `http://www.sciencedirect.com/science/article/pii/S0925838820303182`.

[7] Robert Durgin Rockwell. "Investigation of the Topaz-II space nuclear reactor moderator thermal transient". PhD thesis. Massachusetts Institute of Technology, 1993.

[8] CE Johnson and CA Goetz. "SNAP 8 reactor and shield". In: *AIAA Journal* 1.10 (1963), pp. 2355–2361.

[9] J. P. Hawley and R. A. Johnson. *SNAP 10A FS-3 reactor performance*. English. Tech. rep. NAA-SR-11397. Atomics International Div., Canoga Park, CA (USA), Aug. 1966. DOI: `10.2172/7315563`. URL: `https://www.osti.gov/biblio/7315563`.

[10] Helmuth Boeck and Mario Villa. *TRIGA reactor characteristics*. Tech. rep. Vienna University of Technology, 2007.

[11] R. Van Houten. "Selected engineering and fabrication aspects of nuclear metal hydrides (Li, Ti, Zr, and Y)". en. In: *Nuclear Engineering and Design* 31.3 (Jan. 1974), pp. 434–448. ISSN: 0029-5493. DOI: `10.1016/0029-5493(75)90178-8`. URL: `http://www.sciencedirect.com/science/article/pii/0029549375901788`.

[12] P. Sabharwall et al. "Nonnuclear Experimental Capabilities to Support Design, Development, and Demonstration of Microreactors". In: *Nuclear Technology* (June 2022). Publisher: Taylor & Francis, pp. 1–19. ISSN: 0029-5450. DOI: `10.1080/00295450.2022.2043087`. URL: `https://doi.org/10.1080/00295450.2022.2043087`.

[13] Xunxiang Hu, Chinthaka Silva, and Kurt A Terrani. "Development of Yttrium Hydride Moderator for the Transformational Challenge Reactor". In: *Transactions of the American Nuclear Society* 122.1 (2020).

[14] Robert Van Houten. "Hydriding Process". 3,720,751 (Cincinnati, OH). Mar. 1973.

References

[15] ASTM E1447-09. "Standard Test Method for Determination of Hydrogen in Titanium and Titanium Alloys by Inert Gas Fusion Thermal Conductivity/Infrared Detection Method". In: (2009). Publisher: ASTM International West Conshohocken, PA.

[16] M. Grosse et al. "Quantification of hydrogen uptake of steam-oxidized zirconium alloys by means of neutron radiography". en. In: *Journal of Physics: Condensed Matter* 20.10 (Feb. 2008). Publisher: IOP Publishing, p. 104263. ISSN: 0953-8984. DOI: `10.1088/0953-8984/20/10/104263`.

[17] H. Sakaguchi et al. "Visualization of hydrogen in hydrogen storage alloys using neutron radiography". en. In: *International Journal of Hydrogen Energy* 25.12 (Dec. 2000), pp. 1205–1208. ISSN: 0360-3199. DOI: `10.1016/S0360-3199(00)00031-8`. URL: `http://www.sciencedirect.com/science/article/pii/S0360319900000318`.

[18] Rick L. Paul. "Hydrogen Measurement by Prompt Gamma-ray Activation Analysis: A Review". en. In: *Analyst* 122.3 (Jan. 1997). Publisher: The Royal Society of Chemistry, 35R–41R. ISSN: 1364-5528. DOI: `10.1039/A606419A`. URL: `https://pubs.rsc.org/en/content/articlelanding/1997/an/a606419a`.

[19] Adrien Couet et al. "Cold neutron prompt gamma activation analysis, a non-destructive technique for hydrogen level assessment in zirconium alloys". en. In: *Journal of Nuclear Materials*. Microstructure Properties of Irradiated Materials 425.1 (June 2012), pp. 211–217. ISSN: 0022-3115. DOI: `10.1016/j.jnucmat.2011.06.044`. URL: `http://www.sciencedirect.com/science/article/pii/S0022311511006398`.

[20] Zi-Kui Liu. "First-Principles Calculations and CALPHAD Modeling of Thermodynamics". en. In: *Journal of Phase Equilibria and Diffusion* 30.5 (Sept. 2009), p. 517. ISSN: 1863-7345. DOI: `10.1007/s11669-009-9570-6`. URL: `https://doi.org/10.1007/s11669-009-9570-6`.

[21] C. E. Lundin and J. P. Blackledge. "Pressure-Temperature-Composition Relationships of the Yttrium-Hydrogen System". en. In: *Journal of The Electrochemical Society* 109.9 (Sept. 1962), pp. 838–842. ISSN: 0013-4651, 1945-7111. DOI: `10.1149/1.2425565`. URL: `http://jes.ecsdl.org/content/109/9/838`.

[22] D. Khatamian et al. "Crystal structure of YD1.96 and YH1.98 by neutron diffraction". In: *Physical Review B* 21.6 (Mar. 1980), pp. 2622–2624. DOI: `10.1103/PhysRevB.21.2622`. URL: `https://link.aps.org/doi/10.1103/PhysRevB.21.2622`.

[23] D.S. Parker. *Properties of hydrided yttrium.* Tech. rep. USAEC Report APEX-558. General Electric Company, May 1960.

[24] Daigo Setoyama et al. "Mechanical properties of yttrium hydride". In: *Journal of Alloys and Compounds* 394.1 (May 2005), pp. 207–210. ISSN: 0925-8388. DOI: `10.1016/j.jallcom.2004.10.035`. URL: `http://www.sciencedirect.com/science/article/pii/S0925838804014021`.

[25] A. P. Shivprasad et al. "Thermophysical properties of high-density, sintered monoliths of yttrium dihydride in the range 373–773K". en. In: *Journal of Alloys and Compounds* (Aug. 2020), p. 156303. ISSN: 0925-8388. DOI: `10.1016/j.jallcom.2020.156303`. URL: `http://www.sciencedirect.com/science/article/pii/S0925838820326670`.

[26] Artem A. Trofimov et al. "Thermophysical properties and reversible phase transitions in yttrium hydride". en. In: *Journal of Nuclear Materials* 542 (Dec. 2020), p. 152569. ISSN: 0022-3115. DOI: `10.1016/j.jnucmat.2020.152569`. URL: `https://www.sciencedirect.com/science/article/pii/S0022311520311776`.

[27] J.R. Torres et al. “High-temperature structure, elasticity, and thermal expansion of ε-$ZrH_{1.8}$”. In: *Journal of Nuclear Materials* 603 (0 2025), p. 155437.

[28] Masato Ito et al. “Thermal properties of yttrium hydride”. In: *Journal of Nuclear Materials*. Proceedings of the 11th International Symposium on Thermodynamics of Nuclear Materials 344.1 (Sept. 2005), pp. 295–297. ISSN: 0022-3115. DOI: `10.1016/j.jnucmat.2005.04.058`. URL: `http://www.sciencedirect.com/science/article/pii/S0022311505002412`.

[29] D. L Anderson et al. “Hydrogen locations, diffusion and the electronic density of states in yttrium dihydrides: A nuclear magnetic resonance investigation”. en. In: *Journal of the Less Common Metals* 73.2 (Sept. 1980), pp. 243–251. ISSN: 0022-5088. DOI: `10.1016/0022-5088(80)90309-4`. URL: `http://www.sciencedirect.com/science/article/pii/0022508880903094`.

[30] T. -T. Phua et al. “Paramagnetic impurity effects in nuclear magnetic resonance determinations of hydrogen diffusion and electronic structure in metal hydrides: Cerium in YH2”. en. In: *Journal of the Less Common Metals* 104.1 (Dec. 1984), pp. 105–112. ISSN: 0022-5088. DOI: `10.1016/0022-5088(84)90443-0`. URL: `http://www.sciencedirect.com/science/article/pii/0022508884904430`.

[31] R. Goc et al. “Van Vleck second moments and hydrogen diffusion in YH2.1—measurements and simulations”. en. In: *Solid State Nuclear Magnetic Resonance*. 31st Congress Ampere, Magnetic Resonance and Related Phenomena 25.1 (Jan. 2004), pp. 133–137. ISSN: 0926-2040. DOI: `10.1016/j.ssnmr.2003.03.009`. URL: `https://www.sciencedirect.com/science/article/pii/S092620400300078X`.

[32] C. Korn and S. D. Goren. “NMR study of hydrogen diffusion in zirconium hydride”. In: *Physical Review B* 33.1 (Jan. 1986). Publisher: American Physical Society, pp. 68–78. DOI: `10.1103/PhysRevB.33.68`. URL: `https://link.aps.org/doi/10.1103/PhysRevB.33.68`.

[33] E. Lebsanft, D. Richter, and J. Topler. “Investigation of the hydrogen diffusion in $FeTiH_x$ by means of quasielastic neutron scattering”. en. In: *Journal of Physics F: Metal Physics* 9.6 (June 1979). Publisher: IOP Publishing, pp. 1057–1064. ISSN: 0305-4608. DOI: `10.1088/0305-4608/9/6/012`. URL: `https://doi.org/10.1088/0305-4608/9/6/012`.

[34] U. Stuhr et al. “Hydrogen Diffusion in f.c.c. TiHx and YHx : Two Distinct Examples for Diffusion in a Concentrated Lattice Gas”. en. In: *Europhysics Letters (EPL)* 20.2 (Sept. 1992). Publisher: IOP Publishing, pp. 117–123. ISSN: 0295-5075. DOI: `10.1209/0295-5075/20/2/005`.

[35] Xunxiang Hu, Ercan Cakmak, and Eugene Mamontov. *Hydrogen diffusivity measurements of YH1. 87 moderator materials with incoherent quasi elastic neutron scattering*. Tech. rep. Oak Ridge National Lab.(ORNL), Oak Ridge, TN (United States), 2020.

[36] Eric Novak et al. “Uncovering the hydride ion diffusion pathway in barium hydride via neutron spectroscopy”. In: *Scientific Reports* 12.1 (Apr. 2022), p. 6194. ISSN: 2045-2322. DOI: `10.1038/s41598-022-10199-8`. URL: `https://doi.org/10.1038/s41598-022-10199-8`.

[37] Ryou Yasuda et al. “Application of hydrogen analysis by neutron imaging plate method to Zircaloy cladding tubes”. en. In: *Journal of Nuclear Materials* 320.3 (Aug. 2003), pp. 223–230. ISSN: 0022-3115. DOI: `10.1016/S0022-3115(03)00112-0`. URL: `https://www.sciencedirect.com/science/article/pii/S0022311503001120`.

References

[38] M. Grosse et al. “In-situ neutron radiography investigations of hydrogen diffusion and absorption in zirconium alloys”. en. In: *Nuclear Instruments and Methods in Physics Research Section A: Accelerators, Spectrometers, Detectors and Associated Equipment* 651.1 (Sept. 2011), pp. 253–257. ISSN: 0168-9002. DOI: `10.1016/j.nima.2010.12.070`. URL: `https://www.sciencedirect.com/science/article/pii/S0168900210028111`.

[39] Beate Pfretzschner, Thomas Schaupp, and Axel Griesche. “Hydrogen in Metals Visualized by Neutron Imaging”. In: *Corrosion* 75.8 (Apr. 2019), pp. 903–910. ISSN: 0010-9312. DOI: `10.5006/3104`. URL: `https://doi.org/10.5006/3104`.

[40] J. R. Santisteban et al. “Diffusion of H in Zircaloy-2 and Zr-2.5%Nb rolled plates between 250 °C and 350 °C by off-situ neutron imaging experiments”. en. In: *Journal of Nuclear Materials* 561 (Apr. 2022), p. 153547. ISSN: 0022-3115. DOI: `10.1016/j.jnucmat.2022.153547`. URL: `https://www.sciencedirect.com/science/article/pii/S0022311522000435`.

[41] Holly R. Trellue et al. “Effects of Hydrogen Redistribution at High Temperatures in Yttrium Hydride Moderator Material”. In: *JOM* 73.11 (Nov. 2021), pp. 3513–3518. ISSN: 1543-1851. DOI: `10.1007/s11837-021-04898-2`. URL: `https://doi.org/10.1007/s11837-021-04898-2`.

[42] A.G. Beattie. “Acoustic Velocity Measurements in the Metal Hydrides, ScH1.99, YH1.93, and ErH1.81”. In: *Journal of Applied Physics* 43.7 (July 1972), pp. 3219–3221. ISSN: 0021-8979. DOI: `10.1063/1.1661692`. URL: `https://aip.scitation.org/doi/10.1063/1.1661692`.

[43] Walter Wolf and Peter Herzig. “First-principles investigations of transition metal dihydrides, TH2: T = Sc, Ti, V, Y, Zr, Nb: energetics and chemical bonding”. en. In: *Journal of Physics: Condensed Matter* 12.21 (May 2000), pp. 4535–4551. ISSN: 0953-8984. DOI: `10.1088/0953-8984/12/21/301`.

[44] Jin Wen Yang, Tao Gao, and Lin Yuan Guo. “Ab initio study of the structural, mechanical, and dynamical properties of the rare-earth dihydrides XH2 (X=Sc, Y, and La)”. In: *Physica B: Condensed Matter* 429 (Nov. 2013), pp. 119–126. ISSN: 0921-4526. DOI: `10.1016/j.physb.2013.08.008`. URL: `http://www.sciencedirect.com/science/article/pii/S0921452613004717`.

[45] Peter A. Schultz and Clark S. Snow. “Mechanical properties of metal dihydrides”. en. In: *Modelling and Simulation in Materials Science and Engineering* 24.3 (Feb. 2016), p. 035005. ISSN: 0965-0393. DOI: `10.1088/0965-0393/24/3/035005`.

[46] Vedant K. Mehta et al. “A density functional theory and neutron diffraction study of the ambient condition properties of sub-stoichiometric yttrium hydride”. In: *Journal of Nuclear Materials* 547 (2021), p. 152837. ISSN: 0022-3115. DOI: `https://doi.org/10.1016/j.jnucmat.2021.152837`. URL: `https://www.sciencedirect.com/science/article/pii/S002231152100060X`.

[47] Vedant K Mehta et al. “Evaluation of Yttrium Hydride (δ-YH2-x) Thermal Neutron Scattering Laws and Thermophysical Properties”. In: *Nuclear Science and Engineering* 195.6 (2021), pp. 563–577.

[48] Vedant K Mehta et al. “A modeling and neutron diffraction study of the high temperature properties of sub-stoichiometric yttrium hydride for novel moderator applications”. In: *Metals* 12.2 (2022), p. 199.

[49] Jeremy Lloyd Conlin et al. "NJOY Status in 2018". In: Santa Fe, NM: American Nuclear Society, Aug. 2018.

[50] T. Cutler et al. "The Hypatia Experiment: Yttrium Hydride and Highly Enriched Uranium Critical Experiment". In: *Nuclear Technology* 0.0 (Apr. 2022). Publisher: Taylor & Francis _eprint: https://doi.org/10.1080/00295450.2022.2027146, pp. 1–17. ISSN: 0029-5450. DOI: `10.1080/00295450.2022.2027146`. URL: `https://doi.org/10.1080/00295450.2022.2027146`.

[51] U.S. Geological Survey. *2021 Draft List of Critical Minerals.*

[52] K. Kane et al. "Air oxidation of yttrium hydride as a high temperature moderator for thermal neutron spectrum fission reactors". en. In: *Journal of Nuclear Materials* 556 (Dec. 2021), p. 153166. ISSN: 0022-3115. DOI: `10.1016/j.jnucmat.2021.153166`. URL: `https://www.sciencedirect.com/science/article/pii/S0022311521003895`.

[53] Wei-E Wang and Donald R. Olander. "Thermodynamics of the Zr-H System". In: *Journal of the American Ceramic Society* 78.12 (1995), pp. 3323–3328.

[54] Christopher Matthews, Aditya Prahlad Shivprasad, and Michael William Donald Cooper. *Metal Hydride Simulations Using SWIFT*. English. Tech. rep. LA-UR-21-27538. Los Alamos National Lab. (LANL), Los Alamos, NM (United States), Nov. 2021. DOI: `10.2172/1829624`. URL: `https://www.osti.gov/biblio/1829624`.

[55] JAMES P. Blackledge. "CHAPTER 10 - Yttrium and Scandium Hydrides". In: *Metal Hydrides*. Academic Press, 1968, pp. 441–489. ISBN: 978-1-4832-3215-7. DOI: `10.1016/B978-1-4832-3215-7.50014-9`. URL: `https://www.sciencedirect.com/science/article/pii/B9781483232157500149`.

[56] D. Khatamian and F. D. Manchester. "The H-Y (Hydrogen-Yttrium) system". en. In: *Bulletin of Alloy Phase Diagrams* 9.3 (June 1988), pp. 252–260. ISSN: 0197-0216. DOI: `10.1007/BF02881276`. URL: `https://doi.org/10.1007/BF02881276`.

[57] M. Mansmann and W. E. Wallace. "The structure of HoD_3". en. In: *Journal de Physique* 25.5 (May 1964), pp. 454–459. ISSN: 0368-3842. DOI: `10.1051/jphys:01964002505045400`. URL: `http://dx.doi.org/10.1051/jphys:01964002505045400`.

[58] A. Machida et al. "X-ray diffraction investigation of the hexagonal-fcc structural transition in yttrium trihydride under hydrostatic pressure". In: *Solid State Communications* 138.9 (June 2006), pp. 436–440. ISSN: 0038-1098. DOI: `10.1016/j.ssc.2006.04.011`. URL: `http://www.sciencedirect.com/science/article/pii/S0038109806003218`.

[59] L. N. Yannopoulos, R. K. Edwards, and P. G. Wahlbeck. "The Thermodynamics of the Yttrium-Hydrogen System". In: *The Journal of Physical Chemistry* 69.8 (Aug. 1965), pp. 2510–2515. ISSN: 0022-3654. DOI: `10.1021/j100892a004`. URL: `https://doi.org/10.1021/j100892a004`.

[60] Kai Fu et al. "Experimental investigation and thermodynamic assessment of the yttrium-hydrogen binary system". en. In: *Progress in Natural Science: Materials International* 28.3 (June 2018), pp. 332–336. ISSN: 1002-0071. DOI: `10.1016/j.pnsc.2018.04.001`. URL: `http://www.sciencedirect.com/science/article/pii/S1002007117309747`.

References

[61] Jiaqing Peng et al. “Thermodynamic modelling of Y–H and Y–Zr–H system aided by first-principles and its application in bulk hydride moderator fabrication”. en. In: *Journal of Nuclear Materials* 531 (Apr. 2020), p. 152035. ISSN: 0022-3115. DOI: `10.1016/j.jnucmat.2020.152035`. URL: `http://www.sciencedirect.com/science/article/pii/S0022311519303551`.

[62] P. P. Kong et al. “Superconductivity up to 243 K in yttrium hydrides under high pressure”. In: *arXiv:1909.10482 [cond-mat]* (Sept. 2019). arXiv: 1909.10482. URL: `http://arxiv.org/abs/1909.10482`.

[63] Ivan A. Troyan et al. “Anomalous high-temperature superconductivity in YH_6”. In: *arXiv:1908.01534 [cond-mat]* (June 2020). arXiv: 1908.01534. URL: `http://arxiv.org/abs/1908.01534`.

[64] F. H. Spedding, A. H. Daane, and K. W. Herrmann. “The crystal structures and lattice parameters of high-purity scandium, yttrium and the rare earth metals”. en. In: *Acta Crystallographica* 9.7 (July 1956), pp. 559–563. ISSN: 0365-110X. DOI: `10.1107/S0365110X5600156X`. URL: `//scripts.iucr.org/cgi-bin/paper?a01745`.

[65] B. J. Beaudry and F. H. Spedding. “The solubility of RH2-xin Gd, Er, Tm, Lu and Y from ambient to 850°C”. en. In: *Metallurgical Transactions B* 6.3 (Sept. 1975), p. 419. ISSN: 1543-1916. DOI: `10.1007/BF02913827`. URL: `https://doi.org/10.1007/BF02913827`.

[66] A. Pebler and W. E. Wallace. “CRYSTAL STRUCTURES OF SOME LANTHANIDE HYDRIDES”. In: *The Journal of Physical Chemistry* 66.1 (Jan. 1962), pp. 148–151. ISSN: 0022-3654. DOI: `10.1021/j100807a033`. URL: `https://doi.org/10.1021/j100807a033`.

[67] T. Palasyuk and M. Tkacz. “Hexagonal to cubic phase transition in YH3 under high pressure”. In: *Solid State Communications* 133.7 (Feb. 2005), pp. 477–480. ISSN: 0038-1098. DOI: `10.1016/j.ssc.2004.11.035`. URL: `http://www.sciencedirect.com/science/article/pii/S0038109804009962`.

[68] P. G. Dantzer and O. J. Kleppa. “High temperature thermodynamics of the yttrium–hydrogen systems”. In: *The Journal of Chemical Physics* 73.10 (Nov. 1980), pp. 5259–5263. ISSN: 0021-9606. DOI: `10.1063/1.439954`. URL: `https://aip.scitation.org/doi/abs/10.1063/1.439954`.

[69] Yuh Fukai. *The Metal-Hydrogen System: Basic Bulk Properties*. en. Google-Books-ID: CshrIxMIQaoC. Springer Science & Business Media, Feb. 2006. ISBN: 978-3-540-28883-1.

[70] S. Richmond et al. “The solubility of hydrogen and deuterium in alloyed, unalloyed and impure plutonium metal”. en. In: *IOP Conference Series: Materials Science and Engineering* 9 (Mar. 2010). Publisher: IOP Publishing, p. 012036. ISSN: 1757-899X. DOI: `10.1088/1757-899X/9/1/012036`.

[71] Mats Hillert. *Phase Equilibria, Phase Diagrams and Phase Transformations: Their Thermodynamic Basis*. en. Google-Books-ID: juk4cxteC1AC. Cambridge University Press, Nov. 2007. ISBN: 978-1-139-46586-1.

[72] Joseph Bloch and Moshe H Mintz. “Kinetics and mechanisms of metal hydrides formation—a review”. en. In: *Journal of Alloys and Compounds* 253-254 (May 1997), pp. 529–541. ISSN: 0925-8388. DOI: `10.1016/S0925-8388(96)03070-8`. URL: `http://www.sciencedirect.com/science/article/pii/S0925838896030708`.

[73] G. M. Begun, J. F. Land, and J. T. Bell. “High temperature equilibrium measurements of the yttrium–hydrogen isotope (H2, D2, T2) systems.” In: *The Journal of Chemical Physics* 72.5 (Mar. 1980), pp. 2959–2966. ISSN: 0021-9606. DOI: `10.1063/1.439496`. URL: `https://aip.scitation.org/doi/abs/10.1063/1.439496`.

[74] M. Tanase, P. W. Fisher, and J. S. Watson. “Isothermal equilibrium pressures of a Y-Nb alloy-H$_2$ system”. In: *Journal of the Less Common Metals* 99.1 (1984), pp. 23–31. ISSN: 0022-5088. DOI: `https://doi.org/10.1016/0022-5088(84)90332-1`. URL: `https://www.sciencedirect.com/science/article/pii/0022508884903321`.

[75] Vincenc Nemanic. “Hydrogen permeation barriers: Basic requirements, materials selection, deposition methods, and quality evaluation”. en. In: *Nuclear Materials and Energy* 19 (May 2019), pp. 451–457. ISSN: 2352-1791. DOI: `10.1016/j.nme.2019.04.001`. URL: `http://www.sciencedirect.com/science/article/pii/S2352179119300109`.

[76] C San Marchi and Brian P Somerday. “Technical reference on hydrogen compatibility of materials”. In: *Sandia National Laboratories, SANDIA REPORT SAND2008-1163* (2008), pp. 1211–1.

[77] VN FADEYEV. “DISSOCIATION PRESSURES IN YTTRIUM-HYDROGEN SYSTEM”. In: *RUSSIAN METALLURGY* 5 (1972). ISBN: 0036-0295 Publisher: ALLERTON PRESS INC 150 FIFTH AVE, NEW YORK, NY 10011, pp. 148–150.

[78] D. Sarussi et al. “The kinetics and mechanism of cerium hydride formation”. en. In: *Journal of Alloys and Compounds* 191.1 (Jan. 1993), pp. 91–99. ISSN: 0925-8388. DOI: `10.1016/0925-8388(93)90277-T`. URL: `http://www.sciencedirect.com/science/article/pii/092583889390277T`.

[79] Jason R. Hattrick-Simpers et al. “Observation of phase transitions in hydrogenated Yttrium films via normalized infrared emissivity”. en. In: *Journal of Alloys and Compounds* 490.1 (Feb. 2010), pp. 42–46. ISSN: 0925-8388. DOI: `10.1016/j.jallcom.2009.10.054`. URL: `http://www.sciencedirect.com/science/article/pii/S0925838809020301`.

[80] F Wöhler. “Über das Beryllium und Yttrium”. In: *Annalen der Physik* 89.8 (1828), pp. 577–582.

[81] *The Rare Earths*. NY, John Wiley & Sons, Incorporated, 1961. URL: `https://books.google.com/books?id=QpzXzwEACAAJ`.

[82] COY L. Huffine. “CHAPTER 13 - Fabrication of Hydrides”. In: *Metal Hydrides*. Ed. by William M. Mueller, James P. Blackledge, and George G. Libowitz. Academic Press, Jan. 1968, pp. 675–747. ISBN: 978-1-4832-3215-7. DOI: `10.1016/B978-1-4832-3215-7.50017-4`. URL: `http://www.sciencedirect.com/science/article/pii/B9781483232157500174`.

[83] Howard E. Flotow, Darrell W. Osborne, and Klaus Otto. “Heat Capacities and Thermodynamic Functions of YH2 and YD2 from 5° to 350°K and the Hydrogen Vibration Frequencies”. In: *The Journal of Chemical Physics* 36.4 (Feb. 1962), pp. 866–872. ISSN: 0021-9606. DOI: `10.1063/1.1732681`. URL: `https://aip.scitation.org/doi/abs/10.1063/1.1732681`.

[84] C. E. Lundin and D. T. Klodt. *FUNDAMENTAL ALLOY DEVELOPMENT. Quarterly Progress Report, August 1, 1959- October 31, 1959*. English. Tech. rep. TID-6728; XDC-60-9-72. Denver. Univ. Denver Research Inst., Nov. 1959. URL: `https://www.osti.gov/biblio/4674996`.

References

[85] Masato Ito. “Studies on physical properties of metal hydrides and hydrogen behavior in Zr alloys”. In: (2008).

[86] S. Narasimhan. “Phonon softening and the anomalous thermal expansion of Ag(111)”. In: *Surface Science* 417.2 (1998), pp. L166–L172. ISSN: 0039-6028. DOI: `https://doi.org/10.1016/S0039-6028(98)00739-0`. URL: `https://www.sciencedirect.com/science/article/pii/S0039602898007390`.

[87] R. Mittal, M. K. Gupta, and S. L. Chaplot. “Phonons and anomalous thermal expansion behaviour in crystalline solids”. In: *Progress in Materials Science* 92 (2018), pp. 360–445. ISSN: 0079-6425. DOI: `https://doi.org/10.1016/j.pmatsci.2017.10.002`. URL: `https://www.sciencedirect.com/science/article/pii/S0079642517301184`.

[88] Xunxiang Hu et al. *Handbook on the Material Properties of Yttrium Hydride for High Temperature Moderator Applications*. Tech. rep. Oak Ridge National Lab.(ORNL), Oak Ridge, TN (United States), 2021.

[89] J. H. Weaver, R. Rosei, and D. T. Peterson. “Electronic structure of metal hydrides. I. Optical studies of ScH_2, YH_2, and LuH_2”. In: *Physical Review B* 19.10 (May 1979). Publisher: American Physical Society, pp. 4855–4866. DOI: `10.1103/PhysRevB.19.4855`. URL: `https://link.aps.org/doi/10.1103/PhysRevB.19.4855`.

[90] Yan Wang and M. Y. Chou. “Structural and electronic properties of hexagonal yttrium trihydride”. In: *Physical Review B* 51.12 (Mar. 1995). Publisher: American Physical Society, pp. 7500–7507. DOI: `10.1103/PhysRevB.51.7500`. URL: `https://link.aps.org/doi/10.1103/PhysRevB.51.7500`.

[91] P. Vajda. “Hydrogen in rare earths: a wealth of structural and electronic phenomena”. In: *Solid State Ionics*. Proceedings of the Workshop on Hydrogen: Ionic, Atomic and Molecular Motion 168.3 (Mar. 2004), pp. 271–279. ISSN: 0167-2738. DOI: `10.1016/j.ssi.2002.11.001`. URL: `http://www.sciencedirect.com/science/article/pii/S0167273803004302`.

[92] M. Sakai et al. “Magnetotransport properties in near-stoichiometric hydride films of $YH_{2+\delta}$ under weak fields”. In: *Journal of Applied Physics* 101.10 (May 2007). Publisher: American Institute of Physics, p. 103713. ISSN: 0021-8979. DOI: `10.1063/1.2733602`. URL: `https://aip.scitation.org/doi/full/10.1063/1.2733602`.

[93] P. Vajda. “Hydrogen in rare-earth metals, including RH2+x phases”. en. In: *Handbook on the Physics and Chemistry of Rare Earths*. Vol. 20. Elsevier, Jan. 1995, pp. 207–291. DOI: `10.1016/S0168-1273(05)80071-6`. URL: `http://www.sciencedirect.com/science/article/pii/S0168127305800716`.

[94] P. Vajda and J. N. Daou. “Semiconductor-metal-semiconductor transitions in the superstoichiometric dihydride YH2.10”. In: *Physical Review Letters* 66.24 (June 1991). Publisher: American Physical Society, pp. 3176–3178. DOI: `10.1103/PhysRevLett.66.3176`. URL: `https://link.aps.org/doi/10.1103/PhysRevLett.66.3176`.

[95] J. N. Daou and P. Vajda. “Hydrogen ordering and metal-semiconductor transitions in the system YH2+x”. In: *Physical Review B* 45.19 (May 1992), pp. 10907–10913. DOI: `10.1103/PhysRevB.45.10907`. URL: `https://link.aps.org/doi/10.1103/PhysRevB.45.10907`.

[96] Pierre Villars and Fritz Hulliger. *YH2 permittivity (dielectric constant): Datasheet from "PAULING FILE Multinaries Edition – 2012" in SpringerMaterials (https://materials.springer.com/isp/phy property/docs/ppp_ 0a021c0b47f55ab175d102aee03629b0).* URL: `https://materials.springer.com/isp/physical-property/docs/ppp_0a021c0b47f55ab175d102aee03629b0`.

[97] Pierre Villars and Fritz Hulliger. *YH2 charge carrier concentration: Datasheet from "PAULING FILE Multinaries Edition – 2012" in SpringerMaterials (https://materials.springer.com/isp/physical-property/docs/ppp_ c0566a127ed023216a77f8d46e049133).* URL: `https://materials.springer.com/isp/physical-property/docs/ppp_c0566a127ed023216a77f8d46e049133`.

[98] Pierre Villars and Fritz Hulliger. *YH2 conductivity/resistivity: Datasheet from "PAULING FILE Multinaries Edition – 2012" in SpringerMaterials (https://materials.springer.com/isp/physical-property/docs/ppp_ e9c3df5efd481075c2be74ce36264382).* URL: `https://materials.springer.com/isp/physical-property/docs/ppp_e9c3df5efd481075c2be74ce36264382`.

[99] Pierre Villars and Fritz Hulliger. *YH3 rt permittivity (dielectric constant): Datasheet from "PAULING FILE Multinaries Edition – 2012" in SpringerMaterials (https://materials.springer.com/isp/phy property/docs/ppp_ 8f0042dbf6c3237619b6b1c293b1f392).* URL: `https://materials.springer.com/isp/physical-property/docs/ppp_8f0042dbf6c3237619b6b1c293b1f392`.

[100] R. R. Arons and H.P.J. Wijn. *2.3.8 Nuclear spin resonance: Datasheet from Landolt-Börnstein - Group III Condensed Matter · Volume 19D1: "Rare Earth Elements, Hydrides and Mutual Alloys" in SpringerMaterials (https://doi.org/10.1007/10013330_ 71).* DOI: `10.1007/10013330_71`. URL: `https://materials.springer.com/lb/docs/sm_lbs_978-3-540-46884-4_71`.

[101] Xunxiang Hu and Kurt A. Terrani. "Thermomechanical properties and microstructures of yttrium hydride". en. In: *Journal of Alloys and Compounds* 867 (June 2021), p. 158992. ISSN: 0925-8388. DOI: `10.1016/j.jallcom.2021.158992`. URL: `https://www.sciencedirect.com/science/article/pii/S0925838821003996`.

[102] Amey Khanolkar et al. "High temperature elastic properties of sub-stoichiometric yttrium dihydrides". In: *Materials Today Communications* 35 (2023), p. 105879. ISSN: 2352-4928. DOI: `https://doi.org/10.1016/j.mtcomm.2023.105879`. URL: `https://www.sciencedirect.com/science/article/pii/S2352492823005706`.

[103] E. S. Funston. "PHYSICAL PROPERTIES OF YTTRIUM HYDRIDE". English. In: *Met. Soc. Am. Inst. Mining, Met. Petrol. Engrs., Inst. Metals Div.* Vol: Spec. Rept. Ser. No. 10 (Jan. 1960). URL: `https://www.osti.gov/biblio/4020288`.

[104] A. Abragam. *The Principles of Nuclear Magnetism.* en. Google-Books-ID: 9M8U_JK7K54C. Clarendon Press, 1961. ISBN: 978-0-19-852014-6.

[105] Malcolm H Levitt. "Spin dynamics: Basics of Nuclear Magnetic Resonance John Wiley & Sons". In: *New York-London-Sydney* (2008).

[106] Takatsugu Endo et al. "Cation and anion dynamics in supercooled and glassy states of the ionic liquid 1-butyl-3-methylimidazolium hexafluorophosphate: Results from 13C, 31P, and 19F NMR spectroscopy". In: *Physical Review B* 85.5 (Feb. 2012). Publisher: American Physical Society, p. 054307. DOI: `10.1103/PhysRevB.85.054307`. URL: `https://link.aps.org/doi/10.1103/PhysRevB.85.054307`.

References

[107] E. L. Gjersing et al. “Anomalously large decoupling of rotational and shear relaxation in a molecular glass”. In: *Physical Review B* 76.21 (Dec. 2007). Publisher: American Physical Society, p. 214202. DOI: `10.1103/PhysRevB.76.214202`. URL: `https://link.aps.org/doi/10.1103/PhysRevB.76.214202`.

[108] Maxwell A. T. Marple et al. “Observation of a Phonon Softening Effect on Li Ion Conduction in Mixed-Anion Chalcogenide Glasses”. In: *Chemistry of Materials* 30.17 (Sept. 2018). Publisher: American Chemical Society, pp. 5896–5903. ISSN: 0897-4756. DOI: `10.1021/acs.chemmater.8b01830`. URL: `https://doi.org/10.1021/acs.chemmater.8b01830`.

[109] Young Joo Lee, Charlotte Eng, and Clare P. Grey. “^{6}Li Magic Angle Spinning NMR Study of the Cathode Material $LiNi_xMn_{2\text{-}x}O_4$: The Effect of Ni Doping on the Local Structure during Charging”. en. In: *Journal of The Electrochemical Society* 148.3 (Mar. 2001). Publisher: IOP Publishing, A249. ISSN: 1945-7111. DOI: `10.1149/1.1350658`. URL: `https://iopscience.iop.org/article/10.1149/1.1350658/meta`.

[110] M. Bée. *Quasielastic neutron scattering (Adam Hilger)*. IOP Publishing Ltd: Bristol, England, 1988.

[111] G Majer et al. “Model-independent measurements of hydrogen diffusivity in the yttrium dihydrides”. en. In: *Journal of Alloys and Compounds*. Proceedings of the International Symposium on Metal-Hydrogen Systems, Fundamentals and Applications (MH2000) 330-332 (Jan. 2002), pp. 438–442. ISSN: 0925-8388. DOI: `10.1016/S0925-8388(01)01452-9`. URL: `http://www.sciencedirect.com/science/article/pii/S0925838801014529`.

[112] Peter A. Fedders and O. F. Sankey. “Correlation functions for simple hopping in a simple cubic lattice”. In: *Physical Review B* 18.11 (Dec. 1978). Publisher: American Physical Society, pp. 5938–5947. DOI: `10.1103/PhysRevB.18.5938`. URL: `https://link.aps.org/doi/10.1103/PhysRevB.18.5938`.

[113] J. C. Marshall, R. Van Houten, and W. G. Baxter. *YTTRIUM HYDRIDE MODERATOR EVALUATION–IN-PILE THERMAL STABILITY*. Tech. rep. General Electric Co. Flight Propulsion Lab., Dept., Cincinnati, 1962.

[114] M. T. Simnad. “The U-ZrH_x alloy: Its properties and use in TRIGA fuel”. en. In: *Nuclear Engineering and Design* 64.3 (Apr. 1981), pp. 403–422. ISSN: 0029-5493. DOI: `10.1016/0029-5493(81)90135-7`. URL: `https://www.sciencedirect.com/science/article/pii/0029549381901357`.

[115] Yueling Guo et al. “Enhancing the oxidation resistance of Nb-Si based alloys by yttrium addition”. en. In: *Intermetallics* 101 (Oct. 2018), pp. 165–172. ISSN: 0966-9795. DOI: `10.1016/j.intermet.2018.08.004`. URL: `http://www.sciencedirect.com/science/article/pii/S096697951830311X`.

[116] Donald R. Olander, Kenji Konashi, and Michio Yamawaki. “5.08 - Uranium–Zirconium Hydride Fuel”. In: *Comprehensive Nuclear Materials (Second Edition)*. Ed. by Rudy J.M. Konings and Roger E. Stoller. Oxford: Elsevier, 2012, pp. 209–255. ISBN: 978-0-08-102866-7.

[117] R. L. Beck and W. M. Mueller. “CHAPTER 7 - Zirconium Hydrides and Hafnium Hydrides”. In: *Metal Hydrides*. Ed. by William M. Mueller, James P. Blackledge, and George G. Libowitz. Academic Press, 1968, pp. 241–335. ISBN: 978-1-4832-3215-7.

[118] E Zuzek et al. “The H-Zr (hydrogen-zirconium) system”. In: *Bulletin of alloy phase diagrams* 11.4 (1990), pp. 385–395.

[119] M Christensen et al. “H in α-Zr and in zirconium hydrides: solubility, effect on dimensional changes, and the role of defects”. In: *Journal of Physics: Condensed Matter* 27.2 (Dec. 2014), p. 025402.

[120] R Khoda-Bakhsh and D K Ross. “Determination of the hydrogen site occupation in the α phase of zirconium hydride and in the and phases of titanium hydride by inelastic neutron scattering”. In: *Journal of Physics F: Metal Physics* 12.1 (Jan. 1982), p. 15.

[121] P.P. Narang, G.L. Paul, and K.N.R. Taylor. “Location of hydrogen in α-zirconium”. In: *Journal of the Less Common Metals* 56.1 (1977), pp. 125–128. ISSN: 0022-5088.

[122] R. C. Bowman et al. “Effects of thermal treatments on the lattice properties and electronic structure of ZrH_x”. In: *Phys. Rev. B* 31 (9 May 1985), pp. 5604–5615.

[123] S. S. Sidhu et al. “Neutron and X-Ray Diffraction Studies of Nonstoichiometric Metal Hydrides”. In: *Nonstoichiometric Compounds, Advances in ChemistryVol. 39*. 1963. Chap. 8, pp. 87–98.

[124] V. F. Petrunin et al. “INVESTIGATION OF PHASE EQUILIBRIA IN ZIRCONIUM DEUTERIDES”. In: *Physics of metals and metallography* 46.1 (1978), pp. 181–184. ISSN: 0031-918X.

[125] R. E. Rundle, C. G. Shull, and E. O. Wollan. “The crystal structure of thorium and zirconium dihydrides by X-ray and neutron diffraction”. In: *Acta Crystallographica* 5.1 (Jan. 1952), pp. 22–26.

[126] L. Espagno, P. Azou, and P. Bastien. “X RAY STUDY OF THE HYDROGEN-ZIRCONIUM SYSTEM”. In: *Compt. rend* 249 (1959).

[127] Z. Zhao et al. “Identification and characterization of a new zirconium hydride”. In: *Journal of Microscopy* 232.3 (2008), pp. 410–421.

[128] M.H.A. Piro et al. “The thermochemistry library Thermochimica”. In: *Computational Materials Science* 67 (2013), pp. 266–272. ISSN: 0927-0256.

[129] J. W. Raymond. *Equilibrium Dissociation Pressures of the Delta and Epsilon Phases in the Zirconium-Hydrogen System , Report No. NAA-SR-9374*. 1964.

[130] Russell K Edwards, Pascal Levesque, and D Cubicciotti. “Solid Solution Equilibria in the Zirconium-Hydrogen System”. In: *Journal of the American Chemical Society* 77.5 (1955), pp. 1307–1311.

[131] KP Singh and J Gordon Parr. “Hydrogen solubility in Zr—O alloys”. In: *Transactions of the Faraday Society* 59 (1963), pp. 2248–2255.

[132] Lee D LaGrange et al. “A study of the zirconium-hydrogen and zirconium-hydrogen–uranium systems between 600°C and 800°C”. In: *The Journal of Physical Chemistry* 63.12 (1959), pp. 2035–2041.

[133] RL Beck. “Zirconium-hydrogen phase system”. In: *Am. Soc. Metals, Trans. Quart.* 55 (1962).

[134] George G Libowitz. “A pressure-composition-temperature study of the zirconium-hydrogen system at high hydrogen contents”. In: *Journal of Nuclear Materials* 5.2 (1962), pp. 228–233. ISSN: 0022-3115.

[135] H. Muta et al. “Effect of hydrogenation conditions on the microstructure and mechanical properties of zirconium hydride”. In: *Journal of Nuclear Materials* 500 (2018), pp. 145–152.

References

[136] M.P. Cassidy and C.M. Wayman. “The crystallography of hydride formation in zirconium: I. The $\delta \rightarrow \gamma$ transformation”. In: *Metallurgical Transactions A* 11.1 (1980), pp. 47–56.

[137] M.P. Cassidy and C.M. Wayman. “The crystallography of hydride formation in zirconium: II. The $\delta \rightarrow \varepsilon$ transformation”. In: *Metallurgical Transactions A* 11.1 (1980), pp. 57–67.

[138] Hui He et al. “Densification, hydrogen retention, microstructure, and mechanical properties of ε-ZrH_{2-x} monolith fabricated by high-pressure spark plasma sintering”. In: *Journal of the European Ceramic Society* 44.11 (2024), pp. 6179–6191. ISSN: 0955-2219.

[139] W. Wang et al. “Hydrogen Permeation Behavior of Zirconium Nitride Film on Zirconium Hydride”. In: *Materials* 15 (2 2022), p. 550.

[140] W. Wang et al. “Mechanisms of Growth and Hydrogen Permeation of Zirconium Nitride Film on Zirconium Hydride”. In: *Materials* 16 (0 2023), p. 349.

[141] D. Parkison et al. “Fabrication of bulk delta-phase Zirconium Hydride from Zircaloy-4 for use as moderators in microreactors”. In: *Scripta Materialia* 239 (0 2024), p. 115771.

[142] T. -T. Phua et al. “Paramagnetic impurity effects in NMR determinations of hydrogen diffusion and electronic structure in metal hydrides. Gd^{3+} in YH_2 and $LaH_{2.25}$”. In: *Phys. Rev. B* 28 (11 Dec. 1983), pp. 6227–6250.

[143] R C Bowman Jr and B D Craft. “Rotating-frame relaxation time study of hydrogen diffusion in ZrH_x”. In: *Journal of Physics C: Solid State Physics* 17.19 (July 1984), p. L477.

[144] J-W. Han et al. “Anomalous proton-spin-lattice relaxation at high temperatures in zirconium dihydrides”. In: *Phys. Rev. B* 44 (22 Dec. 1991), pp. 12353–12360.

[145] J. F. Hon. “Nuclear Magnetic Resonance Study of the Diffusion of Hydrogen in Zirconium Hydride”. In: *The Journal of Chemical Physics* 36.3 (Feb. 1962), pp. 759–763. ISSN: 0021-9606.

[146] G Majer, W Renz, and R G Barnes. “The mechanism of hydrogen diffusion in zirconium dihydrides”. In: *Journal of Physics: Condensed Matter* 6.15 (Apr. 1994), p. 2935.

[147] H. Wipf, B. Kappesser, and R. Werner. “Hydrogen diffusion in titanium and zirconium hydrides”. In: *Journal of Alloys and Compounds* 310.1 (2000). Intern. Conf. Internal Friction and Ultrasonic Attentuation in Solids (ICIFUAS-12), pp. 190–195. ISSN: 0925-8388.

[148] Peter A. Fedders and O. F. Sankey. “Correlation functions for simple hopping in a simple cubic lattice”. In: *Phys. Rev. B* 18 (11 1978), pp. 5938–5947.

[149] Kurt A. Terrani, Jeffrey E. Seifried, and Donald R. Olander. “Transient hydride fuel behavior in LWRs”. In: *Journal of Nuclear Materials* 392.2 (2009). Nuclear Fuels and Structural Materials 2, pp. 192–199. ISSN: 0022-3115.

[150] A. W. Sommer and W. F. Dennsion. *Thermal diffusion of hydrogen in nonstoichiometric zirconiuim-dihydride, Report No. NAA-SR-5066.* 1960.

[151] D. Olander et al. “Uranium–zirconium hydride fuel properties”. In: *Nuclear Engineering and Design* 239.8 (2009), pp. 1406–1424. ISSN: 0029-5493.

[152] U. Merten et al. “Thermal migration of hydrogen in zirconium-uranium-hydrogen alloys”. In: *Journal of Nuclear Materials* 10.3 (1963), pp. 201–208. ISSN: 0022-3115.

[153] P. Paetz and K. Lücke. “On the Kinetics of Hydrogen Engassing of Delta-Zirconium Hydride”. In: *International Journal of Materials Research* 62 (1971), p. 657. ISSN: 0022-3115.

[154] W. M. Albrecht and W. D. Goode Jr. *The diffusion of hydrogen in zircnoium hydride, Report No. BMI-1426*. 1960.

[155] S. D. Harkness and W. A. Young. *The diffusion coefficient of hydrogen in delta-phase zirconium hydride, Report No. NAA-SR-10516*. 1965.

[156] Earl A. Gulbransen and Kenneth F. Andrew. "Diffusion of Hydrogen and Deuterium in High Purity Zirconium". In: *Journal of The Electrochemical Society* 101.11 (1954), p. 560.

[157] C. Korn and S. D. Goren. "NMR study of hydrogen diffusion in zirconium hydride". In: *Phys. Rev. B* 33 (1 Jan. 1986), pp. 68–78.

[158] Weidong Chen, Lijun Wang, and Shigang Lu. "Influence of oxide layer on hydrogen desorption from zirconium hydride". In: *Journal of Alloys and Compounds* 469.1 (2009), pp. 142–145. ISSN: 0925-8388.

[159] Xunxiang Hu, Kurt A. Terrani, and Brian D. Wirth. "Hydrogen desorption kinetics from zirconium hydride and zirconium metal in vacuum". In: *Journal of Nuclear Materials* 448.1 (2014), pp. 87–95. ISSN: 0022-3115.

[160] Doonyapong Wongsawaeng and Sarawut Jaiyen. "High-temperature absolute hydrogen desorption kinetics of zirconium hydride under clean and oxidized surface conditions". In: *Journal of Nuclear Materials* 403.1 (2010), pp. 19–24. ISSN: 0022-3115.

[161] Mingwang Ma et al. "Non-isothermal and isothermal hydrogen desorption kinetics of zirconium hydride". In: *Journal of Nuclear Materials* 467 (2015), pp. 349–356. ISSN: 0022-3115.

[162] K.A. Terrani et al. "The kinetics of hydrogen desorption from and adsorption on zirconium hydride". In: *Journal of Nuclear Materials* 397.1 (2010), pp. 61–68. ISSN: 0022-3115.

[163] D Gutkowski. "Kinetics of hydrogen uptake and release from zirconium hydride". MA thesis. Dept. of Nuclear Engineering, University of California at Berkeley, 2005.

[164] Shinsuke Yamanaka et al. "Thermal properties of zirconium hydride". In: *Journal of Nuclear Materials* 294.1 (2001). 10th Int. Symp. on Thermodynamics of Nuclear Materials, pp. 94–98. ISSN: 0022-3115.

[165] Walter J. Tomasch. "Specific Heats of Delta-Phase Zr-H and Zr-D". In: *Phys. Rev.* 123 (2 July 1961), pp. 510–514.

[166] C. C. Weeks, M. M. Nakata, and C. A. Smith. "Thermal properties of SNAP fuels". In: *Proc. 7th Conf. on Thermal Conductivity*. 1968, pp. 387–398.

[167] B. Tsuchiya et al. "Thermophysical properties of zirconium hydride and uranium–zirconium hydride". In: *Journal of Nuclear Materials* 289.3 (2001), pp. 329–333. ISSN: 0022-3115.

[168] S Yamanaka et al. "Thermal and mechanical properties of zirconium hydride". In: *Journal of Alloys and Compounds* 293-295 (1999), pp. 23–29. ISSN: 0925-8388.

[169] M.P. Puls, San-Qiang Shi, and J. Rabier. "Experimental studies of mechanical properties of solid zirconium hydrides". In: *Journal of Nuclear Materials* 336.1 (2005), pp. 73–80. ISSN: 0022-3115.

[170] A. G. Lanin et al. "Mechanical properties of zirconium, titanium and yttrium hydride alloys". In: *Problemy Prochnosti* 6 (June 1984), pp. 83–88.

References

[171] V.A. Syasin, E.B. Boyko, and V.Ya. Markin. “Investigations of Hardness, Internal Friction and Brittleness of Zirconium Hydride”. In: *Zeitschrift für Physikalische Chemie* 164.2 (1989), pp. 1567–1572.

[172] M. Nedim Cinbiz et al. “Nanoindentation study of bulk zirconium hydrides at elevated temperatures”. In: *Journal of Alloys and Compounds* 726 (2017), pp. 41–48. ISSN: 0925-8388.

[173] Jiujun Xu and San-Qiang Shi. “Investigation of mechanical properties of ε-zirconium hydride using micro- and nano-indentation techniques”. In: *Journal of Nuclear Materials* 327.2 (2004), pp. 165–170. ISSN: 0022-3115.

[174] Masatoshi Kuroda et al. “Nanoindentation studies of zirconium hydride”. In: *Journal of Alloys and Compounds* 368.1 (2004), pp. 211–214. ISSN: 0925-8388.

[175] Naoko Oono et al. “Irradiation hardening and microstructure evolution of ion-irradiated Zr-hydride”. In: *Journal of Nuclear Materials* 419.1 (2011), pp. 366–370. ISSN: 0022-3115.

[176] Naoko Oono et al. “Comparison of irradiation hardening and microstructure evolution in ion-irradiated delta and epsilon hydrides”. In: *Journal of Nuclear Materials* 442 (2013), S826–S829. ISSN: 0022-3115.

[177] I.J.S. Cherubin, M. Topping, and M.R. Daymond. “Evaluation of irradiation hardening in proton-irradiated δ-zirconium hydride and Zr2.5Nb”. In: *Journal of Nuclear Materials* 562 (0 2022), p. 153600.

[178] I.J.S. Cherubin et al. “Plastic deformation of δ-zirconium hydride during micropillar compression”. In: *Journal of Nuclear Materials* 577 (0 2023), p. 154285.

[179] Hao Wang et al. “Constitutive modeling of δ-phase zircaloy hydride based on strain rate dependent nanoindentation and nano-scale impact dataset”. In: *International Journal of Plasticity* 133 (2020), p. 102787. ISSN: 0749-6419.

[180] M.A. Martin Rengel et al. “Obtention of the constitutive equation of hydride blisters in fuel cladding from nanoindentation tests”. In: *Journal of Nuclear Materials* 487 (2017), pp. 220–228. ISSN: 0022-3115.

[181] Siddharth Suman et al. “Investigation of elevated-temperature mechanical properties of δ-hydride precipitate in Zircaloy-4 fuel cladding tubes using nanoindentation”. In: *Journal of Alloys and Compounds* 726 (2017), pp. 107–113. ISSN: 0925-8388.

[182] Arthur Hellouin de Menibus et al. “Formation and characterization of hydride blisters in Zircaloy-4 cladding tubes”. In: *Journal of Nuclear Materials* 449.1 (2014), pp. 132–147. ISSN: 0022-3115.

[183] K. Kese et al. “High temperature nanoindentation hardness and Young’s modulus measurement in a neutron-irradiated fuel cladding material”. In: *Journal of Nuclear Materials* 487 (2017), pp. 113–120. ISSN: 0022-3115.

[184] A. Rico et al. “Nanoindentation measurements of the mechanical properties of zirconium matrix and hydrides in unirradiated pre-hydrided nuclear fuel cladding”. In: *Journal of Nuclear Materials* 452.1 (2014), pp. 69–76. ISSN: 0022-3115.

[185] J. Zhang et al. “The structural stabilty and mechanical properties of ZrHx from first-principles calculations”. In: *Computational Materials Science* 226 (0 2023), p. 112226.

[186] H.E. Weekes et al. “In situ micropillar deformation of hydrides in Zircaloy-4”. In: *Acta Materialia* 92 (2015), pp. 81–96. ISSN: 1359-6454.

[187] H. Chan, S.G. Roberts, and J. Gong. "Micro-scale fracture experiments on zirconium hydrides and phase boundaries". In: *Journal of Nuclear Materials* 475 (2016), pp. 105–112. ISSN: 0022-3115.

[188] William M. Mueller, James P. Blackledge, and George G. Libowitz. *Metal Hydrides*. en. Elsevier, 1968. ISBN: 978-1-4832-3215-7. DOI: `10.1016/C2013-0-12462-2`. URL: `https://linkinghub.elsevier.com/retrieve/pii/C20130124622`.

[189] E. Zuzek et al. "The H-Zr (hydrogen-zirconium) system". en. In: *Bulletin of Alloy Phase Diagrams* 11.4 (Aug. 1990), pp. 385–395. ISSN: 0197-0216. DOI: `10.1007/BF02843318`. URL: `https://link.springer.com/article/10.1007/BF02843318`.

[190] R. C. Bowman et al. "Effects of thermal treatments on the lattice properties and electronic structure of ZrHx". In: *Physical Review B* 31.9 (May 1985), pp. 5604–5615. DOI: `10.1103/PhysRevB.31.5604`. URL: `https://link.aps.org/doi/10.1103/PhysRevB.31.5604`.

[191] R. J. Gambino and P. E. Seiden. "Correlation of the Superconducting Transition Temperature with an Empirical Pseudopotential Determined from Atomic Spectra". In: *Physical Review B* 2.9 (Nov. 1970), pp. 3571–3577. DOI: `10.1103/PhysRevB.2.3571`. URL: `https://link.aps.org/doi/10.1103/PhysRevB.2.3571`.

[192] M. Nedim Cinbiz, Xunxiang Hu, and Kurt Terrani. "Thermal expansion behavior of δ-zirconium hydrides: Comparison of δ hydride powder and platelets". In: *Journal of Nuclear Materials* 509 (Oct. 2018), pp. 566–576. ISSN: 0022-3115. DOI: `10.1016/j.jnucmat.2018.07.026`. URL: `http://www.sciencedirect.com/science/article/pii/S0022311518304021`.

[193] William L. Korst and James C. Warf. "Rare Earth-Hydrogen Systems. I. Structural and Thermodynamic Properties". In: *Inorganic Chemistry* 5.10 (Oct. 1966), pp. 1719–1726. ISSN: 0020-1669. DOI: `10.1021/ic50044a018`. URL: `https://doi.org/10.1021/ic50044a018`.

[194] F. D. Manchester and J. M. Pitre. "The Ce-H (Cerium-Hydrogen) system". en. In: *Journal of Phase Equilibria* 18.1 (Feb. 1997), p. 63. ISSN: 1054-9714. DOI: `10.1007/BF02646759`. URL: `https://doi.org/10.1007/BF02646759`.

[195] F. Aldinger and S. Joensson. "The phase diagram beryllium-cobalt". German. In: *Zeitschrift fuer Metallkunde* 68.5 (1977), pp. 362–367. URL: `http://inis.iaea.org/Search/search.aspx?orig_q=RN:8340156`.

[196] T. Spittel, M. Spittel, and H. Warlimont. "Non-Ferrous Alloys—Light Metals". In: *Landolt-Börnstein-Group VIII Advanced Materials and Technologies, H. Warlimont, ed., Springer-Verlag, Berlin Heidelberg* (2011).

[197] P. J. Baldock, W. E. Spindler, and T. W. Baker. "An X-ray diffraction study of the variation of the lattice parameters and their ratio for beryllium oxide at temperatures up to 2000° C". en. In: *Journal of Nuclear Materials* 19.2 (May 1966), pp. 169–172. ISSN: 0022-3115. DOI: `10.1016/0022-3115(66)90107-3`. URL: `http://www.sciencedirect.com/science/article/pii/0022311566901073`.

[198] Yu. M. Kozlovskii and S. V. Stankus. "Thermal expansion of beryllium oxide in the temperature interval 20–1550°C". en. In: *High Temperature* 52.4 (July 2014), pp. 536–540. ISSN: 1608-3156. DOI: `10.1134/S0018151X1403016X`. URL: `https://doi.org/10.1134/S0018151X1403016X`.

[199] Eugene Staritzky. "Crystallographic Data. 120. Diberyllium Carbide, Be2C". In: *Analytical Chemistry* 28.5 (1956). ISBN: 0003-2700 Publisher: ACS Publications, pp. 915–915.

References

[200] A. M. Saul and W. J. Smith. *Available Information on Be2C.* Tech. rep. Atomics International-A Division of North American Aviation, 1956.

[201] Anne A. Campbell et al. "Property changes of G347A graphite due to neutron irradiation". In: *Carbon* 109 (2016), pp. 860–873. ISSN: 0008-6223. DOI: `https://doi.org/10.1016/j.carbon.2016.08.042`. URL: `http://www.sciencedirect.com/science/article/pii/S0008622316306972`.

[202] K. A. Terrani et al. "The kinetics of hydrogen desorption from and adsorption on zirconium hydride". en. In: *Journal of Nuclear Materials* 397.1 (Feb. 2010), pp. 61–68. ISSN: 0022-3115. DOI: `10.1016/j.jnucmat.2009.12.008`. URL: `http://www.sciencedirect.com/science/article/pii/S0022311509009313`.

[203] Xunxiang Hu, Kurt A. Terrani, and Brian D. Wirth. "Hydrogen desorption kinetics from zirconium hydride and zirconium metal in vacuum". en. In: *Journal of Nuclear Materials* 448.1 (May 2014), pp. 87–95. ISSN: 0022-3115. DOI: `10.1016/j.jnucmat.2014.01.028`. URL: `http://www.sciencedirect.com/science/article/pii/S0022311514000397`.

[204] GF Burdi. *SNAP technology handbook. Volume II. Hydride fuels and claddings.* Tech. rep. 1964.

[205] J. A. Rawlins et al. *FFTF (Fast Flux Test Facility) cobalt test assembly results.* English. Tech. rep. WHC-SA-0292; CONF-880546-36. Westinghouse Hanford Co., Richland, WA (USA), Oct. 1987. URL: `https://www.osti.gov/biblio/6814653`.

[206] C.W. Alexander et al. *Reactor production of 252Cf and transcurium isotopes.* Tech. rep. CONF-901101–44 INIS Reference Number: 22030805. United States, 1990, p. 15.

[207] Mahmut Nedim Cinbiz, Chase N. Taylor, and Thomas A. Johnson. *Yttrium Hydride Post-Irradiation Examination Plan.* English. Tech. rep. INL/MIS-21-61303-Rev000. Idaho National Lab. (INL), Idaho Falls, ID (United States), Feb. 2021. URL: `https://www.osti.gov/biblio/1769400`.

[208] Mahmut Nedim Cinbiz. *PLN-6268 Yttrium Hydride Post Irradiation Examination Plan.* English. Tech. rep. INL/MIS-21-64412-Rev001. Idaho National Lab. (INL), Idaho Falls, ID (United States), Mar. 2022. URL: `https://www.osti.gov/biblio/1847920`.

[209] M. Nedim Cinbiz et al. *Initial Post Irradiation Examination of Irradiated Yttrium Hydride.* Tech. rep. INL RPT-22-68084.

[210] M. Nedim Cinbiz et al. *Report on the Incorporation of Post-Irradiation Examination Results of Yttrium Hydride for Advanced Moderator Handbook.* Tech. rep. INL/RPT-23-71531. Idaho National Lab. (INL), Idaho Falls, ID (United States).

[211] L. Greenwood. *Fluence capsules for the LANL-MOD-1 Experiment.* Tech. rep. PNNL-75643. Pacific Northwest National Laboratory, 2020.

[212] *Standard Test Method for Measuring Fast-Neutron Reaction Rates by Radioactivation of Niobium.* en. URL: `https://www.astm.org/e1297-18.html`.

[213] *Standard Test Method for Thermal Diffusivity by the Flash Method.* en. URL: `https://www.astm.org/e1461-13r22.html`.

[214] T. Goorley et al. “Initial MCNP6 Release Overview”. In: *Nuclear Technology* 180.3 (Dec. 2012). Publisher: Taylor & Francis _eprint: https://doi.org/10.13182/NT11-135, pp. 298–315. ISSN: 0029-5450. DOI: `10.13182/NT11-135`. URL: `https://doi.org/10.13182/NT11-135`.

[215] E.P. Luther, J.R. Wermer, and D.R. Cummins. *Fabrication of YH2 Moderator Plates, LA-UR-17-29111.* Los Alamos, NM, Oct. 2016.

[216] H. J. Goldschmidt and J. A. Brand. “The constitution of the chromium-niobium-molybdenum system”. In: *Journal of the Less Common Metals* 3.1 (1961), pp. 44–61. ISSN: 0022-5088. DOI: `https://doi.org/10.1016/0022-5088(61)90042-X`. URL: `https://www.sciencedirect.com/science/article/pii/002250886190042X`.

[217] J. Hutchinson et al. *Comparison of Approach-to-Critical Results in Current and Pulse Mode for Systems with High Starter Neutron Rates.* Tech. rep. Los Alamos National Lab.(LANL), Los Alamos, NM (United States), 2022.

[218] Dassault Systèmes. “Abaqus analysis user’s manual”. In: *Simulia Corp. Providence, RI, USA* 40 (2007).